UNIVERSITY OF SOUTHAMPTON
Faculty of Physical and Applied Sciences
Physics and Astronomy

Magneto-optic effects in colloids of ferromagnetic nanoparticles in nematic liquid crystals

by
Nina Podoliak

A thesis submitted in partial fulfillment for the
degree of Doctor of Philosophy

May 2012

UNIVERSITY OF SOUTHAMPTON

ABSTRACT

FACULTY OF PHYSICAL AND APPLIED SCIENCES

Doctor of Philosophy

MAGNETO-OPTIC EFFECTS IN COLLOIDS OF FERROMAGNETIC NANOPARTICLES IN NEMATIC LIQUID CRYSTALS

by Nina Podoliak

This thesis describes theoretical and experimental investigation of the optical and magnetic effects in nematic liquid crystals and in ferronematics, namely suspensions of ferromagnetic nanoparticles in nematic liquid crystals. In the experimental part, the effect of the nanoparticles shape and functionality on the suspension stability and magneto-optic properties were studied. Suspensions with magnetic nanospheres showed a linear response to low magnetic fields ($<$ 100 Oersted) and a decrease in the effective Frederiks threshold. Ferronematics with magnetic nanorods coated by 4-n-Octyloxybiphenyl-4-carboxylic acid were more stable and showed a larger decrease in the Frederiks threshold than the spherical magnetic nanoparticles coated by Oleic acid. No ferronematic effects were detected in the weakly magnetic hematite nanorod suspensions.

The aim of the theoretical part was to develop a realistic numerical model that could simulate the experimental results of the magnetic-field-induced Frederiks transition in nematic and ferronematic cells. The modelling was carried out in two steps. The first step involved modelling the Frederiks transition of an undoped liquid crystal cell in the presence of an easy axis pretilt and a bias, in-plane, magnetic field. The nematic model predicted that applying a bias field would lead to a shift of the threshold response, which would be sensitive to the bias field direction. This prediction was confirmed as an excellent agreement between the model and experimental data was achieved. In the second stage, a new approach to modelling of ferronematics was proposed, which involved extending previous ferronematic theories to include both the ferromagnetic effect of the particles and the intrinsic magnetic properties of the nematics. There were two variable parameters in the model, which characterise the effective ferroparticle-field interaction, and the ferroparticle-nematic director interaction. These parameters for experimental suspensions were obtained by comparing the model with experimental data. The fitting parameters were used to estimate an effective coupling energy between a nematic host and doped nanoparticles. Up to one order of magnitude higher coupling energy was obtained in the magnetite nanorod suspension as compared to the spherical magnetic nanoparticles.

The research presented in this thesis demonstrates a route to prepare highly sensitive and stable ferronematic suspensions, contributes to better understanding of the magneto-optic effects in these suspensions, and highlights their potential for applications as tailor-made optical materials in magnetically driven devices.

Contents

List of Figures

List of Tables

Declaration of authorship

I, **Nina Podoliak**, declare that the thesis entitled **"Magneto-optic effects in colloids of ferromagnetic nanoparticles in nematic liquid crystals"** and the work presented in the thesis are both my own, and have been generated by me as the result of my own original research. I confirm that:

- this work was done wholly or mainly while in candidature for a research degree at this University;
- where any part of this thesis has previously been submitted for a degree or any other qualification at this University or any other institution, this has been clearly stated;
- where I have consulted the published work of others, this is always clearly attributed;
- where I have quoted from the work of others, the source is always given. With the exception of such quotations, this thesis is entirely my own work;
- I have acknowledged all main sources of help;
- where the thesis is based on work done by myself jointly with others, I have made clear exactly what was done by others and what I have contributed myself;
- parts of this work have been published as conference proceedings and journal articles that are listed in Appendix B.

Signed:

Date:

Acknowledgements

Firstly, I would like to thank my supervisor Prof. Malgosia Kaczmarek for giving me the chance to do a PhD in Physics at the University of Southampton, for her guidance during my study, for financial support of my research and for the opportunities to represent our group at international conferences. I am very grateful to Prof. Tim Sluckin for useful discussions and the supervision of the theoretical part of my project, and also for the help with writing papers. Thanks to Dr. Giampaolo D'Alessandro for useful suggestions on theoretical calculations and Dr. Keith Daly for the help with Matlab programming. I would also like to acknowledge Dr. Oleksandr Buchnev, who has taught me how to do experiments, assisted me through my research and was always willing to discuss my results. I am grateful to Dr. Dmitry Bavykin who synthesized magnetite nanorods and provided their characteristics included into this thesis. I also thank the other members of our research group during these three years, namely Dr. Mark Herrington, Dr. James Bateman, PhD students Andrew Acreman and Mathew Proctor, and MSc student Hannah Warren, for discussing and bringing a fresh vision to some problems.

I would also like to acknowledge Prof. Victor Reshetnyak and Dr. Victor Zadorozhnii from Kiev National Taras Shevchenko University in Ukraine, for valuable discussions on this project and for the fundamental knowledge in the theoretical physics of liquid crystals that I gained from them during my study in Kiev. Special thanks to our collaborators from Institute of Physics (National Academy of Science of Ukraine) in Kiev, Prof. Yuriy Reznikov and Oleksandr Buluy, for useful suggestions and for hospitality during my visit to their laboratory, in which the first ferronematic suspensions were tested.

For proof-reading my thesis I am gratefully thankful to Dr. Kevin O'shea. No changes of intellectual content were made as a result of his advice.

Finally, I would like to thank my parents Valentyna Podoliak and Pavlo Podoliak, my sister Natalia Podoliak, and my little niece Diana for their continuous support and encouragement during the whole period of my study.

Chapter 1

Introduction

The liquid crystal phases occur in some materials as additional states of matter between a liquid state and a crystal state. Materials in these phases exhibit some remarkable properties between those of liquids and of crystals. They can flow like liquids, yet possess a certain order in the arrangements of the molecules. As a result of their molecular order, the optical properties of liquid crystals are anisotropic, as in most crystals. They also exhibit anisotropy in mechanical, electrical, and magnetic properties [1]. This fluidity in combination with the anisotropy, permits liquid crystals to be easily oriented, realigned, or deformed by applying an electric or magnetic field, by heating, or by the application of mechanical stresses. Accordingly, their optical characteristics can be easily controlled, which makes liquid crystals attractive for use in opto-electronic devices [2].

The first liquid crystal phase was observed in 1888 by an Austrian botanist, Friedrich Reinitzer. The material he discovered and investigated was cholesteryl benzoate. He found that this material demonstrated two melting points. After melting from the crystal state at 145°C, it turned into a viscous, opaque liquid with some peculiar properties. With further heating, it became isotropic and clear at a temperature of 179°C [3]. In the following year physicist Otto Lehmann discovered that the liquid in this mesophase was a distinct phase of matter, which had some crystalline properties - it exhibited birefringence. Since then the name "liquid crystal" was born [4]. The fourth state of matter was established with introducing a classification scheme of the different liquid crystal phases by Georges Friedel in 1922. His classification of the phases into nematics, cholesterics, and smectics has been accepted and is still used up to the present day.

The investigation of liquid crystal optics started with the work of Charles Mauguin, who carried out a large number of experiments on thin samples of liquid crystals placed between two glass plates and surrounded by polarizing plates. He was also the first who observed the possibility to control liquid crystal orientation, and, hence, optical properties, by a magnetic field [3]. One of the most important discoveries relating to control of liquid crystals by electric or magnetic fields was the threshold behaviour in the reorientational response of liquid crystals. This effect, described by Vsevolod Konstantinovich Frederiks in 1927 [5] and named after him as "Frederiks transition", laid the foundation for liquid crystal applications in modern technology. The theoretical description of liquid crystals started with the work of Carl Wilhelm Oseen in 1933 [6] and Frederick Charles Frank in 1958 [7]. Their work formed a background for developing liquid crystals continuum theory, which found a wide application in modelling stationary liquid crystal systems. The fundamental theory of liquid crystals was developed further by a French theoretical physicist Pierre-Gilles de Gennes [1]. His work had considerable impact on liquid crystal science and technology and he was awarded the Nobel Prize in Physics in 1991.

Despite their relatively recent discovery, liquid crystals have found a very broad range of applications in different devices, of which liquid crystal displays (LCDs) are only the best known. The potential to develop flat-panel displays using liquid crystals was shown by George Heilmeier in the early 60s [8]. This launched the development of new products, such as digital watches and pocket calculators, which were not possible without a flat, thin display. The full-motion 14-inch display screen was demonstrated by the Sharp Corporation for the first time in 1988 [2] after about 25 years of intense research in this area. Since that, liquid crystals have attracted a huge amount of scientific and industrial interest. The broader impact of liquid crystals on technology required the development of liquid crystal materials that were stable at a room temperature. The task of controlling their properties was achieved by mixing different liquid crystal molecules together to create a material with preferable properties for a given application. It was also shown that by mixing liquid crystals with other materials, for example dyes, polymers, or inorganic nanoparticles, it is possible to create new composite materials with enhanced properties.

1.1 Liquid-crystal-based composite materials

Recently, much effort has been devoted to developing composite materials based on liquid crystals. One of them, which has probably found the widest application, is the heterogeneous liquid crystal mixture with a polymer. Liquid crystal/polymer composites can have different structures depending on the type of polymer and its concentration [9]. The networks of polymer are formed inside the liquid crystal at a low polymer concentration (less that 10%). Such systems, known as polymer-stabilized liquid crystals, exhibit anisotropic light scattering [10, 11]. A structure consisting of micron size liquid crystal droplets in a polymer matrix is formed at a higher polymer concentration (30 - 40%). It is known as polymer dispersed liquid crystal (PDLC) structure. PDLCs can exhibit controllable light scattering if the refractive index of the polymer matrix, n_m, is chosen to be close to one of the refractive indices of the liquid crystal, n_o, and to differ from the other one, n_e. In the initial state, a random distribution of the optical axes in the droplets creates the index mismatch between the liquid crystal (whose average refractive index is $n_{LC} = n_e/3+2n_o/3$) and the polymer, causing strong light scattering. An external electric field orients the optical axes inside the liquid crystal droplets, matching their refractive indices with n_m and making the whole sample transparent [12, 13]. PDLCs find a broad application as switchable smart windows.

The PDLC technique is also used to develop materials that can be used as electrically switchable diffraction gratings. One type of such materials is known as a holographic PDLC (H-PDLC). It consists of nanoscale liquid crystal droplets periodically distributed in a polymer matrix by photopolymer holography [14]. Since the droplet size is small, H-PDLC film is free of light scattering and has a fast response time (30 - 200 μs). The diffraction efficiency of H-PDLC is quite high (up to 40%) and can be easily controlled by an electric field. Another switchable grating, which consists of polymer slices alternated with regularly aligned layers of liquid crystal, is known as POLICRYPS (an acronym of Polymer Liquid Crystal Polymer Slices) [15, 16]. It is characterized by a lower switching voltage and a higher diffraction efficiency (as high as 98%) than H-PDLCs. However, in comparison with most of H-PDLCs, POLICRYPS gratings are highly sensitive to the polarization of incident light and show slower response times [9].

Another group of liquid-crystal-based composite materials is the so-called filled nematics. These are suspensions of small, inorganic particles, such as SiO_2 (aerosil) or TiO_2, in nematic liquid crystals [17]. Aerosil particles in these suspensions form aggregates, whose structure and size are determined by particle size, shape,

concentration, and surface treatment. The liquid crystal defects around the aggregates cause strong light scattering [12]. The alignment of the liquid crystal by an external field arranges the particles and reduces the scattering. Filled nematics demonstrate a memory effect - the residual transmittance after the field is switched off [18, 19].

Rapid increases in the range of new nanomaterials differing in size, shape, and properties bring new interest to filled nematics. As a result, the amount of work reported on the colloidal liquid crystal suspensions has increased dramatically in recent years [20]. In particular, a lot of interest has been devoted to gold nanoparticle suspensions in liquid crystals. Gold nanoparticles exhibit surface plasmon resonance, which is associated with the coherent oscillation of the free electrons [21]. Surface plasmon resonance depends on the size and the shape of particles as well as on the dielectric properties of the surrounded media. Embedding nanoparticles into anisotropic liquid crystals can split and enhance the plasmon resonance. It can be tuned by controlling the liquid crystal orientation around the particles by means of an electric field [22, 23]. The gold nanoparticle surface can be easily functionalized by organic molecules, which can significantly influence the interaction between particles and the liquid crystal host. For example, by utilizing mesogenic surfactants, the self assembling of nanoparticles into 1-, 2- and even 3-D structures has been achieved [24]. This offers a possibility of developing metamaterials based on liquid crystals [25].

In the liquid crystal suspensions described above, the fractional content of colloidal inclusions is high. However, doping liquid crystals at a low concentration, below one percent of nanoparticles, has been shown to be a promising method to modify liquid crystal properties without the need for chemical synthesis. At such a low amount, nanometre size particles do not significantly disturb the liquid crystal order, hence producing a macroscopically homogeneous structure. However, the particles can "share" their intrinsic characteristics with the liquid crystal host, enhancing the existing properties, or introducing some new properties to the composite mixtures. A good example of this composite material is the dispersion of ferroelectric nanoparticles in liquid crystals. It was shown theoretically that the interaction between the liquid crystal molecules and the dipole moments of nanoparticles enhanced the orientational order parameters of both liquid crystal and particles, leading to an increase of the nematic-isotropic transition temperature [26, 27]. This effect was confirmed by experiment [28]. Moreover, an increased anisotropy of dielectric permittivity and birefringence were measured in a low concentration suspension of $BaTiO_3$ or $Sn_2P_2S_6$ nanoparticles in different

nematic liquid crystals [29, 30, 31, 32]. These suspensions also demonstrated a reduced Frederiks transition voltage and a faster response time than the undoped liquid crystals.

1.2 Ferronematics

Although liquid crystals can be controlled by a magnetic field, the magnetic sensitivity of ordinary nematics is very low (the diamagnetic permeability anisotropy is of the order of 10^{-7}). It usually requires a very high field strength, of the order of 1 to 10 kG (0.1 - 1 T), to trigger reorientation in liquid crystals. By contrast, the dielectric permittivity anisotropy of liquid crystals is relatively large, and driving voltages of the order of a few volts are sufficient to control the orientational response. Therefore, most of the liquid crystal devices are driven by the electric field, and liquid crystal applications using magnetic fields are rather limited. As a consequence, increasing the magnetic sensitivity of liquid crystals is an important challenge, which can potentially enable broadening the area of their applications and offers an opportunity to develop new devices.

Brochard and de Gennes suggested a method which would increase the magnetic sensitivity of liquid crystals. Their procedure involved doping the liquid crystals with a low concentration of nanometre-sized magnetic particles. In 1970 they presented the first theory of ferromagnetic nanoparticle colloids in nematic liquid crystals and named them "ferronematics" [33]. Their theory, and the subsequent work of Burylov and Raikhler [34], predicted that the ferronematics should respond to a low field, of the order of tens of Gauss. This low magnetic field would have no significant effect on the undoped nematic, but was predicted to be sufficiently strong to align or rotate the magnetic moments of the particles inside the ferronematic suspensions. The realignment or rotation effect of nanoparticles could then be transferred into the host nematic through coupling between the particles and the liquid crystal molecules. It should be noticed that in these theories the realignment effect of nematic host was assumed to be completely determined by the ferromagnetic properties of nanoparticles rather than by the intrinsic diamagnetic properties of the nematic.

The first experimental realization of ferronematic materials was carried out by Chen and Amer in 1983 [35]. Their ferronematic suspensions seemed to confirm the predicted sensitivity to a low magnetic field. However, the particles tended to aggregate, which was confirmed by anomalous behaviour and a "cellular" texture

observed in the suspension at a high magnetic field strength, above 50 Gauss. Furthermore, their results have not been replicated in the literature and it may indicate that the suspension was not stable. More recently, the interest in ferronematics was renewed as a result of the development of new magnetic nanomaterials. Ferromagnetic nanoparticles of different size and shape, including spherical [36], rodlike, and chainlike particles [37], as well as magnetically functionalized [38] or magnetically filled nanotubes [39] were used to prepare ferronematic suspensions. Those experiments demonstrated that the performance of ferronematic suspensions depended not only on the particle properties, but also on their coupling with liquid crystal molecules. A stronger interaction was achieved when the particles had anisotropic shapes [37]. In addition, Cordoyiannis *et al.* [40] demonstrated that the degree of interaction was also strongly influenced by the particle surface chemistry.

This thesis presents a report of research on ferronematic suspensions and an investigation of their magnetic and optical properties, including both experimental and theoretical work. The experimental part concerns the magneto-optic and electro-optic properties of ferronematic suspensions, containing particles with different shapes (spherical and rodlike) and with different surface coatings. The theoretical part presents two numerical models of magnetic-field-induced Frederiks transition in nematic cells and in ferronematic cells. The nematic model is used to understand the effects of the director surface pretilt and the in-plane bias magnetic field on the magneto-optic response. The ferronematic model is based on the Burylov-Raikhler theory, but takes into account nematic diamagnetism as well as the ferromagnetism of the particles. A comparison between these two effects is made based on experimental data. Both nematic and ferronematic models are used to obtain the best fit for the calculated data with experimental results.

1.3 Thesis outline

The structure of the thesis is as follows. Chapter 2 describes the general theoretical background necessary to understand the optical and magnetic properties of nematic liquid crystals and ferronematic suspensions. It starts with the theory of light propagation in isotropic and anisotropic media. After that, the theoretical background about liquid crystal phases is presented. This includes the introduction of different liquid crystal phases, the continuum theory of nematic liquid crystals, and the description of liquid crystal behaviour in external fields. Finally,

different types of magnetic materials are discussed, focusing on the properties of ferromagnetic materials. An explanation of superparamagnetism, a phenomenon occurring in nanometre size ferromagnetic nanoparticles, is given.

The main experimental techniques used in the thesis are presented in Chapter 3. This describes the characteristics of liquid crystals and the structure of experimental liquid crystal cells. It also describes magneto-optic and electro-optic measurements, which include Frederiks transition experiments in magnetic fields and in AC electric fields and also capacitance measurements. The results of these measurements are used in Chapter 5 to characterize ferronematic suspensions.

In Chapter 4, a numerical model that predicts the magneto-optic effect in a planar nematic cell is developed, based on the continuum theory of nematics. Using this model and analytical calculations, an effect of surface pretilt in the nematic alignment and in-plane bias magnetic field is discussed. It is shown that the bias field not only breaks the symmetry of the ground state, but also plays a crucial role in facilitating the reorientation induced by a large test magnetic field. In particular, a small bias field may alter significantly the strength of the test field needed to observe a given reorientation of the liquid crystal. The model is verified by achieving an excellent agreement with experimental data.

Chapter 5 focuses on the experimental investigation of ferronematic suspensions. It starts with the overview of the previous experimental work on ferronematics, which demonstrates that the performance of ferronematics depends on both the properties of magnetic inclusions and their surface coating. The main part of Chapter 5 describes ferronematic suspensions prepared with three types of Iron Oxide nanoparticles: spherical, ferromagnetic nanoparticles, hematite nanorods, and magnetite nanorods. The role of particle coating on the suspension stability is shown using two different particle surfactants: Oleic acid and 4-n-Octyloxybiphenyl-4-carboxylic acid. The suspension stability is investigated by polarized optical microscopy and by measuring the phase transition temperatures. The results of magneto-optic and electro-optic measurements are used to characterize the suspension properties. A linear optical response to a low magnetic field as well as a decrease in the effective Frederiks threshold is detected in the cells with suspensions of ferromagnetic nanoparticle and magnetite nanorods. These effects are associated with the magnetic properties of nanoparticles.

Chapter 6 presents the numerical model of ferronematic cell in a magnetic field. The model is based on continuum theory, which is described at the beginning of

this chapter. The proposed model takes into account both the nematic diamagnetism and the particle ferromagnetism. This model is fitted to the experimental data from Chapter 5. Analysis of experimental results suggested that in the experimental ferronematic suspension the effect associated with nematic diamagnetism is dominant over the effect of ferroparticles. This is taken into account in the model during the fitting procedure. A good fit of the experimental results with the proposed model is achieved in a low concentration suspension. The theory also predicts the main trend for a high concentration suspension. Some disagreement between theory and experiment in this case is explained by particle aggregation. A possible way to account for the aggregation effect in the model is proposed in Chapter 7. This chapter contains the main conclusions of the thesis and also discusses some future plans in this project.

References

[1] P. G. de Gennes and J. Prost. *The Physics of Liquid Crystals*. Clarendon Press, Oxford, 2nd edition, 1993.

[2] H. Kawamoto. The history of liquid cryatal display. *Proceedings of the IEEE*, 90(4), 2002.

[3] T. J. Sluckin, D. A. Dunmur, and H. Stegemeyer. *CrystalsThat Flow: Classic papers from the history of liquid crystals*. Taylor and Francis, 2004.

[4] O. Lehmann. On flowing crystals. *Zeitschrift für Physikalische Chemie*, 4: 462–72, 1889, translation in *Crystals That Flow*, pages 43-52, 2004.

[5] A. Repiova and V. Frederiks. K voprosy o prirode anisotropno-zhidkogo sostoyaniya veshestva (On the problem of the nature of the anisotropic liquid state of matter) (in russian). *Journal of Russian Physical Chemistry Society*, 59:183–200, 1927.

[6] C. W. Oseen. The theory of liquid crystals. *Transactions of the Faraday Society*, 29:883–899, 1933, from *Crystals That Flow*, pages 255-272, 2004.

[7] F. C. Frank. On the theory of liquid crystals. *Discussions of the Faraday Society*, 25:19–28, 1958, from *Crystals That Flow*, pages 389-399, 2004.

[8] G. H. Heilmeier. Liquid crystal displays: an experiment in interdisciplinary research that worked. *IEEE Transactions on Electron Devices*, ED-23(7), 1976.

[9] Y. J. Liu snd X. W. Sun. Holographic polymer-dispersed liquid crystals: materials, formation, and applications. *Advances in OptoElectronics*, 2008: 684349, 2008.

[10] M. Kreuzer, T. Tschudi, and R. Eidenschink. New liquid crystal display with bistability and selective erasure using scattering in filled nematics. *Applied Physics Letters*, 62(15):1712–1714, 1993.

[11] Y. K. Fung, D.-K. Yang, S. Ying, L. C. Chien, S. Žumer, and J. M. Doane. Polymer networks formed in liquid crystals. *Liquid Crystals*, 19:797–801, 1995.

[12] J. M. Doane, N. A. Vaz, B. G. Wu, and S. Žumer. Field controlled light scattering from nematic microdroplets. *Applied Physics Letters*, 48:269–271, 1986.

[13] D. Higgins. Probing the mesoscopic chemical and physical properties of polymer-dispersed liquid crystals. *Advanced Materials*, 12:251–264, 2000.

[14] T. J. Bunning, L. V. Natarajan, V. P. Tondiglia, and R. L. Sutherland. Holographic polymer-dispersed liquid crystals (H-PDLCs). *Annual Review of Materials Research*, 30:83–115, 2000.

[15] R. Caputo, L. De Sio, A. Veltri, C. Umeton, and A. V. Sukhov. Development of a new kind of switchable holographic grating made of liquid-crystal films separated by slices of polymeric material. *Optics Letters*, 29(11), 2004.

[16] A. D'Alessandro, R. Asquini, C. Gizzi, R. Caputo, C. Umeton, A. Veltri, and A. V. Sukhov. Electro-optic properties of switchable gratings made of polymer and nematic liquid-crystal slices. *Optics Letters*, 29(12), 2004.

[17] N. J. Diorio Jr, M. R. Fisch, and J. W. West. The electro-optic properties of colloidal silica filled nematics. *Liquid Crystals*, 29:589–596, 2002.

[18] A. Glushchenko, H. Kresse, V. Reshetnyak, Yu. Reznikov, and O. V. Yaroshchuk. Memory effect in filled nematic liquid crystals,. *Liquid Crystals*, 23:241–246, 1997.

[19] G. Puchkovskaya, Yu. Reznikov, A. Yakubov, O. V. Yaroshchuk, and A. Glushchenko. Molecular interaction and memory of filled liquid crystals. *Journal of Molecular Structure*, 404:121–128, 1997.

[20] H. Qi and T. Hegmann. Impact of nanoscale particles and carbone nanotubes on current and future generation of liquid crystal display. *Journal of Materials Chemistry*, 18:3288–3294, 2008.

[21] S. Link and M. A. El-Sayed. Shape and size dependence of radiative, non-radiative and photothermal properties of gold nanocrystals. *International Reviews in Physical Chemistry*, 19(3):409–453, 2000.

[22] S. Y. Park and D. Stroud. Splitting of surface plasmon frequencies of metal particles in a nematic liquid crystal. *Applied Physics Letters*, 85:2920–2922, 2004.

[23] M. Kreuzer, T. Tschudi, and R. Eidenschink. Coupling of the plasmon resonances of chemically functionalized gold nanoparticles to local order in thermotropic liquid crystals. *Chemistry of Materials*, 19:1053–1061, 2007.

[24] X. Zeng, F. Liu, A. G. Fowler, G. Ungar amd L. Cseh, G. H. Mehl, and J. E. Macdonald. 3D ordered gold strings by coating nanoparticles with mesogens. *Advanced Materials*, 21:1746–1750, 2009.

[25] M. Draper, I. M. Saez, S. J. Cowling, P. Gai, B. Heinrich, B. Donnio, D. Guillon, and J. W. Goodby. Self-assembly and shape morphology of liquid-crystalline gold metamaterials. *Advanced Functional Materials*, 21:1260–1278, 2011.

[26] L. M. Lopatina and J. V. Selinger. Theory of ferroelectric nanoparticles in nematic liquid crystals. *Physical Review Letters*, 102:197802, 2009.

[27] L. M. Lopatina and J. V. Selinger. Maier-Saupe-type theory of ferroelectric nanoparticles in nematic liquid crystals. *Physical Review E*, 2011.

[28] M. Čopič, A. Mertelj andO. Buchnev, and Yu. Reznikov. Coupled director and polarization fluctuations in suspensions of ferroelectric nanoparticles in nematic liquid crystalsl. *Physical Review E*, 76:011702, 2007.

[29] Yu. Reznikov, O. Buchnev, O. Tereshchenko, V. Reshetnyak, A. Glushchenko, and J. West. Ferroelectric nematic suspension. *Applied Physics Letters*, 82: 1917–1919, 2003.

[30] O. Buchnev, E. Ouskova, V. Reshetnyak, Yu. Reznikov, H. Kresse, and A. Grabar. Enhanced dielectric response of liquid crystal ferroelectric suspension. *Molecular Crystals and Liquid Crystals*, 422:47–55, 2004.

[31] M. Kaczmarek, O. Buchnev, and I. Nandhakumar. Ferroelectric nanoparticles in low refractive index liquid crystals for strong electro-optic response. *Applied Physics Letters*, 92:103307, 2008.

[32] J.-F. Blach, S. Saitzek, C. Legrand, L. Dupont, J.-F. Henninot, and M. Warenghem. $BaTio_3$ ferroelectric nanoparticles dispersed in 5cb nematic liquid crystal: synthesis and electro-optical characterization. *Journal of Applied Physics*, 107:074102, 2010.

[33] F. Brochard and P. G. de Gennes. Theory of magnetic suspensions in liquid crystal. *Journal de Physique (Paris)*, 31:691–708, 1970.

[34] S. V. Burylov and Yu. L. Raikher. Macroscopic properties of ferronematics cause by orientational interactions on the particles surface. *Molecular Crystals and Liquid Crystals*, 258:107–122, 123–141, 1995.

[35] S.-H. Chen and N. M. Amer. Observation of macroscopic colective behavior and new texture in magnetically doped liguid crystal. *Physical Review Letters*, 51(25):2298–2301, 1983.

[36] P. Kopčanský, N. Tomašovičová, M. Koneracká, M. Timko, V. Závišová, N. Eber, K. Fodor-Csorba, T. Toth-Katona, A. Vajda, J. Jadzyn, E. Beaugnon, and X. Chaud. The structural instabiliteis in ferronematic based on liquid crystal with negative diamagnetic susceptibility anisotropy. *Journal of Magnetism and Magnetic Materials*, 322:3696–3700, 2010.

[37] P. Kopčanský, N. Tomašovičová, M. Koneracká, V. Závišová, M. Timko, A. Dzarova, A. Sprincova, N. Eber, K. Fodor-Csorba, T. Toth-Katona, A. Vajda, and J. Jadzyn. Structural changes in the 6CHBT liquid crystal doped with spherical, rodlike, and chainlike magnetic particles. *Physical Review E*, 78:011702, 2008.

[38] Z. Mitróová, N. Tomašovičová, M. Timko, M. Koneracká, J. Kováč, J. Jadzyn, I. Vávra, N. Éber, T. Tóth-Katona, E. Beaugnon, X. Chaud, and P. Kopčanský. The sensitivity of liquid crystal doped with functionalized carbon nanotubes to external magnetic fields. *New Journal of Chemistry*, 35: 1260–1264, 2011.

[39] O. Buluy, S. Nepijko, V. Reshetnyak, E. Ouskova, V. Zadorozhnii, A. Leonhardt, M. Ritschel, G. Schönhense, and Yu. Reznikov. Magnetic sensitivity of a dispersion of aggregated ferromagnetic carbon nanotubes in liquid crystals. *Soft Matter*, 7:644–649, 2011.

[40] G. Cordoyiannis, L. K. Kurihara, L. J. Martinez-Miranda, C. Glorieux, and J. Thoen. Effect of magnetic nanoparticles with different surface coating on the phase transitions of octylcyanobiphenyl liquid crystal. *Physical Review E*, 79:011702, 2009.

Chapter 2

Optical and magnetic properties of liquid crystals

This chapter describes several topics essential for understanding the work presented in Chapter 3, 4, and 6. It starts with the basic description of electromagnetic wave propagation in an optical media, based on the fundamental equations of electromagnetism: Maxwell's equations and material equations. Section 2.1 also introduces the specific feature of anisotropic media. In particular, the equations for the dependence of refractive indices on the direction of light propagation are derived, which will be used to model the light propagation in anisotropic liquid crystal samples.

Section 2.2 gives an introduction to different liquid crystal phases and, in more detail, describes the properties of the nematic liquid crystal phase. The basic equations of continuum theory, which will be used in Chapter 4 and 6 to model respectively nematic and ferronematic behaviour in the magnetic field, are presented in Section 2.2.1 and 2.2.2. The optical properties of nematics are described in Section 2.2.3. This section also explains the optical method of detecting the nematic response to an external field, which is used in the experimental part of the thesis.

Section 2.3 discusses the magnetic properties of nanometre size particles. Firstly, it introduces different types of magnetic materials: ferromagnetic, paramagnetic and diamagnetic. Secondly, the changes in ferromagnetic properties with decreasing the particle size are discussed with particular focus on the transition between ferromagnetic and superparamagnetic behaviour.

2.1 Light propagation in an optical medium

The theory of light interaction with matter is based on Maxwell's equations, which combine the fundamental laws of electromagnetism. Maxwell's equations connect four basic quantities of electromagnetic field: the electric field $\boldsymbol{E}$, the electric displacement $\boldsymbol{D}$, the magnetic induction $\boldsymbol{B}$, and the magnetic field $\boldsymbol{H}$, with a distribution of the charge density ρ and the electric current density $\boldsymbol{j}$ inside the media. The differential form of these equations is:

$$\boldsymbol{\nabla} \times \boldsymbol{E} = -\frac{1}{c}\frac{\partial \boldsymbol{B}}{\partial t}, \tag{2.1a}$$

$$\boldsymbol{\nabla} \times \boldsymbol{H} = \frac{1}{c}\frac{\partial \boldsymbol{D}}{\partial t} + \frac{4\pi}{c}\boldsymbol{j}, \tag{2.1b}$$

$$\boldsymbol{\nabla} \cdot \boldsymbol{D} = 4\pi\rho, \tag{2.1c}$$

$$\boldsymbol{\nabla} \cdot \boldsymbol{B} = 0, \tag{2.1d}$$

where c is a constant, equal to the velocity of light in vacuum. The first equation describes Faraday's law of induction, the second equation is an extended form of Ampere's law, while the third and the fourth equations are the forms of Gauss' law applied to electrostatics and magnetism, respectively [1].

Equations (2.1a)-(2.1d) are written in the Gaussian system of units, which is used in this thesis. In this system of units, the magnetic field, $\boldsymbol{H}$, is measured in Oersted (Oe), (1 Oe = $10^3/4\pi$ A/m), the magnetic induction, $\boldsymbol{B}$, is measured in Gauss (G), (1 G = 10^{-4} Tesla), and the permeability of vacuum is taken as unity. The electric field, $\boldsymbol{E}$, and the electric displacement, $\boldsymbol{D}$, are expressed in the same units: statV/cm (1 statV = 300 V) [2].

The interaction of an electromagnetic wave with a medium results in an electric polarization, $\boldsymbol{P}$, and a magnetic polarization (or magnetization), $\boldsymbol{M}$. The connection between the fundamental electromagnetic quantities can be expressed as:

$$\boldsymbol{D} = \boldsymbol{E} + 4\pi\boldsymbol{P}, \tag{2.2a}$$

$$\boldsymbol{B} = \boldsymbol{H} + 4\pi\boldsymbol{M}. \tag{2.2b}$$

When the fields are sufficiently weak, the electric and the magnetic polarizations are proportional to the electric and the magnetic field, respectively:

$$\boldsymbol{P} = \eta\boldsymbol{E}, \quad \boldsymbol{M} = \chi\boldsymbol{H}. \tag{2.3}$$

The factor η is the dielectric susceptibility and χ is the magnetic susceptibility. Taking into account these relationships, Equations (2.2a, 2.2b) can be expressed in the form, known as material equations:

$$\boldsymbol{D} = \varepsilon \boldsymbol{E}, \quad \boldsymbol{B} = \mu \boldsymbol{H}. \tag{2.4}$$

Here $\varepsilon = 1 + 4\pi\eta$ is known as the dielectric permittivity (or constant) and $\mu = 1 + 4\pi\chi$ is called the magnetic permeability. Material equations (2.4) should be supplemented by an equation for electric current:

$$\boldsymbol{j} = \sigma \boldsymbol{E}, \tag{2.5}$$

where σ is the conductivity of the media. This equation is the differential form of Ohm's law.

From the physical point of view, Equations (2.3) have an assumption that a media response to electromagnetic field is: (i) instantaneous - the polarization and magnetization depend on the momentary values of the fields; (ii) local - the values of $\boldsymbol{P}$ and $\boldsymbol{M}$ are determined only by the local fields; (iii) linear - vectors $\boldsymbol{P}$ and $\boldsymbol{M}$ are proportional to the field strengths [3]. For intense fields, however, the polarization should contain higher order terms of the field strengths, which result in non-linear optical effects [3]. However, these effects are not considered in this thesis, so the assumptions in Equations (2.3) are considered exact.

Maxwell's equations (2.1a)-(2.1d) in combination with the material equations (2.4),(2.5) allow the determination of the electromagnetic field vectors for a given distribution of currents and charges. In the majority of cases discussed further, the electromagnetic wave propagates in the medium without free charges and currents ($\rho = 0,\ \boldsymbol{j} = 0$). Taking into account the material equations (2.4), Maxwell's equations can be written as:

$$\boldsymbol{\nabla} \times \boldsymbol{E} = -\frac{\mu}{c}\frac{\partial \boldsymbol{H}}{\partial t}, \tag{2.6a}$$

$$\boldsymbol{\nabla} \times \boldsymbol{H} = \frac{\varepsilon}{c}\frac{\partial \boldsymbol{E}}{\partial t}, \tag{2.6b}$$

$$\boldsymbol{\nabla} \cdot \varepsilon \boldsymbol{E} = 0, \tag{2.6c}$$

$$\boldsymbol{\nabla} \cdot \mu \boldsymbol{H} = 0. \tag{2.6d}$$

Taking the curl of Equation (2.6a) and substituting Equation (2.6b) result in the wave equation for the electric field $\boldsymbol{E}$:

$$\boldsymbol{\nabla} \times \boldsymbol{\nabla} \times \boldsymbol{E} = -\frac{\varepsilon\mu}{c^2}\frac{\partial^2 \boldsymbol{E}}{\partial t^2}, \tag{2.7}$$

which is used to describe the wave propagation through a medium. Deriving this equation, it is assumed that the dielectric permittivity and the magnetic permeability are independent on the space coordinate and time. It is worth mentioning that the wave equation in this form is valid in both isotropic and anisotropic media.

In isotropic media the material properties are independent of the direction of the wave propagation; this means that the dielectric permittivity and the magnetic permeability are scalars. Using the vector identity $\boldsymbol{\nabla} \times \boldsymbol{\nabla} \times \boldsymbol{E} = \boldsymbol{\nabla}(\boldsymbol{\nabla} \cdot \boldsymbol{E}) - \nabla^2 \boldsymbol{E}$ and Equation (2.6c), which in isotropic medium becomes $\boldsymbol{\nabla} \cdot \boldsymbol{E} = 0$, Equation (2.7) reduces to:

$$\nabla^2 \boldsymbol{E} = \frac{\varepsilon\mu}{c^2}\frac{\partial^2 \boldsymbol{E}}{\partial t^2}. \tag{2.8}$$

An analogous equation can be derived for the magnetic field $\boldsymbol{H}$:

$$\nabla^2 \boldsymbol{H} = \frac{\varepsilon\mu}{c^2}\frac{\partial^2 \boldsymbol{H}}{\partial t^2}. \tag{2.9}$$

The solution of these wave equations results in the existence of a monochromatic plane wave, which can be specified in terms of the electric field vector as:

$$\boldsymbol{E} = \boldsymbol{\mathcal{E}} e^{i\{(\boldsymbol{k}\cdot\boldsymbol{r}) - \omega t + \delta\}}, \tag{2.10}$$

where $|\boldsymbol{\mathcal{E}}|$ is the electric field amplitude, $\boldsymbol{k} = \frac{\omega}{\upsilon}\hat{\boldsymbol{k}}$ is the wave vector, ω is the angular frequency, and δ is the phase. This wave propagates through a medium in the direction defined by unit vector $\hat{\boldsymbol{k}}$ with a phase velocity $\upsilon = c/n$, where $n = \sqrt{\varepsilon\mu}$ is the refractive index of the medium. Accepting the Cartesian coordinate system, in which the direction of propagation is parallel to the z axis, the electric field can be written in terms of two components orthogonal to the z axis:

$$E_x = \mathcal{E}_x e^{i\{kz - \omega t + \delta_x\}}, \quad E_y = \mathcal{E}_y e^{i\{kz - \omega t + \delta_y\}}. \tag{2.11}$$

Depending on the phase lag between these two components, $\delta = \delta_y - \delta_x$, and the ratio of the amplitudes, $\mathcal{E}_y/\mathcal{E}_x$, different states of the light polarization can

be defined. When $\delta = 0$ or π, the electric field oscillates in a fixed plane, the orientation of which is defined by the ratio between the amplitudes $\mathcal{E}_x$, $\mathcal{E}_y$. This state is known as linear polarization, and the plane of the wave oscillation is the polarization plane. Circular polarization occurs when $\delta = \pm\pi/2$ and $\mathcal{E}_x = \mathcal{E}_y$. The state with $\delta = \pi/2$ or $-\pi/2$ are called right-handed or left-handed circular polarizations, respectively. All other states are known as elliptical polarizations. The polarization state might change when the light passes though an optically active or an anisotropic medium.

2.1.1 Propagation of light in an anisotropic medium

In anisotropic media the permittivity, ε, and permeability, μ, are direction dependent. From the mathematical point of view, they become the tensor quantities. The propagation of light in magnetically isotropic but electrically anisotropic media is considered in this section. This assumption approximates to liquid crystal materials, as their magnetic anisotropy is very small (in the order of $\sim 10^{-7}$), while their dielectric anisotropy is grater than unity [4]. Then, μ is a scalar and $\hat{\varepsilon}$ is a tensor in material equations (2.4). The dielectric permittivity tensor is symmetric, so it can be diagonalized by choosing a suitable coordinate system, which is called the principal coordinates. In these coordinates

$$\hat{\varepsilon} = \begin{pmatrix} \varepsilon_x & 0 & 0 \\ 0 & \varepsilon_y & 0 \\ 0 & 0 & \varepsilon_z \end{pmatrix}, \tag{2.12}$$

where ε_x, ε_y and ε_z are principal dielectric constants. If two of the principal dielectric constants are equal ($\varepsilon_x = \varepsilon_y \neq \varepsilon_z$), the medium is called a uniaxial crystal, and the principal axis z is called the optical axis. In a biaxial crystal, however, all dielectric constants are different ($\varepsilon_x \neq \varepsilon_y \neq \varepsilon_z$).

Let us assume that a monochromatic plane wave, with angular frequency ω is propagated through an anisotropic medium in a direction set by unit vector $\hat{\boldsymbol{k}}$, then

$$\boldsymbol{E} = \boldsymbol{\mathcal{E}} e^{i\{(\boldsymbol{k}\cdot\boldsymbol{r})-\omega t\}}, \tag{2.13}$$

where the wave vector $\boldsymbol{k} = \frac{\omega}{c} n\hat{\boldsymbol{k}}$ depends on the refractive index n experienced by the wave. Substituting Equation (2.13) into (2.7), the following equation is obtained:

$$\hat{\varepsilon}\mu\boldsymbol{\mathcal{E}} = n^2\left(\boldsymbol{\mathcal{E}} - \hat{\boldsymbol{k}}(\hat{\boldsymbol{k}}\cdot\boldsymbol{\mathcal{E}})\right). \tag{2.14}$$

In the principal coordinate system, substituting (2.12) into (2.14) gives an expression for the field components

$$\mathcal{E}_i = \frac{n^2\hat{k}_i}{n^2 - \varepsilon_i\mu}(\hat{\boldsymbol{k}}\cdot\boldsymbol{\mathcal{E}}), \qquad i = (x, y, z). \tag{2.15}$$

To rewrite Equation (2.15) for the phase velocity $\upsilon = c/n$, the principal phase velocities of wave propagation should be introduced as $\upsilon_i = c/n_i$, where $n_i = \sqrt{\varepsilon_i\mu}$ are principal refractive indices. Then Equation (2.15) takes the form:

$$\mathcal{E}_i = \frac{\upsilon_i^2\hat{k}_i}{\upsilon_i^2 - \upsilon^2}(\hat{\boldsymbol{k}}\cdot\boldsymbol{\mathcal{E}}), \qquad i = (x, y, z). \tag{2.16}$$

Making simple mathematical manipulations that are described in detail in [1], it is possible to obtain the equation

$$\hat{k}_x^2(\upsilon^2 - \upsilon_y^2)(\upsilon^2 - \upsilon_z^2) + \hat{k}_y^2(\upsilon^2 - \upsilon_z^2)(\upsilon^2 - \upsilon_x^2) + \hat{k}_z^2(\upsilon^2 - \upsilon_x^2)(\upsilon^2 - \upsilon_y^2) = 0, \tag{2.17}$$

which is quadratic in υ^2. This is Fresnel's equation of wave normals, which can be solved to find the phase velocity of a wave propagated in the given direction $\hat{\boldsymbol{k}}$.

Let us restrict it to the case of light propagation in a uniaxial crystal, as nematic liquid crystals belong to this class of materials. Uniaxial crystals can be characterised by two refractive indices: ordinary, $n_o = n_x = n_y$, experienced by the light polarized orthogonal to the optical axis, and extraordinary, $n_e = n_z$, experienced by the light polarized in the direction of the optical axis. This means that the principal velocities in Equation (2.17) can be replaced by ordinary, $\upsilon_o = \upsilon_x = \upsilon_y$, and extraordinary, $\upsilon_e = \upsilon_z$, velocities. Then, if the wave propagates at an angle θ_i with respect to the optical axis, Fresnel's equation reduces to:

$$(\upsilon^2 - \upsilon_o^2)\left[(\upsilon^2 - \upsilon_e^2)\sin^2\theta_i + (\upsilon^2 - \upsilon_o^2)\cos^2\theta_i\right] = 0. \tag{2.18}$$

This equation gives two solutions:

$$\begin{aligned} v'^2 &= v_o^2, \\ v''^2(\theta_i) &= v_o^2 \cos^2\theta_i + v_e^2 \sin^2\theta_i, \end{aligned} \tag{2.19}$$

which correspond to two waves that propagate through the medium encountering different refractive indices:

$$\begin{aligned} n' &= n_o, \\ n''(\theta_i) &= \frac{n_o n_e}{\sqrt{n_e^2 \cos^2\theta_i + n_o^2 \sin^2\theta_i}}. \end{aligned} \tag{2.20}$$

One of the waves is the ordinary wave, with the refractive index independent of the direction of propagation; the other one is the extraordinary wave, with the effective refractive index $n_{eff} = n''(\theta_i)$ dependent on the direction of propagation. It should be mentioned that both indices are equal when the wave propagates in the direction of the optical axis (when $\theta_i = 0$).

In the next part of this chapter, the basic concept of light propagation inside an anisotropic media will be applied to nematic liquid crystals. Initially, however, a general overview of liquid crystals is presented and the basic equations, which are used in this thesis, are derived.

2.2 Liquid crystals

It is conventional to consider three states of matter: crystal, liquid, and gas. However, some organic materials when changing from crystalline to liquid state show one or more additional transitions involving new phases, known as liquid crystal (or mesomorphic) phases [4]. Some materials exhibit liquid crystalline phases when an appropriate concentration of molecules is dissolved in some solvent; they are called lyotropic liquid crystals. For other types of materials, the liquid crystalline state exists for a certain temperature range only; these are called thermotropic liquid crystals. This type of material has two characteristic temperatures: a temperature at which they transform from solid to liquid crystal, the so-called melting point, and a temperature at which they transform from liquid crystal to liquid, the so-called clearing point.

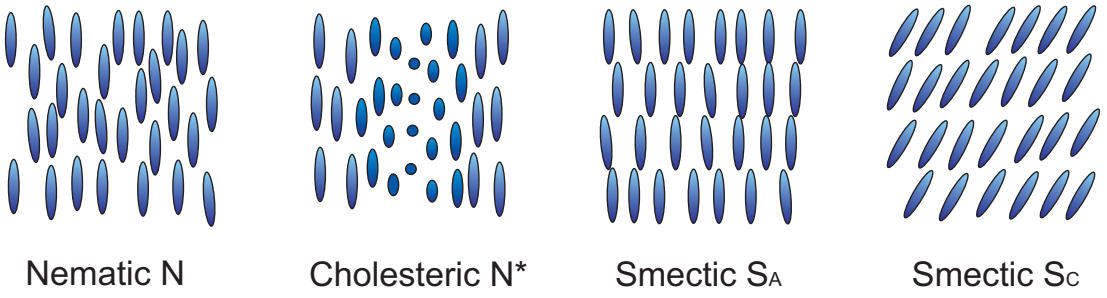

FIGURE 2.1: The arrangements of molecules in different liquid crystal phases.

The molecules that can form a liquid crystal phase require an anisometric shape, often rod-like. Depending on the molecular arrangements, there are two conventional groups of thermotropic liquid crystals: nematics and smectics, see Figure 2.1. In the nematic phase (N) the molecules do not have positional order, they are distributed randomly, but they possess a long-range orientation order. In chiral nematic phase (N*), often called cholesteric, the molecules tend to align in a helical manner. Smectics, unlike nematics, possess some degree of the positional order; the molecules form a layered structure. Depending on the molecular arrangement in the layers, different phases of smectics have been identified: S_A, S_C, among others. Only the nematic liquid crystals are considered in this thesis. Detailed information about other liquid crystal phases can be found in the literature [5, 6].

2.2.1 Nematic liquid crystals

Nematics are the most widely studied and the most widely used liquid crystals. They usually consist of elongated molecules (with a length between 1 and 3 nm and a width of approximately 0.1 to 0.5 nm), which are aligned along one common direction. This direction is defined by the unit vector $\boldsymbol{n}$, which is called the nematic director. The states corresponding to $\boldsymbol{n}$ and $-\boldsymbol{n}$ are identical. The long-range orientation order is characterised by an order parameter tensor [4]:

$$Q_{\alpha\beta} = Q(T)\left(n_\alpha n_\beta - \frac{1}{3}\delta_{\alpha\beta}\right), \tag{2.21}$$

where $n_{\alpha,\beta}$ are the corresponding components of the director and $\delta_{\alpha\beta}$ is the delta-function. The scalar order parameter $Q(T)$ describes the degree of molecular

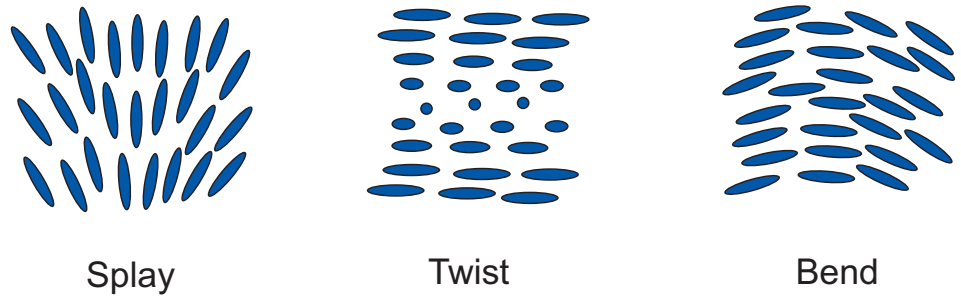

FIGURE 2.2: Three types of deformations occurring in nematics.

ordering. An isotropic fluid would have $Q = 0$ and a perfectly orientated solid would have $Q = 1$. Liquid crystals typically have value of Q between 0.3 and 0.8.

Nematics can be described on a basis of the continuum theory, which depends on the works of Oseen [7] and Frank [8]. In this theory, the details of molecular structure are neglected. The nematic states are defined by the distribution of the order parameter tensor field, $Q_{\alpha\beta}(\boldsymbol{r})$. In most cases it is possible to assume that the characteristic length over which significant variation of $Q_{\alpha\beta}$ occurs is much larger than the molecular size. Then, the order parameter $Q_{\alpha\beta}(\boldsymbol{r})$ can be defined by the director field only. Thus, the nematic state can be entirely described in terms of the director field, $\boldsymbol{n}(\boldsymbol{r})$. Slow variation of the order parameter means that there is a slowly changing director field in the bulk of the liquid crystal sample, except for a few singular points or lines, which are called defects [9].

Continuum theory is based on the phenomenological expressions that describe the free energy of a liquid crystal state. The equilibrium state always corresponds to the minimum of free energy. The free energy density may be expressed as a series of the order parameter. Any distortion from the orientation order leads to additional terms in free energy involving the gradient of $Q_{\alpha\beta}$ [4].

Upon application of any external perturbation fields, nematic liquid crystals will undergo deformations. There are three main types of deformations for nematics: splay, twist, and bend, see Figure 2.2. The free energy density associated with these deformations was suggested by Frank [8]:

$$f_d = \frac{1}{2}K_1[\boldsymbol{\nabla}\cdot\boldsymbol{n}]^2 + \frac{1}{2}K_2[\boldsymbol{n}\cdot(\boldsymbol{\nabla}\times\boldsymbol{n})]^2 + \frac{1}{2}K_3[\boldsymbol{n}\times(\boldsymbol{\nabla}\times\boldsymbol{n})]^2, \tag{2.22}$$

where $K_1,\ K_2,\ K_3$ are the splay, twist, bend Frank elastic constants, respectively. This is the fundamental formula of the nematic continuum theory. It will be used in this thesis to model liquid crystal samples.

In all of the experiments, nematic samples are separated from an external medium by some boundaries, which are often plane surfaces. Thus, a complete description of nematic samples should include not only the bulk deformation energy, but also the surface interaction energy at the boundaries, which is often called anchoring energy. The orientation of the molecules on the surface is characterised by two parameters: an easy axis and a surface anchoring energy density, W_s. The easy axis shows an equilibrium position of the director on the surface that minimizes the surface energy. The simplest form of the anchoring energy density has been suggested by Rapini and Papoular [10]:

$$f_s = \frac{1}{2} W_s \sin^2 \gamma, \tag{2.23}$$

where γ is the angle of the director deviation from the easy axis.

When $W_s \to \infty$ (strong anchoring) the director cannot deviate from the easy axis direction. Thus, the director field could be described by the bulk terms in the free energy functional only, and by the fixed boundary conditions. On the other hand, when W_s has a finite magnitude, typically of the order of 10^{-2} erg cm^{-2} or less, the molecules are not strongly anchored at the boundaries (weak anchoring). Both bulk and surface terms in the free energy should be taken into account. Sometimes, to characterise the anchoring type, a dimensionless parameter is used [11]:

$$w_i = \frac{D W_s}{K_i}, \tag{2.24}$$

where K_i is one of the elastic constants, depending on the sample geometry, D is the liquid crystal layer thickness. $w_i \gg 1$ and $w_i \ll 1$ correspond to strong and weak anchoring, respectively.

The type of liquid crystal alignment on the plane surface is usually defined by an angle, α, between the easy axis and the plane. Depending on this angle, different alignment conditions could be distinguished: planar ($\alpha \approx 0$), homeotropic ($\alpha = \pi/2$), and tilted ($0 < \alpha < \pi/2$). There are several methods to achieve a particular alignment [6, 11]. Most commonly, the planar alignment is produced by mechanical rubbing of the surface with a brush or a cloth. The rubbing creates microgrooves,

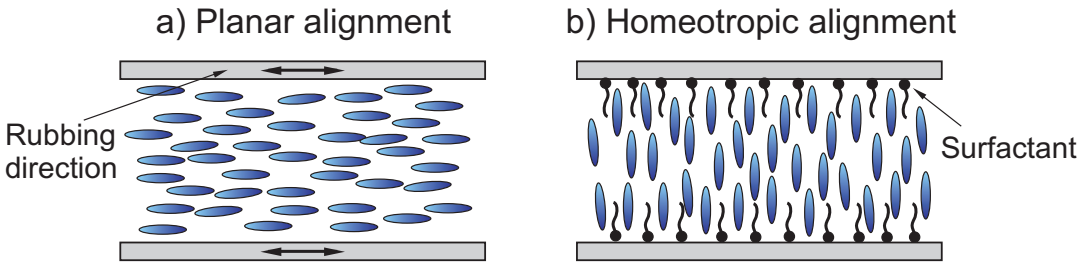

FIGURE 2.3: Two types of liquid crystal alignment between parallel glass substrates: (a) planar, (b) homeotropic.

which promote a well defined orientation of the molecules on the substrate surface. The most popular technique for the homeotropic orientation is the deposition of surfactant or polymer molecules with long tails. These tails extend out normal to the surface, inducing alignment as demonstrated in Figure 2.3.

2.2.2 Liquid crystals in external magnetic or electric fields

Liquid crystals, like most organic materials, are diamagnetic. Their diamagnetic susceptibility, owing to the long-range orientational order, is anisotropic. It can be characterised with two values $\chi_{\parallel}$ and $\chi_{\perp}$, parallel and perpendicular to the nematic director, respectively. Applying an external magnetic field $\boldsymbol{H}$ to a nematic of director $\boldsymbol{n}$ leads to induced magnetization $\boldsymbol{M}$ as derived in [4]:

$$\begin{aligned} \boldsymbol{M} &= \chi_{\parallel}\boldsymbol{H}_{\parallel} + \chi_{\perp}\boldsymbol{H}_{\perp}, \\ \boldsymbol{M} &= \chi_{\perp}\boldsymbol{H} + \chi_a \boldsymbol{n}(\boldsymbol{n}\cdot\boldsymbol{H}), \end{aligned} \tag{2.25}$$

where $\chi_a = \chi_{\parallel} - \chi_{\perp}$ represents an anisotropy of diamagnetic susceptibility. Taking into account Equation (2.2b), the corresponding contribution to the free energy density can be derived as:

$$f_{magn} = -\frac{1}{8\pi}\boldsymbol{B}\cdot\boldsymbol{H} = -\frac{1}{2}\boldsymbol{M}\cdot\boldsymbol{H} = -\frac{1}{2}\chi_{\perp}H^2 - \frac{1}{2}\chi_a(\boldsymbol{n}\cdot\boldsymbol{H})^2. \tag{2.26}$$

The first term in this equation is independent of the director orientation and may be omitted during the modelling of nematic samples.

Both $\chi_{\parallel}$, $\chi_{\perp}$ are negative for nematics, while χ_a has a small, usually positive value ($\sim 10^{-7}$ in cgs units [4]). Due to this, nematic molecules tend to align in the

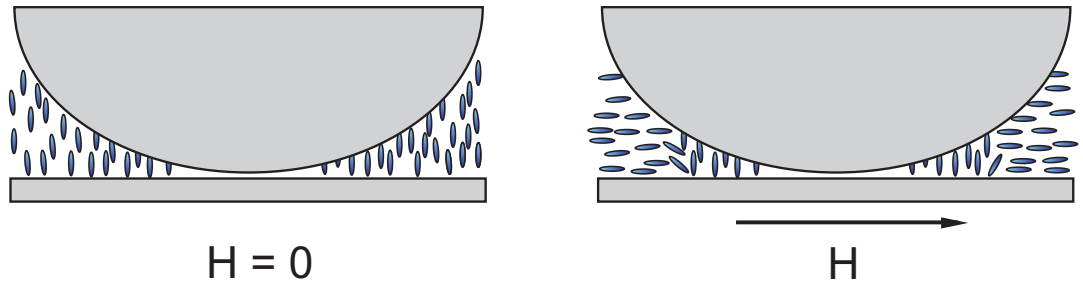

FIGURE 2.4: Geometry of Frederiks' experiment [12].

direction of the external magnetic field. This is generally true for the free bulk of a liquid crystal. However, if a nematic is aligned in a confined geometry, with a field applied perpendicular to the director, molecules will be realigned only when the field strength exceeds some critical threshold value H_c. This effect was called Frederiks transition, as it was first observed and studied by Frederiks in 1927 [12]. In his experiment, the nematic was placed between plane and convex glass surfaces as demonstrated in Figure 2.4. This gave a nematic sample a thickness of that varied with position. In this geometry, it was easy to detect that the critical field H_c was inversely proportional to the sample thickness D.

Frederiks transition can be easily observed in a thin slab of liquid crystal aligned between plane glass slides in different geometries, as demonstrated in Figure 2.5. In all cases, the magnetic field direction is perpendicular to the unperturbed director. Assuming an infinitely strong anchoring condition at the boundaries, the free energy of the system can be expressed as the sum of the elastic energy (2.22) and the magnetic energy (2.26):

$$\mathcal{F}_N = \int_V \frac{1}{2}\left[K_1(\boldsymbol{\nabla}\cdot\boldsymbol{n})^2 + K_2(\boldsymbol{n}\cdot\boldsymbol{\nabla}\times\boldsymbol{n})^2 + K_3(\boldsymbol{n}\times\boldsymbol{\nabla}\times\boldsymbol{n})^2\right] - \frac{1}{2}\chi_a(\boldsymbol{n}\cdot\boldsymbol{H})^2\, dV, \tag{2.27}$$

As a result of surface anchoring and liquid crystal elasticity, there is a competition between the orientation imposed by the boundaries and the orientation imposed by the field. Thus, a nematic will remain unperturbed for a field strength smaller than the critical threshold value and reorient for a field above it. The threshold field of Frederiks transition could be found by solving the free energy (2.27) in the appropriate cell geometry [4]:

$$H_c = \frac{\pi}{D}\sqrt{\frac{K_i}{\chi_a}}, \tag{2.28}$$

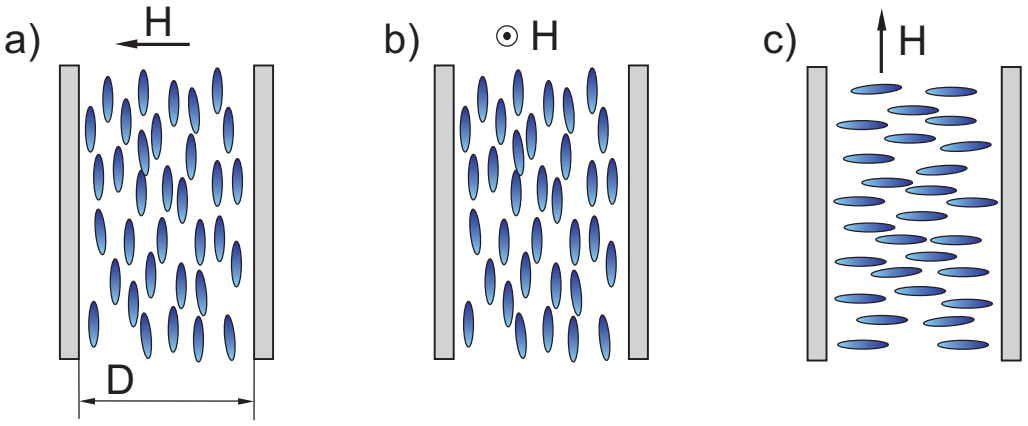

FIGURE 2.5: Geometries for observing Frederiks transition that cause different types of nematic deformation: a) splay; b) twist; c) bend.

where the elastic constant K_i depends on the type of deformation caused by the external field, see Figure 2.5. The work in this thesis only considers planar liquid crystal geometry (Figure 2.5a). The derivation of Equation (2.28) for this case can be found in Section 4.3. It should be mentioned that the critical field is inversely proportional to the sample thickness D, as was demonstrated in Frederiks' early experiment.

In the case of a magnetic field oriented at an angle to the director, the transition threshold disappears and the director deformations begin at a small magnitude of the field [6]. This occurs either when a cell is inclined with respect to the external field direction or when the molecules are tilted in the cell (tilted alignment).

In the case of a finite anchoring energy, the Frederiks transition behaviour is maintained, but the magnitude of the threshold field becomes smaller. The free energy (2.27) in this case should be supplemented by the anchoring energy at the surfaces (2.23):

$$\mathcal{F}_N = \int_V \frac{1}{2}\left[K_1(\boldsymbol{\nabla}\cdot\boldsymbol{n})^2 + K_2(\boldsymbol{n}\cdot\boldsymbol{\nabla}\times\boldsymbol{n})^2 + K_3(\boldsymbol{n}\times\boldsymbol{\nabla}\times\boldsymbol{n})^2\right] - \frac{1}{2}\chi_a(\boldsymbol{n}\cdot\boldsymbol{H})^2\, dV + \int_S \frac{1}{2}W_s \sin^2\gamma\, dS. \tag{2.29}$$

Solving this equation defines the threshold field of Frederiks transition as [10]:

$$H_c(W_s) = H_c(\infty)(1 - 2K_i/W_s D), \tag{2.30}$$

where $H_c(\infty)$ is defined by Equation (2.28). Weak anchoring results not only in a lower threshold, but also in a stronger distortion of the nematic director at a high external field.

Liquid crystal can be also oriented by an electric field [4]. The dielectric constants measured parallel, $\varepsilon_\parallel$, and perpendicular, $\varepsilon_\perp$, to the nematic axis are different. The relation between electric displacement $\boldsymbol{D}$ and field $\boldsymbol{E}$ can be written in the form similar to Equation (2.25),

$$\boldsymbol{D} = \varepsilon_\perp \boldsymbol{E} + \varepsilon_a \boldsymbol{n}(\boldsymbol{n} \cdot \boldsymbol{E}), \tag{2.31}$$

where $\varepsilon_a = \varepsilon_\parallel - \varepsilon_\perp$ is an anisotropy of dielectric permittivity. The electric contribution to the free energy density is:

$$f_{el} = -\frac{1}{8\pi}\boldsymbol{D} \cdot \boldsymbol{E} = -\frac{1}{8\pi}\varepsilon_\perp E^2 - \frac{1}{8\pi}\varepsilon_a(\boldsymbol{n} \cdot \boldsymbol{E})^2. \tag{2.32}$$

Similar to Equation (2.26), only the second term depends on the director orientation with respect to the electric field. So, the first term can be omitted in the modelling of the nematic director orientation.

From Equation (2.32) it can be seen that a nematic with positive dielectric anisotropy favours alignment parallel to the field, while a nematic with negative ε_a favours perpendicular alignment. The sign of the dielectric anisotropy depends on the chemical structure of the molecules. The non-polar molecules or the molecules with a relatively small angle between dipole moment and molecular axis are characterised by positive dielectric anisotropy. Negative dielectric anisotropy typically belongs to materials with a permanent dipole moment normal to the molecular axis.

An effect similar to the magnetic Frederiks transition can be observed in an electric field as well. If the alignment preferred by the electric field is restricted by the alignment induced from the sample boundaries, a liquid crystal will respond to the electric field only when its value is larger than the threshold field given by a formula similar to Equation (2.28) [11],

$$E_c = \frac{\pi}{D}\sqrt{\frac{4\pi K_i}{|\varepsilon_a|}}. \tag{2.33}$$

Then, the threshold voltage can be derived as:

$$V_c = E_c D = \pi \sqrt{\frac{4\pi K_i}{|\varepsilon_a|}}. \tag{2.34}$$

It is worth noting that V_c does not depend on the sample thickness D. So, the critical voltage only depends on the properties of the liquid crystal (elastic constant and dielectric anisotropy), and none of the cell parameters.

2.2.3 Optics of nematic liquid crystals

An aligned sample of a nematic is a uniaxial crystal; its optical axis coincides with the director. Polarized light incident on the liquid crystal sample will experience different refractive indices depending on the direction of propagation and the state of polarization with respect to the director orientation. As a uniaxial crystal, the nematic could be characterised by two refractive indices: ordinary, n_o, and extraordinary, n_e, for the light polarized perpendicular and parallel to the optical axis, respectively.

In typical optical experiments, a light beam often propagates at a certain angle with respect to the director. Let us consider the case when the light propagates in the z direction and the director is aligned at an angle θ_i with respect to it. Then, as was previously derived in Section 2.1.1, the refractive index encountered by the ordinary wave is n_o, and that by the extraordinary wave is n_{eff}, defined in Equation (2.20):

$$n_{eff}(\theta_i) = \frac{n_e n_o}{\sqrt{n_e^2 \cos^2\theta_i + n_o^2 \sin^2\theta_i}}. \tag{2.35}$$

If the nematic sample has some deformations, there is a spatial dependence of the angle $\theta_i(z)$ and, therefore, spatial dependence of the refractive index $n_{eff}(z)$.

As a monochromic light of wavelength λ passes through a nematic layer of thickness D, it acquires the phase lag δ between ordinary and extraordinary waves [5]. If there is no significant variation in the director orientation angle θ_i along the path of the beam, the phase lag can be presented as:

$$\delta = \frac{2\pi}{\lambda}[n_o - n_{eff}(\theta_i)]D. \tag{2.36}$$

For a layer with a variable director orientation angle, $\theta_i = \theta_i(z)$, the total phase lag can be found as:

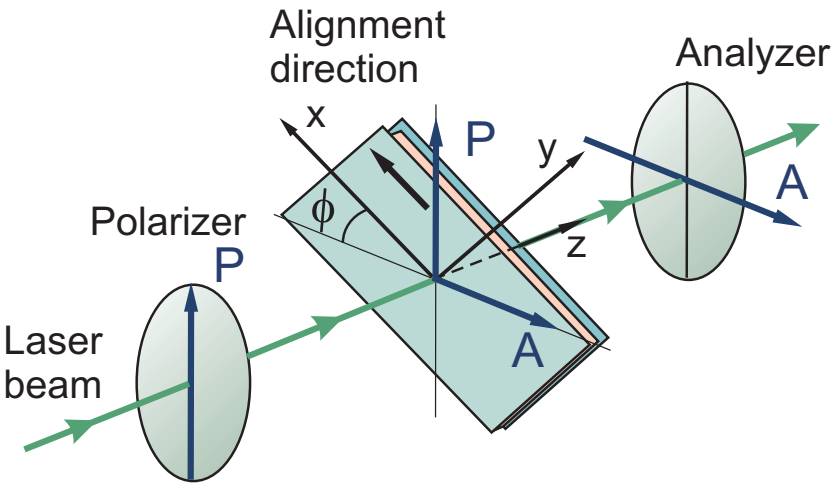

FIGURE 2.6: Schematic of the optical set up for observing birefringence and detecting phase retardation of a planar liquid crystal cell.

$$\delta = \frac{2\pi}{\lambda} \int_0^D [n_o - n_{eff}(\theta_i(z))] \, dz. \tag{2.37}$$

It can be seen that any deviation of the director orientation changes the effective refractive index and, therefore, results in a change of the phase lag between ordinary and extraordinary components of the light passed through the sample. This underlies the principle of the optical method for detecting nematic reorientation, for example, for observing Frederiks transitions.

Let us consider the planar nematic cell, as this cell geometry will be considered in most of the experiments presented later. In the experiments, in order to observe liquid crystal birefringence and detect the phase lag, the cell is usually studied between two linear polarizers, the transmission axes of which are crossed [13]. The cell is placed in such a way that its alignment direction makes a certain angle ϕ with respect to the polarizer as shown in Figure 2.6. The light beam passes through this optical system normal to the cell plane. Assuming the monochromatic plane wave of frequency ω expressed by Equation (2.10) and using the Cartesian system in which the director is aligned in the x direction and the light propagation is in the z direction, the light incident on the cell could be expressed in terms of the electric field vector as:

$$\boldsymbol{E} = \mathcal{E} e^{i\{kz - \omega t\}} \left(\sin\phi \; \hat{\boldsymbol{x}} + \cos\phi \; \hat{\boldsymbol{y}}\right), \tag{2.38}$$

where $\mathcal{E}$ is an amplitude of the electric field and k is the modulus of the wave vector. The polarization of the incident beam is defined by the angle ϕ with respect to the nematic director. The x and y components of the light experience refractive indices n_{eff} and n_o , respectively. As the beam passes through the nematic layer, it undergoes a phase lag δ between the x and y components, which results in a change of the polarization state. The electric component of the light transmitted through the cell becomes

$$\boldsymbol{E'} = \mathcal{E} e^{i\{kz' - \omega t'\}} \left(e^{-i\delta} \sin\phi \ \hat{\boldsymbol{x}} + \cos\phi \ \hat{\boldsymbol{y}} \right). \tag{2.39}$$

The change of the polarization state can be detected by a second polarizer, which is often called the analyzer. The projection of vector $\boldsymbol{E'}$ on the analyzer transmission axis is:

$$E'_{\perp} = -E'_x \cos\phi + E'_y \sin\phi = \mathcal{E} e^{i\{kz' - \omega t'\}} \sin\phi \cos\phi \left(1 - e^{-i\delta}\right). \tag{2.40}$$

Then, the normalized intensity of the beam after transmitting through the analyzer, $I_{\perp}$, can be derived as follows:

$$\begin{aligned} |E'_{\perp}|^2 = \mathcal{E}^2 \sin^2\phi \ \cos^2\phi \ (2 - e^{-i\delta} - e^{i\delta}) = \mathcal{E}^2 \sin^2 2\phi \ \sin^2\left(\frac{\delta}{2}\right), \\ I_{\perp} = \frac{|E'_{\perp}|^2}{\mathcal{E}^2} = \sin^2 2\phi \ \sin^2\left(\frac{\delta}{2}\right). \end{aligned} \tag{2.41}$$

It can be seen that the intensity oscillates with variations of the phase lag δ. The amplitude of oscillations depends on the angle ϕ as $\sin^2 2\phi$. So, the intensity $I_{\perp}$ has a maximum in its amplitude of oscillations when the cell alignment direction is rotated to an angle of $\phi = 45°$ with respect to the polarizers. Therefore, to detect the change in the phase lag, the experiment is usually run with the cell positioned at this angle with respect to the polarizers.

Substituting $\phi = 45°$ into Equation (2.41) simplifies cross-polarized $I_{\perp}$ to

$$I_{\perp} = \sin^2\left(\frac{\delta}{2}\right). \tag{2.42}$$

Thereby, the birefringence of nematic liquid crystals underlines the optical method of detecting the nematic response to an external field [6, 13]. The reorientation of the nematic director changes the effective refractive index of the nematic matrix. This changes the phase lag that the liquid crystal cell can induce between the ordinary and extraordinary components of the beam. In the experiment, phase lag can be detected by placing the cell between two crossed polarizers and monitoring the intensity of the laser beam that passed through this optical system. The rotation of the nematic director inside the cell is observed as an intensity oscillation. The maximum amplitude of oscillation can be obtained than the cell alignment makes 45° angle with the polarizer axes; this geometry is used in the experimental set up. This optical method is used in this thesis to measure the magnetic-field-induced Frederiks transition in a liquid crystal cell with planar geometry. Equation (2.42) is used to extract the change of the phase lag δ from the measured values of the cross-polarized intensity $I_{\perp}$.

On the other hand, the controllable reorientation of liquid crystal alignment results in the possibility to manipulate the effective birefringence of the liquid crystal sample. This makes liquid crystals applicable in a variety of devices, ranging from adjustable wave plates or colour filters to liquid crystal displays (LCDs) [14]. As was shown in Section 2.2.2, because of anisotropy in dielectric and diamagnetic properties, liquid crystal alignment can be controlled either by an electric or by a magnetic field. For the conventional nematics, the anisotropy of dielectric permittivity is relative large (ε_a of the order of ten), allowing the reorientation to be controled by a potential of only a few volts. The anisotropy of diamagnetic permeability, however, is relatively weak ($\chi_a \sim 10^{-7}$), consequently a very strong magnetic field is required to control liquid crystals.

A method of enhancing the magnetic properties of nematics, suggested by Brochard and de Gennes, involves doping them with ferromagnetic particles. Investigations of composite ferronematic suspensions are presented in Chapters 5 and 6. Here, it is worth mentioning that the properties of ferronematic suspensions are strongly depended on the nature of the doped particles. In order to produce a ferronematic sample with good optical quality, the doped particles should be less than a micron in size. However, at this small size, the magnetic properties of particles can change dramatically, as discussed in the next section.

2.3 Magnetic properties of nanoparticles

This section is focused on the magnetic properties of materials, and, in particular, their dependence on particle size. When the particle size reaches the nanometre level, their properties change as compared to the bulk properties of the same materials. These changes arise from the confinement surface effects, as the ratio between surface atoms and bulk atoms increases rapidly with decreasing particle size. This section discusses the changes of ferromagnetic properties in submicron and nanometre sized particles, and in particular, the transition between ferromagnetic and superparamagnetic effects.

Depending on the magnetization of bulk samples in the presence or absence of an external magnetic field, materials can be assigned into the following classes: diamagnetic, paramagnetic, ferromagnetic, ferrimagnetic and antiferromagnetic. This difference in the magnetic properties arises from the different organization of the magnetic dipoles inside the materials [15, 16] (see Figure 2.7). Diamagnetic materials are made up of atoms or molecules that have no magnetic moments. Applying a magnetic field induces weak magnetization in the opposite direction to the external field, so the magnetic susceptibility $\chi < 1$. In paramagnetic materials, the magnetic dipoles are oriented randomly in the absence of a magnetic field; so, they cancel each other and the net magnetization is zero. The external field aligns

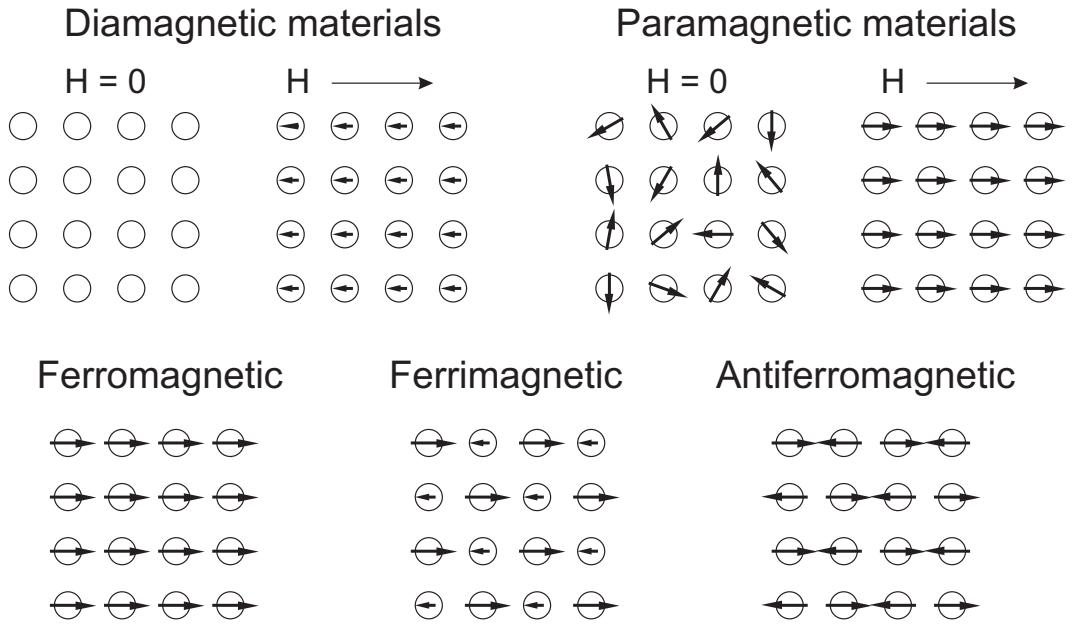

FIGURE 2.7: Schematic of the magnetic dipoles alignment inside diamagnetic, paramagnetic, ferromagnetic, ferrimagnetic, and antiferromagnetic materials.

these dipoles, inducing magnetization in the direction of the field. Paramagnetic materials are characterised by positive magnetic susceptibility: $\chi > 1$. In the ferro-, ferri-, and antiferromagnetic materials there is a long-range order of the magnetic dipoles in the absence of an external field. The bulk material consists of some domains that are characterised by a certain alignment of the magnetic dipoles and separated by domain walls. In ferromagnetic materials all magnetic dipoles inside one domain are aligned in the same direction. Macroscopically, such materials can possess a permanent magnetization. In the ferrimagnetic materials there are weaker dipoles that point in the opposite direction to the stronger dipoles in the absence of an external magnetic field. In the antiferromagnetic materials the adjacent dipoles are pointed in opposite directions, cancelling each other. All of these materials show a very strong response to the external field; their magnetic susceptibility is very large: $\chi \gg 1$ [17].

The magnetic properties of materials can be determined from measurement of the magnetization curve: dependence of the sample magnetization $\boldsymbol{M}$ on the external magnetic field strength $\boldsymbol{H}$. Typical magnetization curves for paramagnetic and ferromagnetic materials are schematically illustrated in Figure 2.8 by blue and black lines, respectively. The magnetization of paramagnetic materials is proportional to the field strength in the small field region and saturates at a high field. The saturation corresponds to complete alignment of magnetic dipoles with the field. The magnetization of ferro- or ferrimagnetic materials shows a hysteresis loop. It is convenient to characterise the magnetization curve by the saturation magnetization M_s (maximum value of M), the remanence magnetization M_r (residual magnetization at zero field) and coercive force H_c (the field required to reduce magnetization to zero). These parameters are different for different materials. They are also volume and temperature dependent [18].

When a ferromagnetic material is heated above the critical temperature, known as the Curie temperature, the hysteresis behaviour disappears. Above this temperature, the long-range order of magnetic dipoles is destroyed by the thermal energy, and the ferromagnetic material becomes paramagnetic. This transition is explained by use of Weiss theory, which can be found in [17]. A similar effect occurs in antiferromagnetic materials. The temperature at which antiferromagnetic order is destroyed is called the Néel temperature.

Magnetic properties of materials also depend on the sample size. In a large sample of ferro- or ferrimagnetics, there is a large number of domains separated by walls, which have a characteristic energy associated with their formation. With

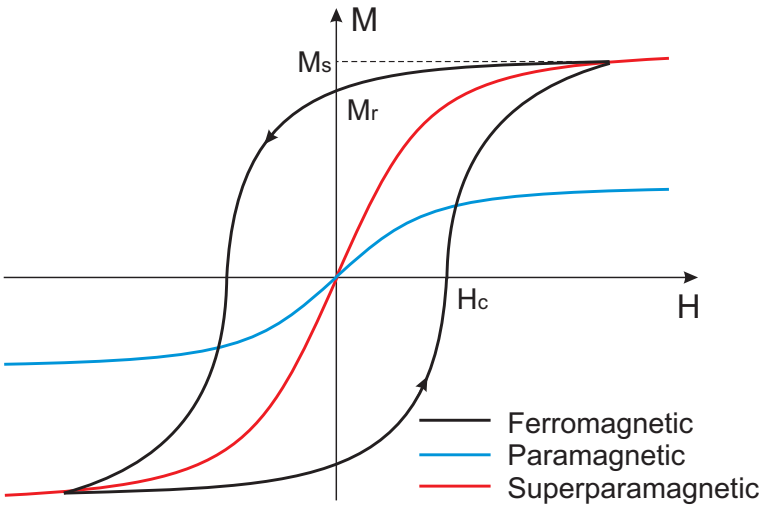

FIGURE 2.8: The typical magnetization curves of paramagnetic, ferromagnetic and superparamagnetic materials.

decreasing particle size, the formation of domain walls becomes energetically unfavourable. So, at a certain critical size d_c, the magnetic particles change from a multi-domain state to a single-domain state. The first estimation of critical size was made by Kittel [19]. For spherical particles with no shape anisotropy, the single-domain size is reported to be 14 nm for Fe particles, 128 nm for Fe_3O_4 and 166 nm for γ-Fe_2O_3 [20]. This critical size is larger for the particles with rodlike shape.

Experimentally, the transition from a multi-domain to a single-domain state can be observed by measuring how the coercive force H_c depends on the particle size d. This dependence is schematically illustrated in Figure 2.9. In the multi-domain sample, the change of magnetization under the influence of an external magnetic field can occur due to changes of domain size (domains with the magnetization in the direction of the applied field grow with increasing field strength). In the single-domain state, the change of magnetization requires the rotation of the whole domain magnetic moment, resulting in a larger coercivity [20].

Figure 2.9 also demonstrates another transition that occurs with a decrease of particle size d, when H_c becomes zero. The thermal energy in a small particle can cause the flip of magnetization direction in a short period of time, known as the Néel relaxation time τ_N:

$$\tau_N = \tau_0 \exp\left(\frac{\Delta E}{k_b T}\right), \tag{2.43}$$

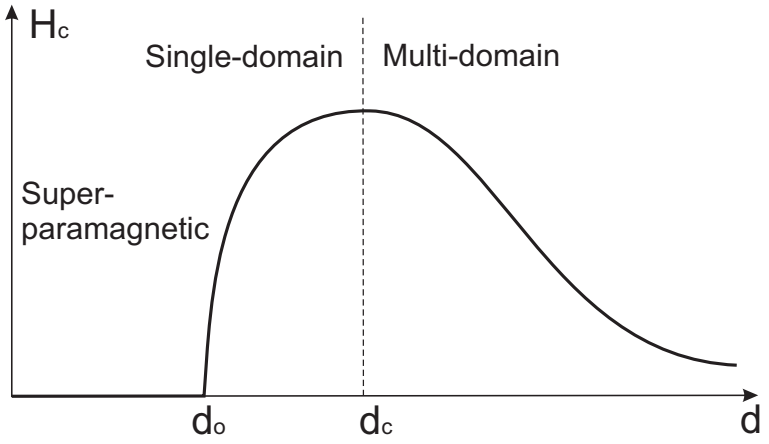

FIGURE 2.9: Typical dependence of the coercive force H_c on particle size d for ferromagnetic particle.

where τ_0 is a characteristic time scale of materials, typically of the order of 10^{-9} to 10^{-13} second [21]; $\Delta E = K_v v$ is the energy barrier associated with the spin flip, $v \sim d^3$ is the particle volume and K_v is the energy density of magnetic anisotropy; $k_b T$ is the thermal energy. It should be noticed that τ_N depends critically on the particle size d as $\exp\{d^3\}$. Assuming $\tau_0 = 10^{-9}$ s, $K_v = 10^6$ erg/cm^3, and $T = 300$ K, the change of particle diameter from 11.4 nm to 14.6 nm will increase relaxation time from 0.1 s to 10^8 s [20].

If the Néel relaxation time is shorter than the measuring time scale τ, the magnetic moment can flip several times during the time τ, and the average magnetic moment of the particle becomes zero. However, the particles can be easily magnetized by an external field. The magnetization curve resembles the curve of paramagnetic materials, but the magnetic susceptibility and the saturation magnetization are significantly larger (see Figure 2.8). This phenomenon is known as superparamagnetism [16, 22].

The superparamagnetic state is temperature dependent. It is characterised by a so-called blocking temperature T_b, a transition point above which particles are in a superparamagnetic state. Below this temperature the particle magnetization does not relax during the measurement time; their ensemble demonstrates a magnetic hysteresis. If $\tau = 100$ s and $\tau_0 = 10^{-9}$ s, the blocking temperature can be derived from the relation $\tau = \tau_N$ as [20]:

$$T_b = \frac{\Delta E}{25 k_b}. \tag{2.44}$$

Equation (2.44) specifies the blocking temperature at a zero magnetic field. With an increase of the external field H, the blocking temperature decreases as the following function: $T_b \sim (1 - H/H_s)^a$, where $a = 2$ for low fields and $a = 2/3$ for high fields, $H_s = 2K_v/M_s$ [21].

The simplest model of superparamagnetic behaviour describes a system of N non-interacting identical particles with the magnetic moment μ_0. Considering the interaction of magnetic moments with the external field H, it is possible to calculate the resulting system magnetization M. In the case of isotropic particles, the magnetization M is described by the Langevin equation [21]:

$$M = N\mu_0 \left[\coth\left(\frac{\mu_0 H}{k_b T}\right) - \frac{k_b T}{\mu_0 H} \right]. \tag{2.45}$$

At low fields, the magnetization is linear with H, which corresponds to magnetic susceptibility $\chi = N\mu_0^2/(3k_bT)$.

2.3.1 Relaxation process in colloids of magnetic particles

Magnetic nanoparticles are often investigated as a colloid in some fluid. To stabilize this colloid, it is necessary to coat the particles by some surfactants that form an organic shell around the particle core.

The response of a magnetic colloid to an external field is usually investigated by measuring magnetization relaxation [23]. If the external field that has been applied to a colloidal system for a sufficient time is switched off, the system magnetization shows an exponential decay with time. The characteristic relaxation time τ_{relax} is mainly determined by two processes: Néel relaxation and Brownian relaxation. The Néel relaxation, which dominates the response of small superparamagnetic nanoparticles, has been described above. The characteristic relaxation time is expressed by Equation (2.43). Brownian relaxation is connected with the physical rotation of particles in a solvent. In this case, the magnetic moment is coupled to the particle crystallographic structure. The characteristic relaxation time τ_B depends on the hydrodynamic volume of the particle v_{hydr} (the particle volume including surfactant layer) and the viscosity of the carrier liquid η:

$$\tau_B = \frac{3\eta v_{hydr}}{k_b T}. \tag{2.46}$$

In a magnetic colloid where particles are free to rotate, both mechanisms contribute to the magnetization relaxation. The characteristic relaxation time, τ_{relax}, can be determined as [23, 24]:

$$\tau_{relax} = \frac{\tau_N \tau_B}{\tau_N + \tau_B}. \tag{2.47}$$

The process with the shortest relaxation time τ_N or τ_B is dominant. The Néel relaxation time is smaller for small particles; however, it increases rapidly with particle size ($\tau_N \sim \exp\{d^3\}$). So, the Brownian process usually dominates in a colloid of large particles. The critical particle size can be found from the relation: $\tau_N = \tau_B$; it depends not only on particle parameters, but also on the properties of solvent and surfactant layer.

In the case of immobilized particles (solidified or dried sample), the Brownian relaxation is inhibited. Then, the relaxation process becomes slower as it is determined by the Néel relaxation time only.

Summary

A liquid crystal is a phase of matter that combines the properties of both liquids and crystals. There are different liquid crystalline phases, depending on the degree of molecular order. In this work only nematic liquid crystals are considered. This is the least ordered phase in which molecules are free to flow, but demonstrate orientational order. This produces anisotropy of their electrical, magnetic, and optical properties, and also in their elasticity. An alignment in a nematic sample can be induced either by the surfaces (by special treatment of the boundary substrates) or by applying an external magnetic or electric field. When the alignments induced by the field and surfaces are orthogonal to each other, an effect known as Frederiks transition occurs in the cell. At a low field, surface-induced alignment is maintained in the sample by bulk elastic forces. The alignment preferred by the field is induced only when the field strength is higher than a threshold value.

The nematic phase can be described by the continuum theory, which deals with the nematic director; i.e. the unit vector that describes the preferable molecular orientation in the sample. There are three possible deformations of the director: splay, twist and bend. Any of these distortions, or the influence of the external fields, are characterized by a contribution to the free energy functional. An equilibrium distribution of the director field corresponds to a minimum in the free

energy. Continuum theory is used in this thesis to model the response of nematics and of ferronematic suspensions to a magnetic field.

An aligned nematic sample shows a birefringence effect. It is characterized by two refractive indices along and across the nematic director. It is possible to observe liquid crystal birefringence by placing a thin nematic sample between two crossed polarizers. This underlines the optical method of detecting liquid crystal reorientation. Any deviation of the nematic director in the sample causes a change in the refractive index encountered by the extraordinary polarized wave. This leads to a change in the phase lag between the ordinary and the extraordinary waves. Variation of the phase lag causes oscillations in the intensity of the laser beam that passes through the liquid crystal sample placed between two crossed polarizers, which can be detected experimentally. Moreover, the possibility to control liquid crystal alignment creates a sample with controllable optical properties. This has enabled liquid crystals to find wide application in a variety of opto-electronic devices.

There are different classes of materials depending on their magnetic properties: diamagnetic, paramagnetic and ferromagnetic. Liquid crystals are diamagnetic, demonstrating weak anisotropy in diamagnetic permeability. This makes them sensitive to the magnetic field, but their magnetic sensitivity is rather low. Ferromagnetic materials are very sensitive to the magnetic field. The ferromagnetic properties depend on both the temperature and the sample size. With increasing temperature, ferromagnetics undergo a phase transition at a Curie temperature and become paramagnetics. A large sample of ferromagnetic material usually contains a large number of domains with a certain magnetization. A ferronematic particle can contain only a single magnetic domain when its size is smaller than some specific critical value. With any further reduction of the particle diameter to nanometre size, superparamagnetic behaviour occurs. In this case, the particle magnetization appears to have an average value of zero. However, an external magnetic field is able to magnetize the nanoparticles, similarly to a paramagnetic, but with much larger magnetic susceptibility.

References

[1] M. Born and E. Wolf. *Principles of Optics, Electromagnetic theory of propagation, interference and diffraction of light.* Pergamon Press, Oxford, 6th edition, 1980.

[2] D. J. Griffiths. *Introduction to Electrodynamics.* Prentice-Hall, Upper Saddler River, N.J., 3rd edition, 1999.

[3] S. A. Akhmanov and S. Yu. Nikitin. *Physical Optics.* Clarendon Press, Oxford, 1997.

[4] P. G. de Gennes and J. Prost. *The Physics of Liquid Crystals.* Clarendon Press, Oxford, 2nd edition, 1993.

[5] I.-C. Khoo. *Liquid Crystals.* Wiley, 2nd edition, 2007.

[6] L. M. Blinov. *Electro-optical and Magneto-optical Properties of Liquid Crystals.* Wiley, Chichester, 1983.

[7] C. W. Oseen. The theory of liquid crystals. *Transactions of the Faraday Society*, 29:883–899, 1933, from *Crystals That Flow*, pages 255-272, 2004.

[8] F. C. Frank. On the theory of liquid crystals. *Discussions of the Faraday Society*, 25:19–28, 1958, from *Crystals That Flow*, pages 389-399, 2004.

[9] P. J. Collings. *Liquid Crystals: Nature's Delicate Phase of Matter.* Princeton University Press, Princeton, New Jersey, 1990.

[10] A. Rapini and M. J. Papoular. Distorsion d'une lamelle nematique sous champ magnetique: conditions d'ancrage aux parois. *Journal de Physique. Colloques*, 30(C4), 1969.

[11] L. M. Blinov and V. G. Chigrinov. *Electrooptic Effects in Liquid Crystal Materials.* Springer, New York, 1994.

[12] A. Repiova and V. Frederiks. K voprosy o prirode anisotropno-zhidkogo sostoyaniya veshestva (On the problem of the nature of the anisotropic liquid state of matter) (in russian). *Journal of Russian Physical Chemistry Society*, 59:183–200, 1927.

[13] I.-C. Khoo and S.-T. Wu. *Optics and Nonlinear Optics of Liquid Crystals.* World Scientific, Singapore, 1993.

[14] L. M. Blinov and V. G. Chigrinov. *Liquid Crystal Devices: Physics and Applications*. Artech-House, Boston-London, 1999.

[15] D. Wagner. *Introduction to the Theory of Magnetism*. Pergamon Press, Oxford, 1972.

[16] U. Jeong, X. Teng, Y. Wang, H. Yang, and Y. Xia. Superparamagnetic colloids: controlled synthesis and niche applications. *Advanced Materials*, 19: 33–60, 2007.

[17] F. Brailsford. *Physical Principles of Magnetism*. 1966.

[18] J. C. Anderson. *Magnetism and Magnetic Materials*. Chapman and Hall LTD., London, 1968.

[19] C. Kittel. Theory of the structure of ferromagnetic domains in films and small particles. *Physical Review*, 70:965–971, 1946.

[20] D. L. Leslie-Pelecky and R. D. Rieke. Magnetic properties of nanostructured materials. *Chemistry of Materials*, 8:1770–1783, 1996.

[21] S. P. Gubin, Yu. A.Koksharov, G. B. Khomutov, and G. Yu. Yurkov. Magnetic nanoparticles: preparation, structure and properties. *Russian Chemical Reviews*, 74:489–520, 2005.

[22] C. P. Bean and J. D. Livingston. Superparamagnetism. *Journal of Applied Physics*, 30(4):120S–129S, 1959.

[23] D. Eberbeck, F. Wiekhorst, U. Steinhoff, and L. Trahms. Aggregation behaviour of magnetic nanoparticle suspensions investigated by magnetorelaxometry. *Journal of Physics: Condensed Matter*, 18:S2829–S2846, 2006.

[24] W. Möller, S. Takenaka, N. Buske, K. Felten, and J. Heyder. Relaxation of ferromagnetic nanoparticles in macrophases: in vitro and in vivo studies. *Journal of Magnetism and Magnetic Materials*, 293:245–251, 2005.

Chapter 3

Experimental methods of characterising the magneto-optic and electro-optic properties of liquid crystals

This chapter concentrates on describing experimental methods that are used in this thesis to investigate both undoped nematics and ferromagnetic nanoparticle suspensions in nematics (ferronematics). It starts with the characterisation of nematic liquid crystals, which are used as a base for the ferronematic suspensions. However, the preparation method of ferronematics, together with the detailed characteristics of different nanoparticles, will be given in Chapter 5. The fabrication techniques for liquid crystal cells and the experimental methods of determining the cell characteristics, such as cell thickness and liquid crystal alignment, including easy axis pretilt on the surfaces, are given in Section 3.2. Liquid crystal cells are used in the following magneto-optic and electro-optic experiments, which are described in Section 3.3 and Section 3.4, respectively. These sections briefly discuss some of the experimental results, pointing out how the liquid crystal properties can be extracted from the measurements. Further experimental data with detailed analysis will be presented for nematic cells in Chapter 4 and for cells with different ferronematic suspensions in Chapter 5 .

3.1 Properties of nematic liquid crystals

A commercially available nematic liquid crystal E7 (Merk Ltd.) is used in most of the experiments. In some cases, nematic 5CB (Merk Ltd.) is tested as well. Both of these liquid crystals have only one - nematic - liquid crystal phase, which exists at room temperature. 5CB has the nematic state between 22.5°C and 35.3°C; E7 exists in the nematic state between -10°C and 59.8°C. 5CB is a single component liquid crystal consisting of 4-pentyl-4'-cyanobiphenyl molecules; E7 is a mixture of four types of cyanobiphenyl molecules, the content and molecular structure of which are presented in Figure 3.1. The main component (51%) of E7 consists of 5CB molecules. However, due to the addition of the other components, E7 has a wide temperature range for the existence of the nematic phase compared to 5CB (see Figure 3.1 for comparison). This makes it more suitable for use in the experiments.

Some characteristics of the nematics E7 and 5CB, including the elastic constants, refractive indices, diamagnetic anisotropy, and dielectric constants, are listed in Table 3.1. Both E7 and 5CB are characterized by a relatively large anisotropy of refractive indices ($n_a = (n_e - n_o) \sim 0.22$ for E7 and $n_a \sim 0.17$ for 5CB, where n_e, n_o are the extraordinary and ordinary refractive index, respectively). They have positive anisotropy of dielectric constants and positive anisotropy of diamagnetic susceptibility. Because of this, in order to observe Frederiks transition in the cells containing these nematics, or suspensions based on them, experiments are conducted on cells with planar liquid crystal alignment and with an electric or a magnetic field applied perpendicular to the cell plane.

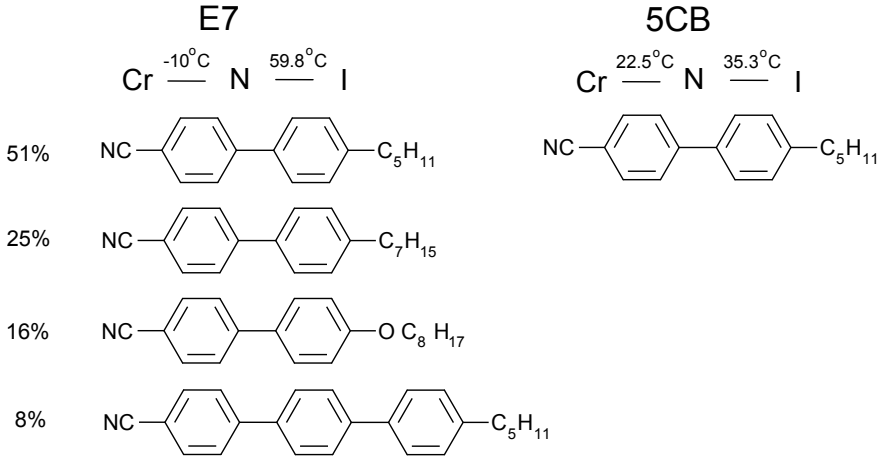

FIGURE 3.1: Molecular structure of nematic liquid crystals E7 and 5CB.

TABLE 3.1: Material properties of nematics E7 and 5CB

		E7			5CB	
Elastic constants, $\times 10^{-7}$ erg/cm	K_1	11.2	[1]		6.4	[2]
	K_2	6.8	[1]		3	
	K_3	17.8	[3]		10	
Refractive indices						
at 633 nm ($T = 25°C$)	n_o	1.5189	[4]		1.532	[5]
	n_e	1.7305			1.706	
at 589.3 nm ($T = 20°C$)	n_o			1.5217*	-	
	n_e			1.7472*	-	
at 532 nm ($T = 25°C$)	n_o	1.5268	[4]		-	
	n_e	1.7512			-	
Dielectric constants	$\varepsilon_\perp$	5.17	[6]	5.1*	6.9	[7]
	$\varepsilon_\parallel$	19.54		19.3*	17.9	
Diamagnetic anisotropy	χ_a	$\sim 10^{-7}$	[8]		$\sim 10^{-7}$	[8]

* E7 characteristics taken form Merck data sheet.

3.2 Liquid crystal cells

Two types of liquid crystal cells are used in the experimental investigations, which will be referred to as a normal cell and a guard electrode cell. The normal cell is used for magneto-optic measurements, while the guard electrode cell is used for electro-optic measurements.

The normal liquid crystal cell consists of two glass substrates covered with the alignment layers, and a thin layer of liquid crystal between them, as demonstrated in Figure 3.2. To achieve planar liquid crystal alignment, polyimide (Pyralin PI 2525 from HD microsystems) is used. The solution of PI 2525 in solvent 1-methyl-2-pyrrolidinone (ratio 1:10) is spin coated on the glass substrate, which

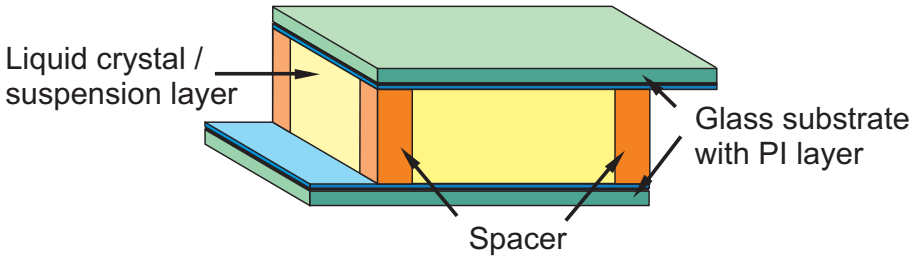

FIGURE 3.2: Structure of the liquid crystal cell.

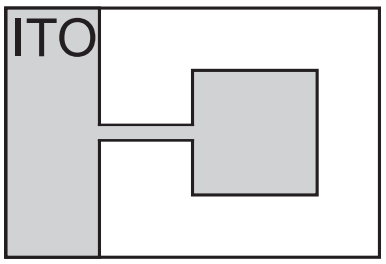

FIGURE 3.3: Glass substrate with patterned indium tin oxide (ITO) layer.

is then baked at 225 °C for an hour to evaporate the solvent and stabilize the polymer layer. Polymer coated substrates are rubbed with a velvet cloth using a machine which allows precise control of a rubbing direction with respect to the edges of the substrate. Rubbing produces microgrooves on the polymer layer which promotes the alignment of liquid crystals in that direction. Two substrates are joined together in such a way that there are antiparallel rubbing directions on opposite sides of the cell. This technique ensures a uniform planar alignment inside the cell without defects and twist deformations.

Two glass substrates are separated by glass bead spacers, with well defined size of either 12 or 50 μm. Initially, the spacers are dispersed in UV-curing glue (Norland Optical Adhesive 61). The drops of glue with spacers are placed in the corners of one substrate, which is then covered with the second one. The two substrates are gently pressed together to obtain a monodispersed layer of spacers. Uniformity of the gap between them is controlled by observing interference fringes. Each fringe corresponds to a thickness variation of the order of half the wavelength of light. 50 μm cell is considered to be uniform if there are not more than three fringes across its area, which correspond to the thickness variation less than 1 μm [5]. Uniformity of 12 μm cell is controlled more precisely, allowing only one interference fringe across its area. The cell is then exposed to ultra-violet light to cure the glue.

The glass substrates of a guard electrode cell, unlike the normal cell, have patterned transparent electrodes on them. The electrodes are the etched layers of indium tin oxide (ITO), the shape of which is presented in Figure 3.3. The square electrode in the centre has an area of 1×1 cm^2. Apart from that special electrode design, the cell is prepared in the same way as the normal cell. During assembly, the square electrode from the top substrate is superimposed on the square electrode from the bottom substrate. This creates a liquid crystal layer between the two electrodes with a known area. The drops of UV-curing glue with spacers are confined to the region without the ITO layer. This ensures that all possible liquid

crystal defects, appearing near the drops of glue at the cell edges, lie outside the electrode region. Voltages can then be applied to the cell by attaching contacts to the parts of the electrodes at the edge of each substrate.

The Frederiks threshold magnetic field is inversely proportional to the cell thickness (see Equation (2.28)). Therefore, to shift the threshold to lower values, the cells used in the magneto-optic experiments are normally quite thick, around 50 μm. For the electric field experiments, however, the threshold voltage does not depend on the cell thickness (see Equation (2.34)), so the guard electrode cells are usually made thinner, using 12 μm spacers.

The cells are filled with undoped liquid crystals or their suspensions with nanoparticles in the isotropic phase. For this, the cell is placed on a hot stage, heated above clearing temperature and then filled with the suspension using capillary forces. When the hot stage is switched off, the cell stays on it as it slowly cools down to room temperature. The slow cooling process ensures that there is no redistribution of particles in liquid crystal suspensions during transition to the nematic state - the effect observed during rapid lowering of temperature. In some cases the cells are filled at room temperature with suspensions in nematic phase. No difference in the alignment and cell homogeneity is detected in cells filled either in isotropic or in nematic phases. Each cell is then sealed around the edges with epoxy glue to prevent the liquid crystal leaking out.

3.2.1 Cell thickness measurement

The cell thickness can be verified by the interferometric method [5]. In this method, an empty cell is illuminated by a white light source. A spectrum of the light transmitted through the cell is determined by an Ocean Optics USB4000 spectrometer. The transmitted light consists of the light that passes through the cell with no reflection, and the light that reflects from the front and the back substrates. The optical path difference between these two beams is

$$\Delta S = 2Dn, \tag{3.1}$$

where D is the cell thickness and n is the refractive index of the medium inside the cell (for the empty cell $n = 1$). Transmitted beams interfere beyond the cell, which appears in the spectrum as maxima and minima. The wavelength of the spectrum maxima satisfy the condition

$$\Delta S = m_i \lambda_i, \tag{3.2}$$

where m_i is an integer. The difference between numbers m_i and m_{i+1} corresponding to the neighbouring maxima is 1. To calculate the cell thickness, two transmission maxima with the wavelength λ_1 and λ_2 are selected from the spectra. The number of the interference cycles between them is $m = m_1 - m_2$. Using Equations (3.1) and (3.2), the cell thickness, D, can be calculated as:

$$D = \frac{m}{2n} \frac{\lambda_1 \lambda_2}{\lambda_2 - \lambda_1}. \tag{3.3}$$

3.2.2 Control of liquid crystal alignment

The alignment of the cells is checked by inspecting them between two crossed, linear polarizers. Planar alignment corresponds to the change of the cross-polarized image from uniform bright to uniform dark when the cell is rotated with respect to the polarizer axes. When the cell alignment direction is perpendicular or parallel to the transmission axis of the first polarizer, the incident light encounters only one, ordinary or extraordinary, refractive index, respectively. The light polarization remains unchanged after the cell. Therefore, all light is blocked by the second polarizer, resulting in a dark cell image. When the cell is placed at some angle other than 0° or 90° to the polarizer axis, the light experiences two refractive indices, n_o and n_e. Passing through the liquid crystal, the two polarizations become out of phase and in general emerge as elliptically polarized light. Some light can therefore pass through the second polarizer, creating a bright image. Homeotropic alignment corresponds to a dark cross-polarized image regardless of the cell orientation between the two polarizers. The incident light always experiences the ordinary refractive index, as the liquid crystal director remains perpendicular to the polarization upon rotation. So, the cell appears dark after the second polarizer [9].

Any possible defects or non-uniformities in the nematic alignment are visible as bright, dark, or multicoloured nonuniform regions or spots on the cross-polarized image. If the nematic orientation is not homogeneous, but varies slowly in the plane of the substrates, so-called Schlieren textures are observed between crossed polarizers [10]. Schlieren textures exhibit characteristic sets of often curved dark and bright stripes that come together at some singular points. These singularities are topological point defects. Another possible texture for unaligned nematic

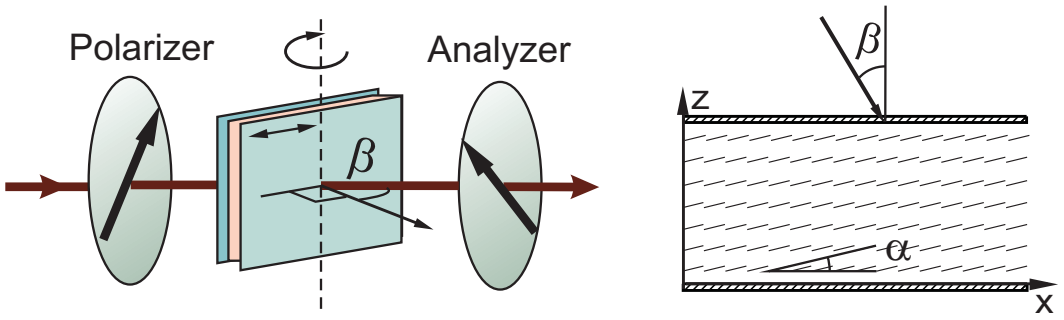

FIGURE 3.4: Schematic of the set up for measuring pretilt angle by the crystal rotation method, and cell geometry demonstrating pretilt angle.

samples is a thread-like texture. It contains dark lines, which either connect two point defects or form closed loops. These line singularities are called disclination lines. Detailed descriptions of nematic defects and images of different textures can be found in the literature [9, 10]. However, this topic is beyond the scope of the present thesis.

A cell with polyimide antiparallel rubbed layers usually produces uniform, planar liquid crystal alignment with a small pretilt angle $\sim 3°$. The pretilt angle for each cell is measured separately by the crystal rotation method [11, 12]. In this experiment, the cell is set between a polarizer and an analyzer, whose transmission axes are perpendicular to each other and make an angle of 45° angle with respect to the liquid crystal alignment direction. The cell is rotated around the perpendicular to the alignment direction axis, as demonstrated in Figure 3.4. The cell is illuminated by He-Ne laser beam with $\lambda = 543$ nm. The transmitted beam intensity is measured for various angles of cell rotation, β. An example of the transmitted intensity obtained for a cell filled with nematic E7 is presented in Figure 3.5. This curve is described by the following function:

$$I_{\perp}(\beta) = \sin^2\left(\frac{\delta(\beta)}{2}\right),$$

$$\delta(\beta) = \frac{2\pi D}{\lambda}\left(\frac{n_o n_e\sqrt{n^2(\alpha) - \sin^2\beta}}{n^2(\alpha)} - \sqrt{n_o^2 - \sin^2\beta}\right.$$
$$\left. - \frac{n_e^2 - n_o^2}{n^2(\alpha)}\sin\alpha\cos\alpha\sin\beta\right), \tag{3.4}$$

where

$$n(\alpha) = \sqrt{n_o^2\cos^2\alpha + n_e^2\sin^2\alpha},$$

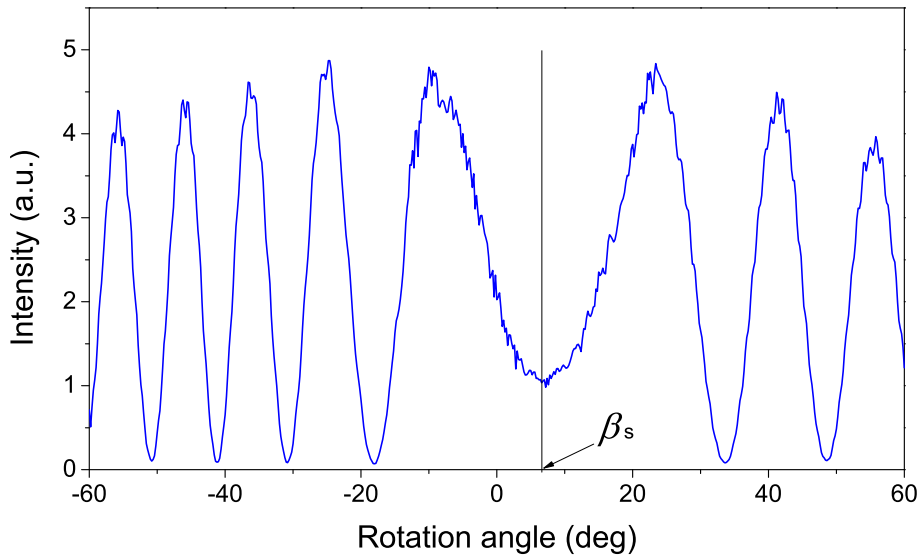

FIGURE 3.5: Typical curve of the transmitted intensity depending on the rotation angle measured by the crystal rotation method for the E7 cell.

n_o and n_e are the ordinary and extraordinary refractive indices, α is the pretilt angle. The detailed derivation of Equation (3.4) can be found in [12]. The symmetry point of the transmitted intensity corresponds to the maximum of the phase lag $\delta(\beta)$. So, the symmetry point, β_s, should satisfy an equation obtained by setting the derivative $d\delta/d\beta$ equal to zero:

$$\left[\frac{1}{\sqrt{n_o^2-\sin^2\beta_s}}-\frac{n_o n_e}{n^2(\alpha)\sqrt{n^2(\alpha)-\sin^2\beta_s}}\right]\sin\beta_s=\frac{n_e^2-n_o^2}{n^2(\alpha)}\sin\alpha\cos\alpha. \qquad (3.5)$$

For small pretilt angles, α, Equation (3.5) can be approximated to the following:

$$\sin 2\alpha=\frac{-2\sin\beta_s}{(n_o+n_e)\sqrt{1-(\sin\beta_s/n_o)^2}}. \qquad (3.6)$$

This equation is used to evaluate the pretilt angle α using the angle β_s measured from the experimental curve. The noise in the signal that is usually observed around the symmetry point creates some difficulties in the detection of angle β_s. This can be resolved by detecting the symmetry position as a middle point between two first order minima, which can be easily detected (see Figure 3.5). The pretilt angle determined from this experimental curve is 2.7°; refractive indices n_o and n_e for calculation are taken from Table 3.1.

Crystal rotation method is a very simple method that provides accurate results with a margin of error within $\pm 0.05^\circ$ [12]. It is entirely suitable for determining the pretilt angle in the experimental cells discussed here. However, it has one disadvantage: it is restricted to small pretilt angles, usually less that 10°. In the case of larger pretilt, other methods, such as a magnetic null method [11] or a conoscopic method [13], can be used.

3.3 Frederiks transition experiments in magnetic fields

The response of liquid crystals or ferronematic suspensions to a magnetic field is investigated by measuring the magnetic-field-induced Frederiks transition. In this experiment, the optical method of detecting liquid crystal reorientation is adopted [14]. The first set of ferronematic suspensions was tested using a magneto-optic arrangement from Institute of Physics, Kiev, Ukraine. Later, a similar arrangement was constructed at the University of Southampton, where the majority of ferronematic samples were measured.

The magneto-optic arrangements are schematically represented in Figure 3.6. The planar cell containing either nematic or ferronematic suspension is placed between two crossed polarizers in such a way that the liquid crystal director makes a 45° angle with the polarizer axes. This optical system is set by hand, however an accurate arrangement is ensured by following procedure. Firstly, the cell is aligned with the transmission axis of one of the crossed polarizers by rotating the cell until a minimum in transmitted output intensity is observed. After that, each polarizer is rotated at 45° using a scale on the polarizer holder. The cell between crossed polarizers is held between the two poles of an electromagnet, which create a "test" magnetic field, $\boldsymbol{H}$, of strength up to 2 kOe in the direction perpendicular to the cell plane. This component of the magnetic field induces liquid crystal reorientation. The test magnetic field strength is measured by a Hall probe sensor with a maximal error of 10 Oe. There is also a small bias field, $\boldsymbol{H}_b$, up to 30 Oe, applied along the initial alignment direction of the liquid crystal. This field is produced by Helmholtz coils placed above and below the cell (not shown on diagram). The bias field is needed to orient the magnetic moments of ferroparticles in ferronematic suspensions in the absence of the test field. For consistency, it is also applied during the measurements with undoped liquid crystals.

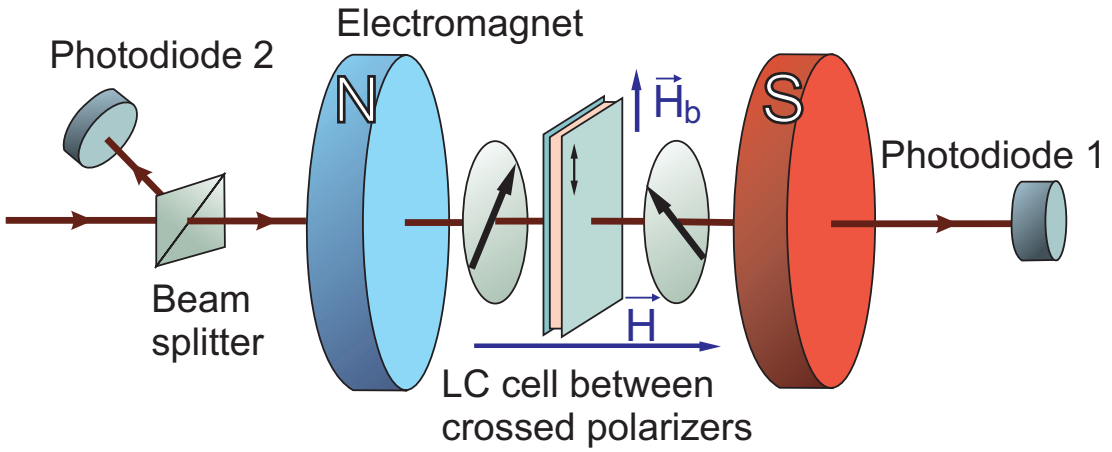

FIGURE 3.6: Schematic of experimental set up for detecting magnetic-field-induced Frederiks transition. Arrows on the polarizer and analyzer indicate their polarization axes, arrow on the liquid crystal (LC) cell indicates alignment direction.

The liquid crystal orientation inside the cell is measured using an optical method. A He-Ne laser beam with $\lambda = 633$ nm propagates through the optical system in the direction perpendicular to the cell plane, passing through holes in the magnet pole pieces. The intensity of this beam after passing through the cell is monitored by the Photodiode 1. There is also a beam splitter placed before the cell and an additional photodiode (Photodiode 2) that controls the intensity of the incident beam, and hence the laser stability.

Data acquisition is performed by a program written in LabVIEW. At each step of the measurements, it sets a voltage applied to the electromagnet and records the data from both photodiodes and the Hall sensor for a given interval. An example of raw data collected at one step of the measurement when the test magnetic field $H \simeq 1.6$ kOe is presented in Figure 3.7. It has been found experimentally that the time interval for each step, during which a liquid crystal relaxes to the equilibrium state, should be around 60 seconds. As can be seen in Figure 3.7, this time interval is sufficient for the intensity of the beam transmitted through the cell to reach the saturated value. The intensity of this beam, collected by Photodiode 1, is normalized to the intensity of the reference beam, collected by Photodiode 2, in order to eliminate any possible influence of the laser intensity fluctuation with time. To minimize the signal noise, the program averages the normalized intensity value over the large number of data collected over the final three seconds of the recorded time. The result is plotted as a normalized cross-polarized intensity dependence on the test magnetic field. Both photodiodes measure an intensity with an accuracy

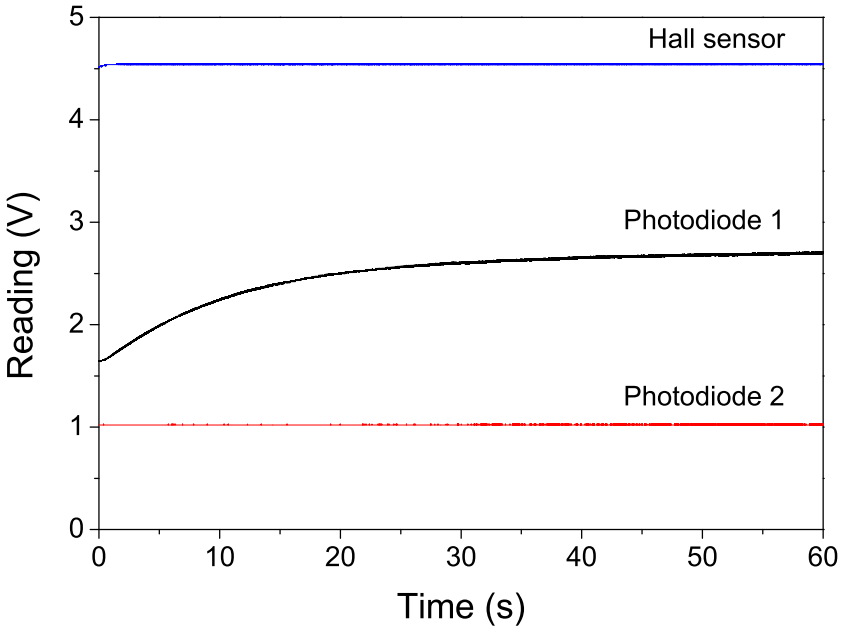

FIGURE 3.7: Example of the experimental data collected at one step of the Frederiks transition experiment in a magnetic field. Photodiode 1 monitors the intensity of the laser beam transmitted through the cell; Photodiode 2 controls the intensity of the reference beam; Hall sensor measures the test magnetic field.

of 0.05%, which makes the relative error for normalized cross-polarized intensity 0.1%.

The fact that the liquid crystal comes to an equilibrium during each step of the experiment is verified by the following trial measurement: the normalized cross-polarized intensity is monitored depending on the test magnetic field for an increasing and for a decreasing magnetic field. The resulting curves for the cell filled with nematic E7 is presented in Figure 3.8. Comparison and excellent overlap between the two curves ensures that the liquid crystal alignment has reached a steady state during the measured time interval.

The measured dependence of the cross-polarized intensity allows the determination of the phase lag induced by a liquid crystal layer between the ordinary and the extraordinary component of the transmitted light. Based on Equation (2.37), the phase lag has a maximum absolute value, $\delta_{max} = 2\pi D(n_o - n_e)/\lambda$, in the absence of the magnetic field. The magnetic-field-induced reorientation of the liquid crystal results in the change of the phase lag and, therefore, in the change of the cross-polarized intensity, $I_\perp$. Thus, the change of the phase lag, $\Delta\delta = \delta - \delta_{max}$, can be recovered from the cross-polarized intensity using the relation (2.42):

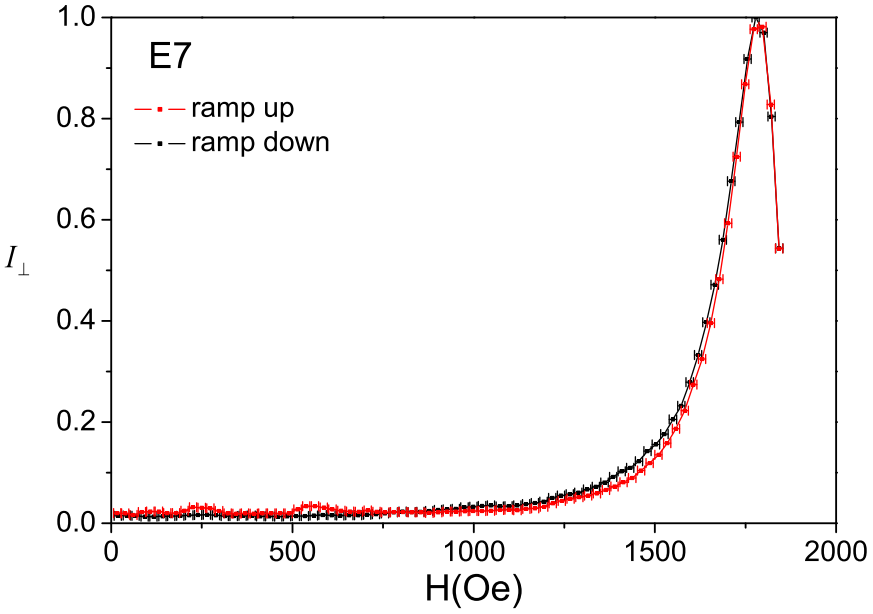

FIGURE 3.8: Normalized cross-polarized intensity ($I_\perp$) measured in the nematic E7 cell for an increasing and for a decreasing magnetic field. The relative error for $I_\perp$ is 0.1% (not shown on the plot).

$$I_\perp = \sin^2\left(\frac{\delta}{2}\right) . \tag{3.7}$$

The typical dependence of the normalized cross-polarized intensity on the test magnetic field, for nematic liquid crystal E7 is presented on the upper plot in Figure 3.9. The value of the magnetic field where the cross-polarized intensity starts to oscillate corresponds to Frederiks transition threshold. The oscillations of the cross polarized intensity correspond to reorientation of the director. One full oscillation is related to the change of the phase lag by 2π. The lower plot in Figure 3.9 demonstrates the dependence of $\Delta\delta$ on H obtained from the cross-polarized intensity. Frederiks transition is not "sharp" because the initial director alignment is not exactly perpendicular to the magnetic field: there are small director pretilt and in-plane bias magnetic field. The effect of both of these on the Frederiks transition will be discussed in Section 4.2.

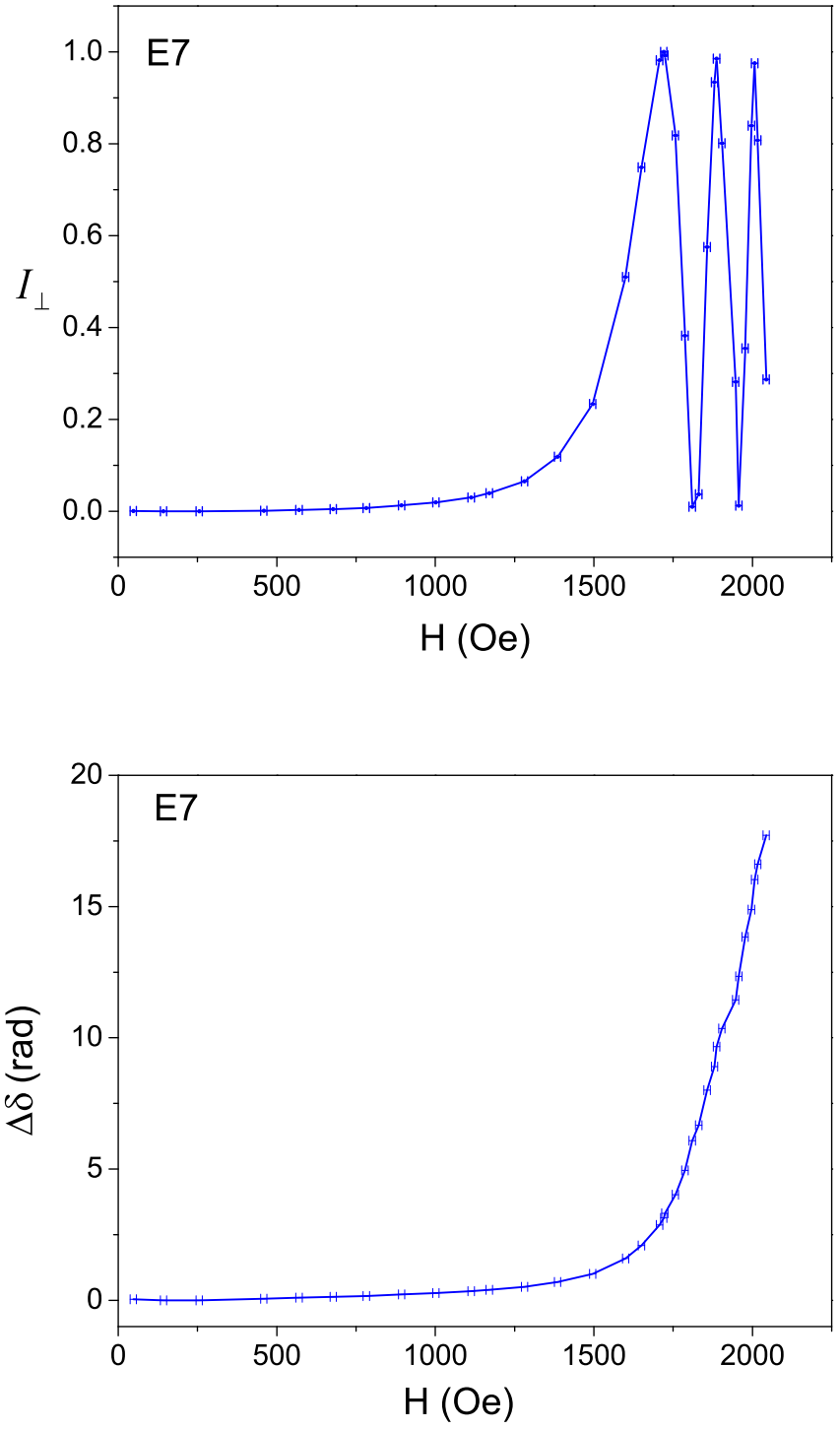

FIGURE 3.9: Experimental dependence of normalized cross-polarized intensity (top plot) and correspondent phase lag changes (bottom plot) on the test magnetic field for nematic E7 cell.

3.4 Electro-optic measurements

Electro-optic measurements involve two independent experiments: capacitance measurements and Frederiks transition experiments with an AC electric field. Firstly, the capacitance experiment is used to determine the dielectric constants, and secondly, the Frederiks transition experiment is used to find the bend and splay elastic constants of the liquid crystals or the liquid-crystal-based suspensions as described in this section. The results of these measurements performed on cells with different ferronematic suspensions will be presented later in Chapter 5. They are carried out in order to determine any possible variation of the dielectric constants or the elastic constants in ferronematic suspensions compared to undoped nematics. This information was essential for a complete characteristic of the magneto-optic experimental data and obtaining their good fit with the numerical model. This will be discussed fully in Chapters 5 and 6.

3.4.1 Capacitance measurements

A guard electrode liquid crystal cell is used in this experiment. As described above, this cell consists of a liquid crystal layer sandwiched between two transparent electrode layers of ITO. To a reasonable approximation, this cell can be considered as a capacitor with area $S_0 = 1 \times 1$ cm^2 and thickness $D = 12$ μm. The capacitance of the cell, according to the formula,

$$C = \frac{\varepsilon S_0}{4\pi D}, \tag{3.8}$$

depends on the effective dielectric constant of the liquid crystal layer, ε. In an empty cell ($\varepsilon = 1$), the capacitance, C_0, depends only on the cell parameters S_0 and D. The ratio between the capacitance of the cell that contains the liquid crystal, C, and the capacitance of the empty cell, before filling, C_0, yields an effective dielectric constant of the liquid crystal layer. The value of ε obtained in this way depends on the liquid crystal alignment inside the cell: $\varepsilon = \varepsilon_\perp$ in a planar cell and $\varepsilon = \varepsilon_\parallel$ in a homeotropic cell.

The cell capacitance at 1 kHz is measured using a Wayne Kerr automatic precision bridge B905, which contains a capacitance bridge circuit shown in Figure 3.10. It applies a small, approximately 1 mV, AC field at 1 kHz frequency to the circuit and changes the value of the variable capacitor until a null is reached. At this

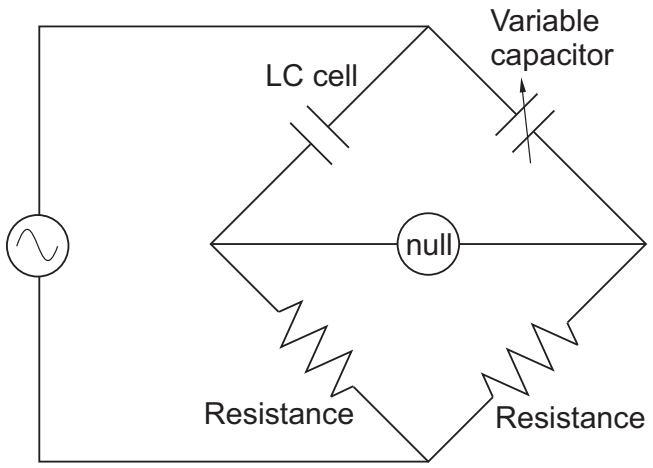

FIGURE 3.10: A standard bridge circuit used to measure the capacitance of a liquid crystal (LC) cell.

point, the values of the variable capacitor and the capacitance of the liquid crystal cell are equal. The small amplitude of the AC field ensures no significant effect on the liquid crystal alignment. The set up also applies a DC bias electric field to the cell electrodes, which can induce liquid crystal reorientation. The DC voltage is generated by a TTI QL564P power generator with an accuracy of $0.03\% \pm 5$ mV. In the experiment, the capacitance is recorded for various DC voltages applied to the cell. The capacitance is then calibrated by comparison with the previously measured capacitance of the empty cell. As mentioned above, this allows the determination of the effective dielectric permittivity of the liquid crystal layer. An example of the dependence of ε on the applied DC voltages for a cell filled with undoped E7 suspension is presented in Figure 3.11. The bridge measures capacitance with an accuracy of 0.05%. Thus, the dielectric permittivity is defined with the relative error of 0.1%.

Without any voltage applied to the cell, the liquid crystal has planar alignment. So, the value of dielectric permittivity at $V = 0$ corresponds to $\varepsilon_\perp$. As the voltage reaches the threshold value, the liquid crystal starts to reorient, changing the effective dielectric permittivity of the cell. When a sufficient voltage is applied to the cell, there is a complete reorientation of liquid crystal molecules within the electric field. The dielectric permittivity in this case saturates, and its value corresponds to $\varepsilon_\parallel$. From the data presented in Figure 3.11 it is possible to determine that $\varepsilon_\perp = 4.900 \pm 0.005$, $\varepsilon_\parallel = 17.30 \pm 0.02$. The value of $\varepsilon_\perp$ is very close to the data sheet (see Table 3.1); the value of $\varepsilon_\parallel$, however, is slightly smaller. This might be explained by a strong anchoring of the nematic molecules on the substrates. In

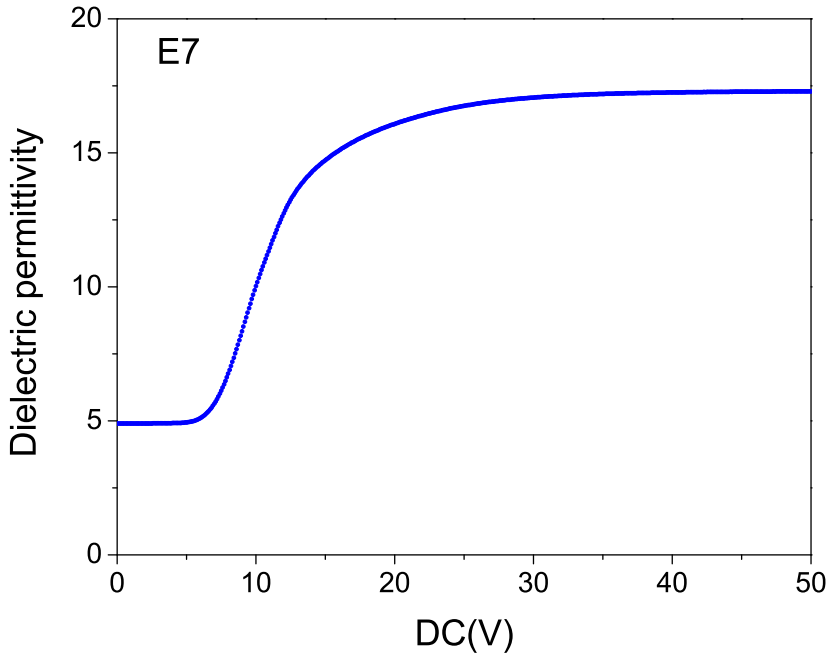

FIGURE 3.11: Dependence of the effective dielectric permittivity on the DC voltage obtained from the capacitance measurements for E7 cell. The relative errors for the dielectric permittivity is 0.1% and for the DC voltage is 0.03%.

this case, even at a high field there are thin layers of liquid crystal near the boundaries that have a planar orientation, which causes the resulting effective dielectric permittivity to be lower than $\varepsilon_{\parallel}$. Using a homeotropic cell instead of a planar cell can yield a more precise value of $\varepsilon_{\parallel}$.

This capacitance measurements give us the liquid crystal dielectric constants only at one frequency. To provide more detailed characteristics of dielectric constants and their dependences on frequency, dielectric spectroscopy measurements should be performed [15, 16, 17]. However, this is not required for the investigations conducted in this thesis.

3.4.2 Frederiks transition experiments in AC electric fields

Frederiks transition experiments in AC electric fields are also performed using guard electrode cells. The optical scheme is similar to the magneto-optic experiment: the cell is placed between two crossed polarizers, oriented at 45° with respect to the liquid crystal alignment. The optical system is illuminated by a beam of wavelength 532 nm from a frequency doubled YAG diode pumped laser (Laser

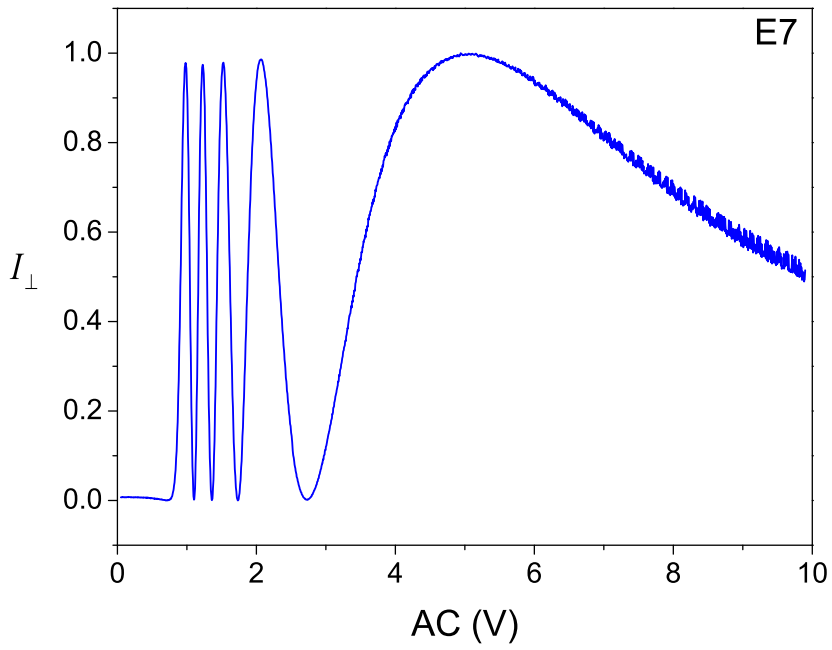

FIGURE 3.12: Dependence of the normalized cross-polarized intensity on the AC Voltage measured in the nematic E7 cell. The relative errors for the normalized intensity is 0.1% and for the AC voltage is 1%.

Quantum). The intensity of the beam after passing through the cell is monitored by a photodiode.

In the experiment, the cross-polarized intensity is recorded depending on the AC voltages applied to the cell. An AC electric field at 1 kHz and with 1% accuracy is generated by an Agilent 33120A waveform generator. Voltages are applied to the cell through conducting ITO layers and increased at a rate of 1 mV/s from 0 V to 10 V. An example of the normalized cross-polarized curve measured in the nematic E7 cell is shown in Figure 3.12.

The cross-polarized intensity curve $I_\perp(V)$ is qualitatively similar to the curve $I_\perp(H)$ obtained from the magneto-optic experiment (see Figures 3.12 and 3.9). The intensity at zero field in both curves depends on maximum of the phase lag induced by the planar alignment liquid crystal layer between ordinary and extraordinary beams: $\delta_{max} = 2\pi D n_a/\lambda$, where $n_a = n_e - n_o$ is the liquid crystal birefringence and D is the cell thickness . The intensity curves start to oscillate at the Frederiks threshold fields, at which the beginning of the liquid crystal reorientation happens. The Frederiks threshold in the magnetic field, H_c, depends on the cell thickness, D, and the liquid crystal parameters (diamagnetic anisotropy χ_a, and elastic constant K_1), while the threshold voltage in the electric field, V_c,

is determined by the liquid crystal properties only (dielectric anisotropy ε_a, and elastic constant K_1), as defined by Equation (2.28) and (2.34), respectively.

$$H_c = \frac{\pi}{D}\sqrt{\frac{K_i}{\chi_a}}, \tag{3.9a}$$

$$V_c = \pi\sqrt{\frac{4\pi K_i}{|\varepsilon_a|}}. \tag{3.9b}$$

Diamagnetic anisotropy of nematic E7 is very low, $\sim 10^{-7}$. Because of that, the transition in magnetic fields happens at a high field strength of $\sim 1,5$ kOe. Dielectric anisotropy, however, is much larger: $\varepsilon_a = \varepsilon_\parallel - \varepsilon_\perp = 12.4$, as can be seen from the capacitance measurements. Thus, transition takes place at relatively low voltages of ~ 0.6 Volt. That is why in the magneto-optic experiment we only measure the beginning of the liquid crystal reorientation (usually the first couple of oscillations in the cross-polarized intensity curve), while in the electric field the complete reorientation of the liquid crystal from the initial, planar alignment to homeotropic state is monitored. The complete reorientation requires a voltage of approximately 10 Volt. The complete reorientation of the liquid crystal appears as a slow reduction of the cross-polarized intensity to zero with increasing field. The residual intensity at high fields is associated with the anchoring effects at the cell boundaries.

The Frederiks transition experiment with an AC electric field allows estimations of the splay and bend elastic constants (K_1 and K_3). K_1 can be evaluated using the threshold voltage value, V_c. K_3 defines the rate of the liquid crystal reorientation towards the homeotropic state at a high field. The higher value of K_3 results in the slower process of reorientation, which appears in the larger spacing between the intensity oscillations in curve $I_\perp(V)$. The exact values of K_1 and K_3 can be found by fitting the experimental cross-polarized intensity curve using a numerical model described in [18].

Summary

This section describes experimental method that are used to characterise nematics and ferronematic suspensions in Chapter 4 and in Chapter 5, respectively. In the experiments, undoped liquid crystals or ferronematic suspensions are tested in planar liquid crystal cells. There are two types of cells: the standard cell of 50 μm thickness and the guard electrode cell of 12 μm thickness. The guard electrode cell has patterned conductive ITO layers on its substrates, which apply voltages to it. The standard cell is used in magneto-optic experiments, while the guard electrode cell is used in electro-optic experiments. In both cells rubbed polyimide layers are utilized to produce planar liquid crystal alignment with a small pretilt angle between 2.5 and 3°. The pretilt is measured by a crystal rotation method.

The properties of nematics or ferronematic suspensions are investigated using magneto-optic and electro-optic measurements. Magneto-optic experiments allow the determination of the sensitivity to magnetic field. It is based on observations of the magnetic-field-induced Frederiks transition in the cell by an optical method. Electro-optic measurements involve two experiments: a capacitance experiment and a Frederiks transition experiment in an AC electric field. Capacitance measurements is used to determine the liquid crystal dielectric permittivities $\varepsilon_\perp$ and $\varepsilon_\parallel$. Frederiks transition experiments in an AC field are used to evaluate any possible variation of the elastic constants K_1 and K_3 in ferronematic suspensions compared to undoped nematic.

References

[1] E. P. Rynes, C. V. Brown, and J. F. Stromer. Method for the measurement of the K_{22} nematic elastic constant. *Applied Physics Letters*, 82(1):13–15, 2003.

[2] L. M. Blinov and V. G. Chigrinov. *Electrooptic Effects in Liquid Crystal Materials*. Springer, New York, 1994.

[3] Y. Zhou and S. Sato. A method for determining elastic constants of nematic liquid crystals at high electric fields. *Japanese Journal of Applied Physics*, 36 (7A):4397–4400, 1997.

[4] J. Li, C.-H. Wen, S. Gauza, R. Lu, and S.-T. Wu. Refractive indices of liquid crystals for display application. *IEEE/OSA Journal of Display Technology*, 1 (1):51–61, 2005.

[5] I.-C. Khoo and S.-T. Wu. *Optics and Nonlinear Optics of Liquid Crystals*. World Scientific, Singapore, 1993.

[6] E. P. Rynes, R. J. A. Tough, and K. A. Davies. Voltage dependence of the capacitance of a twisted nematic liquid crystal layer. *Molecular Crystals and Liquid Crystals*, 56:63–68, 1979.

[7] P. Yen and C.Gu. *Optics of Liquid Crystal Displays*. Wiley, New York, 1999.

[8] P. G. de Gennes and J. Prost. *The Physics of Liquid Crystals*. Clarendon Press, Oxford, 2nd edition, 1993.

[9] P. J. Collings. *Liquid Crystals: Nature's Delicate Phase of Matter*. Princeton University Press, Princeton, New Jersey, 1990.

[10] I. Dierking. *Textures of Liquid Crystals*. Wiley-VCH, Weinheim, 2003.

[11] T. J. Scheffer and J. Nehring. Accurate determination of liquid-crystal tilt bias angles. *Journal of Applied Physics*, 48(5), 1977.

[12] F. Nakano, M. Isogai, and M. Sato. Simple method of determining liquid crystal tilt-bias angle. *Japanese Journal of Applied Physics*, 19(10), 1980.

[13] B. L. Van Horn and H. Henning Winter. Analysis of the conoscopic measurements for uniaxial liquid-crystal tilt angles. *Applied Optics*, 40(13), 2001.

[14] L. M. Blinov. *Electro-optical and Magneto-optical Properties of Liquid Crystals*. Wiley, Chichester, 1983.

[15] G. P. Sinha and F. M. Aliev. Dielectric spectroscopy of liquid crystals in smectic, nematic, and isotropic phases confined in random porous media. *Physical Review E*, 58(2):2001–2010, 1998.

[16] S. K. Kundu, S. Okudaira, M. Kosuge, N. Shinyashiki, and S. Yagihara. Broadband dielectric spectroscopy of a nematic liquid crystal in benzene. *Journal of Chemical Physics*, 129:164509, 2008.

[17] P. Perkowski. Dielectric spectroscopy of liquid crystals. Electrodes resistivity and connecting wires inductance influence on dielectric measurements. *Opto-Electronics Review*, 20(1):79–86, 2012.

[18] K. R. Daly. *Light-matter Interaction in Liquid Crystal Cells*. PhD thesis, University of Southampton, 2011.

Chapter 4

Magnetic-field-induced Frederiks transition in nematic cells

In this chapter a numerical model of magnetic-field-induced Frederiks transition in nematic cells is derived. The model is based on the continuum theory. The geometry of a nematic cell corresponds to the experimental set up described in the previous chapter. The model takes into account both a small pretilt of the nematic director at the cell boundaries and an in-plane bias magnetic field. Although the Frederiks transition problem was studied in great detail in both geometries: classical [1, 2] (when a magnetic field is perpendicular to the initial director alignment) and tilted [3, 4] (when a director is inclined with respect to the magnetic field), it can be shown that some new features occur in the presence of a pretilt and also a bias magnetic field. In particular, the application of a bias field shifts the effective threshold and this shift is sensitive to the direction of the bias field with respect to the easy axis. The shift in the effective threshold is significantly larger than the value of the bias field causing it. This effect is also confirmed by experimental results, which agree well with the proposed model.

The structure of this chapter is as follows. In Section 4.1 a numerical model that describes the response of the nematic director to the magnetic field is derived and used to test the fit with magneto-optic experimental data. In Section 4.2 the effect of both easy axis pretilt and bias field on the system response is described using numerical model predictions and experimental data. To analyse these effects, some analytical calculations are made using the small angle assumption as described in Section 4.3. This allows a derivation of an approximate dependence of the director deviation angle on the field.

4.1 Numerical model of a nematic cell in a magnetic field

The numerical model of a nematic liquid crystal cell in a magnetic field is based on the continuum theory, which was introduced in Section 2.2.1. An orientation order of the liquid crystal molecules inside the cell is described by the nematic director field $\boldsymbol{n}$. The total free energy of the system in the presence of the external magnetic field $\boldsymbol{H}$ can be expressed by Equation (2.27):

$$\mathcal{F}_N = \int_V \frac{1}{2}\left[K_1(\boldsymbol{\nabla}\cdot\boldsymbol{n})^2 + K_2(\boldsymbol{n}\cdot\boldsymbol{\nabla}\times\boldsymbol{n})^2 + K_3(\boldsymbol{n}\times\boldsymbol{\nabla}\times\boldsymbol{n})^2\right] - \frac{1}{2}\chi_a(\boldsymbol{n}\cdot\boldsymbol{H})^2\, dV, \tag{4.1}$$

where $K_1,\ K_2,\ K_3$ are the elastic constants and χ_a is the diamagnetic anisotropy of the nematic. It is worth remembering that the first term is the elastic energy of liquid crystal deformations and the second term is the magnetic energy of the nematic molecules.

A nematic cell of thickness D is considered in the model, see Figure 4.1. The geometry of the cell corresponds to the experimental geometry described in Section 3.3. Nematic alignment is assumed to be planar with a small pretilt angle α of easy axis on the boundary surfaces and with an infinitely strong anchoring energy. An external magnetic field is applied to the cell in two different directions: the test field $\boldsymbol{H}$ is in the z direction, perpendicular to the substrates; the small bias field $\boldsymbol{H}_b$ is in the cell plane, along the x axis. The magnetic field can be expressed as:

$$\boldsymbol{H} = (H_b,\ 0,\ H). \tag{4.2}$$

The cell is assumed to be uniform in the x and y directions, so the director field depends on the z coordinate only. Moreover, it is assumed that there is no twist deformation in the cell, so the director always stays in the $x-z$ plane. Thus, it can be described by an angle $\theta(z)$ that it forms with the cell facets as

$$\boldsymbol{n} = (\cos\theta,\ 0,\ \sin\theta). \tag{4.3}$$

The free energy functional (4.1) in the described geometry takes the following form:

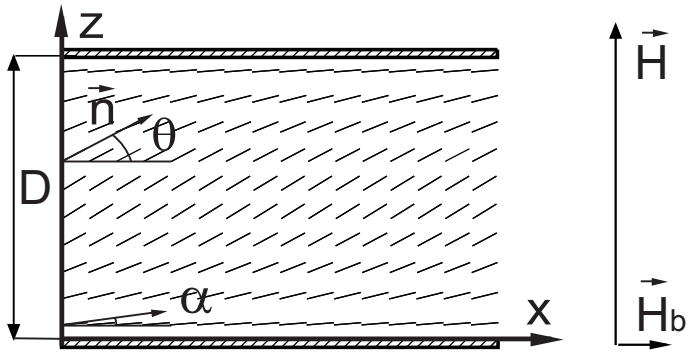

FIGURE 4.1: Geometry of the nematic cell.

$$\mathcal{F}_N = \int_0^D \frac{K_1}{2}\left(\frac{d\theta}{dZ}\right)^2 [1 + p\sin^2\theta] - \frac{\chi_a}{2}\left[H\sin\theta + H_b\cos\theta\right]^2 dZ, \tag{4.4}$$

where $p = (K_3 - K_1)/K_1$.

The following dimensionless parameters can be introduced in the model. Dimensionless coordinate z is scaled with respect to the cell thickness: $z = Z/D$, with $0 < z < 1$. The test, H, and the bias, H_b, magnetic fields are represented by non-dimensional parameters h and h_b, respectively, which are equal to

$$\begin{aligned} h &= \frac{H}{H_s}, \quad b = \frac{H_b}{H_s}, \\ H_s &= \frac{1}{D}\sqrt{\frac{K_1}{\chi_a}}. \end{aligned} \tag{4.5}$$

Then, the non-dimensional free energy functional reduces to

$$F_N = \int_0^1 \frac{1}{2}\left(\frac{d\theta}{dz}\right)^2 [1 + p\sin^2\theta] - \frac{1}{2}\left[h\sin\theta + b\cos\theta\right]^2 dz. \tag{4.6}$$

This functional depends on one variable function - $\theta(z)$. The equilibrium director orientation corresponds to a minimum of the free energy. The Euler-Lagrange equation that minimizes the free energy functional (4.6) with respect to the variable angle $\theta(z)$ can be written as:

$$\frac{d^2\theta}{dz^2}[1 + p\sin^2\theta] + \frac{p}{2}\left(\frac{d\theta}{dz}\right)^2 \sin 2\theta + \frac{h^2 - b^2}{2}\sin 2\theta + hb\cos 2\theta = 0. \tag{4.7}$$

The differential equation (4.7) can be solved analytically only if the director distortion angle θ is assumed to be small. This analytical approximation to the solution will be derived later in Section 4.3. However, Equation (4.7) can be solved numerically as a boundary value problem. The numerical function of the director orientation angle is calculated for a number of points z_i on the Chebyshev grid. The director anchoring at the cell boundaries is taken into account as the Dirichlet boundary conditions: $\theta\ (z = 0,\ z = 1) = \alpha$. The Euler-Lagrange equation is solved using a Broyden non-linear solver [5]. The differentials over the spatial coordinate z are evaluated using the Chebyshev differential matrix [6]. Description of these numerical methods can be found in Appendix A. The program code for solving Equation (4.7) is implemented in MATLAB. It yields a numerical function $\theta(z)$ for given strengths of the test and the bias magnetic fields, cell pretilt angle and liquid crystal parameters.

4.1.1 Fitting the magneto-optic experiment results

The numerical model consists of two stages. In the first stage, the program evaluates a profile of the director orientation inside the cell as described above. The second part of the program calculates the optical properties of the liquid crystal cell with a given director profile and, in this way, simulates the magneto-optic experiment described in Section 3.3.

In the experiment, a laser beam propagates through the cell in the z direction. The incident light is linearly polarized with the polarization plane at 45° with respect to the $x - z$ plane (see cell geometry in Figure 4.1). As discussed in Section 2.2.3, the out-of-plane component of the light experiences the ordinary refractive index, n_o, while the in-plane component encounters some effective refractive index, n_{eff}, the equation of which can be obtained by substituting $\theta_i = \pi/2 - \theta$ into Equation (2.35):

$$n_{eff}(\theta) = n_e[1 + \nu \sin^2 \theta(z)]^{-1/2}, \tag{4.8}$$

where $\nu = (n_e^2 - n_o^2)/n_o^2$, n_e is the extraordinary refractive index. As the light passes through the liquid crystal layer, the in-plane component phase shifts with respect to the out-of-plane component. The phase lag, δ, between the two components of light is determined by the nematic director orientation angle $\theta(z)$. δ can be computed using Equation (2.37), which in this case can be rewritten as:

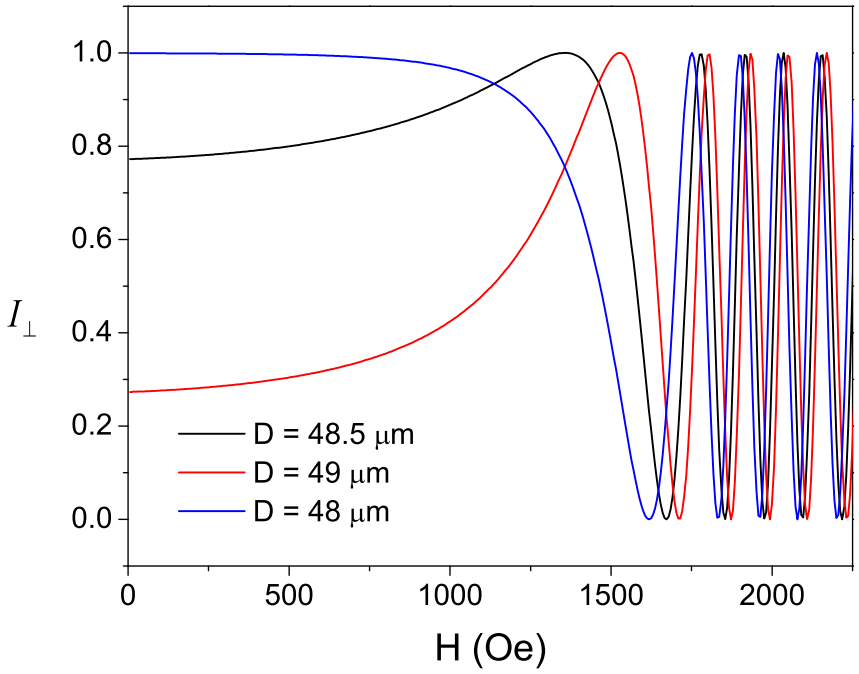

FIGURE 4.2: Calculated dependence of cross-polarized intensity for E7 cells with different thicknesses D.

$$\delta = \frac{2\pi D}{\lambda} \int_0^1 n_o - n_e[1 + \nu \sin^2 \theta(z)]^{-1/2} dz. \tag{4.9}$$

Using the numerically calculated nematic director function $\theta(z)$, the second part of the numerical model evaluates the phase lag integral using a Clenshaw-Curtis quadrature scheme, the details of which are presented in Appendix A [6]. By carrying out these calculations for a range of test magnetic fields, the numerical function $\delta(H)$ can be found. After that, a normalized cross-polarized intensity dependence is calculated using Equation (2.42).

The calculated dependence of normalized cross-polarized intensity, $I_{\perp th}(H)$, can now be fitted to the measured one, $I_{\perp exp}(H)$. The fitting procedure begins with a determination of the cell thickness by fitting a starting point of the experimental cross-polarized intensity curve (value of the cross-polarized intensity at zero magnetic field, $I_\perp(H = 0)$). The cell thickness is known approximately from direct measurement (see Section 3.2.1). For a cell filled with nematic E7, this value is measured to be $D = (49 \pm 0.5)$ μm. The starting point of the cross-polarized intensity curve is determined by the initial phase lag, that is, in the zero pretilt approximation, $\delta_{max} = 2\pi D(n_o - n_e)/\lambda$. Owing to the relatively large birefringence of E7 ($n_a = n_e - n_o = 0.22$), a cell thickness uncertainty of 1 μm results

in a phase lag uncertainty of approximately 0.7π. This uncertainty can shift the zero-field intensity by more than a half of its amplitude, as demonstrated in Figure 4.2. Thus, by the fitting of $I_\perp(H = 0)$, the cell thickness can be calculated more precisely, to within 0.1 μm. It is found to be 49.2 μm for the E7 cell, which is equal to the measured value within the range of experimental error.

The next part of the fitting procedure consists of finding appropriate fitting parameters that minimize the mean square deviation between the calculated and experimental values of cross-polarized intensity, over the whole range of the magnetic field. Any system parameters (e.g. elastic constants, diamagnetic anisotropy, or pretilt angle) can be set as the fitting parameters. They will be specified for each particular set of experimental data.

The quality of fit can be characterised by different methods [7]. One way is to calculate a sum of squared errors: $\sum(I_{\perp exp} - I_{\perp th})^2$. In the case where the uncertainty in the individual measurement, σ_i, is known, it is possible to use a weighted sum of squared errors: $\sum \frac{1}{\sigma_i^2}(I_{\perp exp} - I_{\perp th})^2$, known as chi-squared goodness of fit [8]. However, these sums strongly depend on the number of experimental data points N, which makes them inconvenient for comparison when the number of data point varies between different experiments. In this case a normalization to fit measure is required. It is possible to calculate the reduced chi-squared statistic: $\frac{1}{N-n-1}\sum \frac{1}{\sigma_i^2}(I_{\perp exp} - I_{\perp th})^2$, where n is the number of fitted parameters. Another method is normalizing errors with respect to the theoretically expected value: $\sum \frac{1}{I_{\perp th}}(I_{\perp exp} - I_{\perp th})^2$. In our case however, $I_{\perp th}$ often reaches zero, which would lead to unreasonably large values. So, in the procedure presented in the thesis, the measure for goodness of fit is characterized by a sum of deviations, r, normalized in the following way:

$$r = \frac{\sum(I_{\perp exp} - I_{\perp th})^2}{\sum I_{\perp exp} \cdot I_{\perp th}}. \tag{4.10}$$

The fitting procedure is verified by analyzing the magneto-optic experimental data collected from the E7 cell, which were presented in Figure 3.9 (see Section 3.3). Figure 4.3 shows the comparison between the theoretical and experimental cross polarized intensities and the corresponding phase lag curves. The only fitting parameter in this case is the diamagnetic anisotropy χ_a. The elastic constants $K_{1,3}$ and the refractive indices $n_{e,o}$ of E7 are taken from the literature (see Table 3.1), the pretilt angle α and the bias field H_b are measured directly: $\alpha = 2.7°$, $H_b = 16$ Oe. The best fit is obtained for a value of $\chi_a = 1.22 \times 10^{-7}$, the order of magnitude of which is consistent with those found in the literature ($\chi_a \sim 10^{-7}$ [1]). The

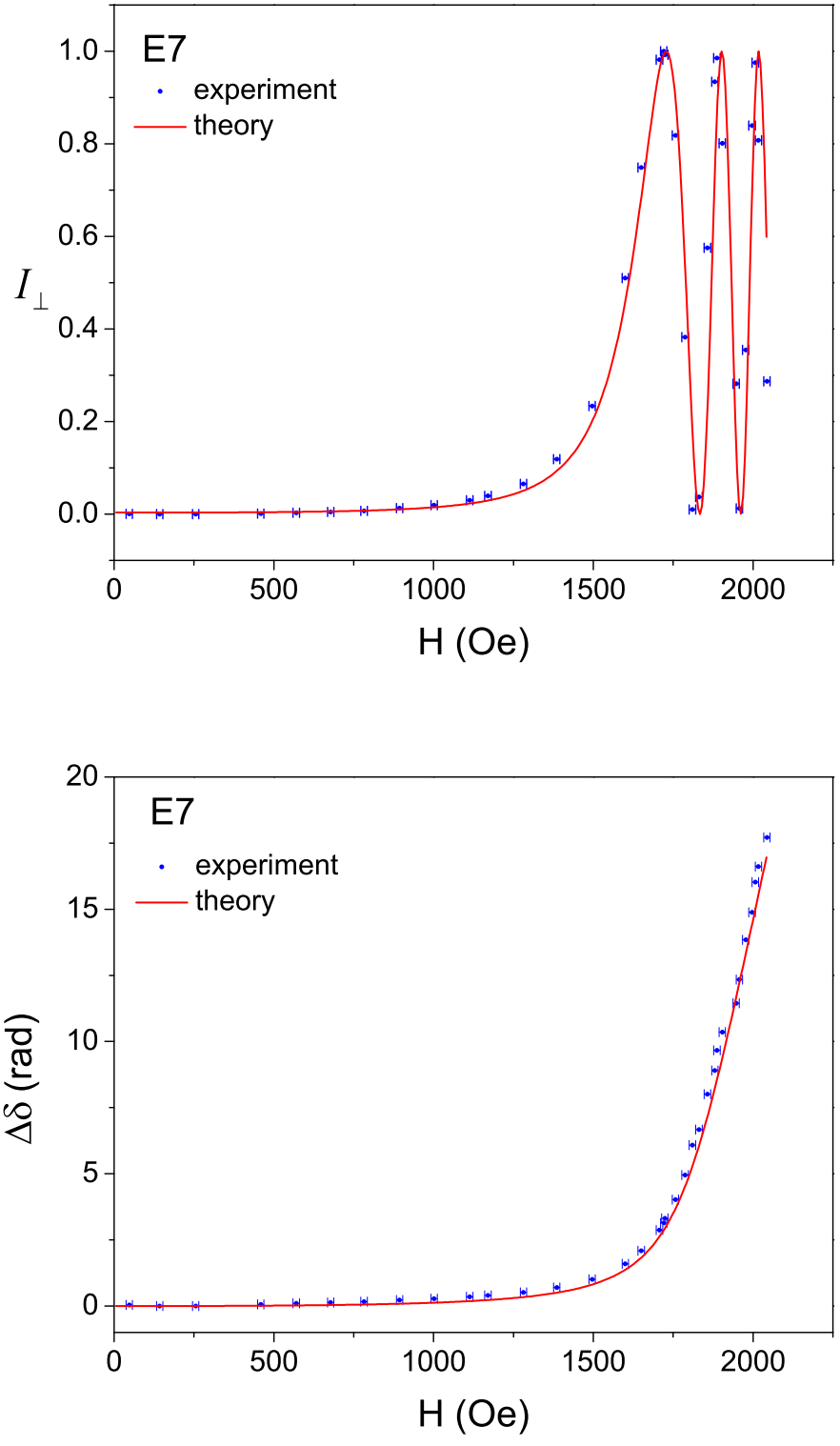

FIGURE 4.3: Comparison between the experimental data (blue dots with error bars) and the results of modelling (red line) of normalized cross-polarized intensity (top plot) and correspondent phase lag (bottom plot) for E7 cell.

accuracy of the fit is $r = 0.014$. This fit shows clearly that the model is well able to describe the optical response of a nematic cell to the external magnetic field.

The model can be used not only for fitting experimental data, but also for exploring and predicting the results for different experimental conditions, e.g. varying the bias field or cell pretilt, sometimes even beyond the experimental set up limit.

4.2 Symmetry-breaking effect of bias magnetic field and surface pretilt

In this section, the effect of a bias magnetic field and a surface pretilt on the magnetic-field-induced Frederiks transition in a nematic cell is discussed. The Frederiks transition is more easy to detect from a plot of the phase lag dependence on the magnetic field (the lower plot in Figure 4.3) rather than from the cross-polarized intensity curve (the upper plot).

To understand the effect of both the pretilt and the bias field, let us start with a consideration of the classical Frederiks transition, which occurs in a cell with no bias field and no pretilt. The model can simulate the classical Frederiks geometry by substituting $\alpha = b = 0$. Orientation of the nematic director inside the cell calculated with different values of the magnetic field is presented in Figure 4.4. The director orientation angle is a symmetric function with respect to the centre of the cell because of symmetric anchoring conditions at the cell boundaries. Thus, the director reorientation with field can be represented by the director angel in the centre of the cell, $\theta(z = 1/2)$, which is plotted in Figure 4.5. This figure clearly demonstrates classical Frederiks transition. The nematic director stays unperturbed for magnetic fields below the threshold value. A sharp transition happens at the threshold field, which appears as a rapid reorientation of the director. The corresponding graph of the phase lag also demonstrates a sharp transition, which is shown by the black curves in Figure 4.6. In dimensionless units, the threshold field corresponds to $h_c = \pi$. Above the threshold, the director reorientation angle increases with the field and saturates, reaching the value of $\pi/2$, which corresponds to the complete alignment in the direction of the magnetic field. It can be seen in Figure 4.4 that for a high enough magnetic field, far above the threshold value, the director is homeotropically aligned in the whole cell volume except some thin layers close to the boundaries.

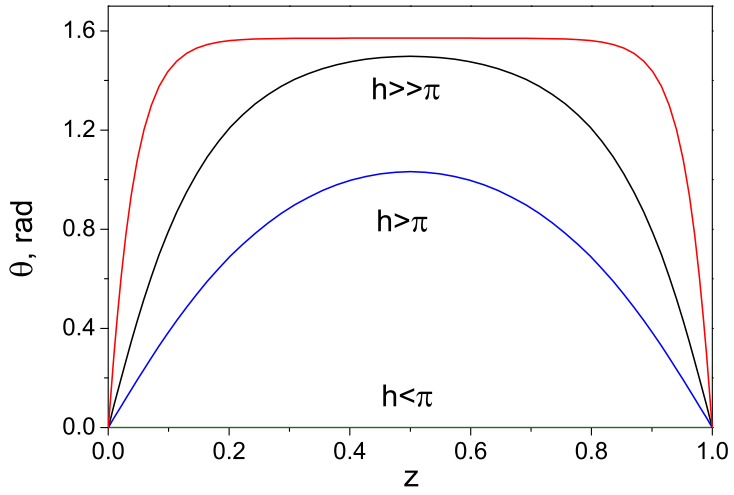

FIGURE 4.4: Orientation of nematic director inside the cell for different values of the magnetic field.

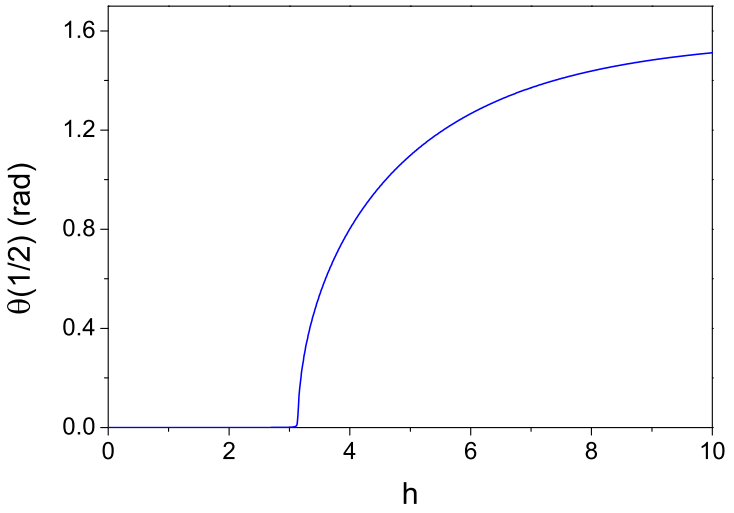

FIGURE 4.5: Dependence of the nematic director deviation the centre of the cell on the dimensionless magnetic field.

In the classical Frederiks geometry, there is a reflection symmetry of the system below the threshold. It breaks spontaneously at the threshold, and both clockwise and counterclockwise director rotations become possible. From the mathematical point of view, it means that if $\theta = \theta(z)$ is a solution of the Euler-Lagrange equation (4.7), then $\theta = -\theta(z)$ satisfies this equation as well. Both solutions $\theta(z)$ and $-\theta(z)$ result in the same phase lag at the same test field, as the phase lag depends on $\sin^2\theta$ (see Equation (4.9)). So, both ways of director rotation are indistinguishable in the optical experiment. In a real experimental cell, however, spatial

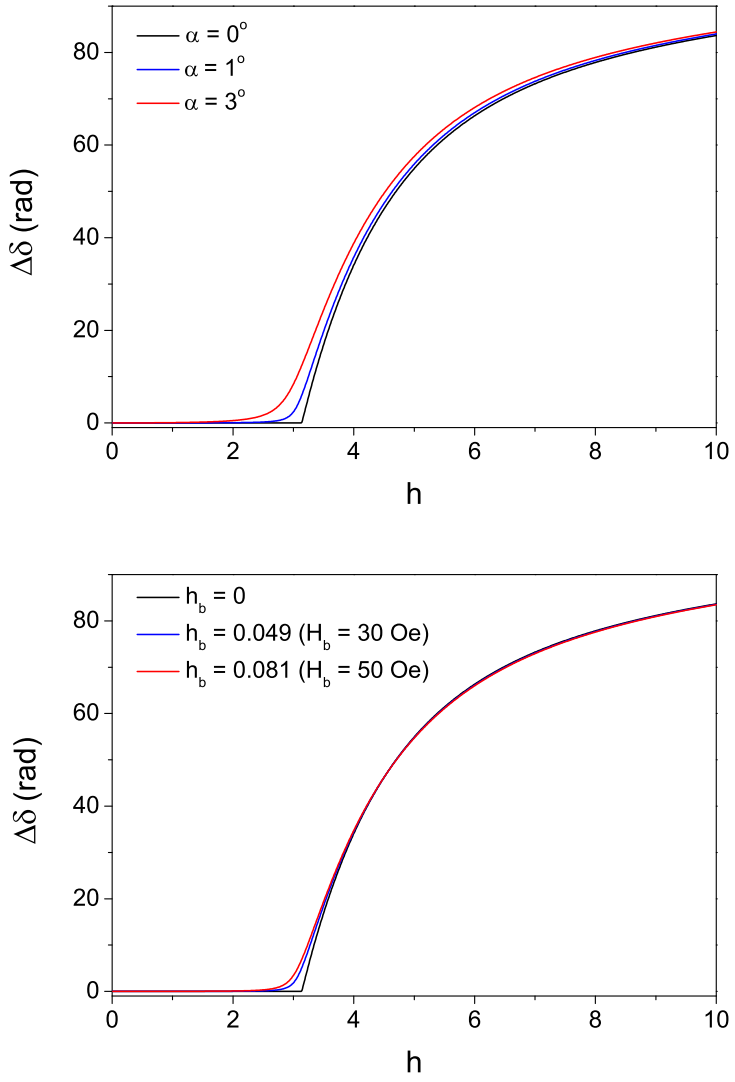

FIGURE 4.6: Effect of the pretilt (top plot) and the bias field (bottom plot) on the phase lag change.

inhomogeneities connected with the symmetry-breaking, may cause domains with different directions of director rotation and also cause defects at these domain boundaries.

Introducing a pretilt or a bias field breaks the symmetry from the initial state. This favours the director switching in one direction only. Frederiks transition in this case is demonstrated in Figure 4.6 by the phase lag curves calculated for different values of the pretilt angle at zero bias field (the upper plot) and for different bias fields at zero pretilt (the lower plot). The pretilt or the bias field effectively destroy the threshold behaviour, as the total magnetic field is not perpendicular to the initial director alignment anymore. This causes a small director distortion at fields below the threshold and makes the Frederiks transition to be "smeared" compared

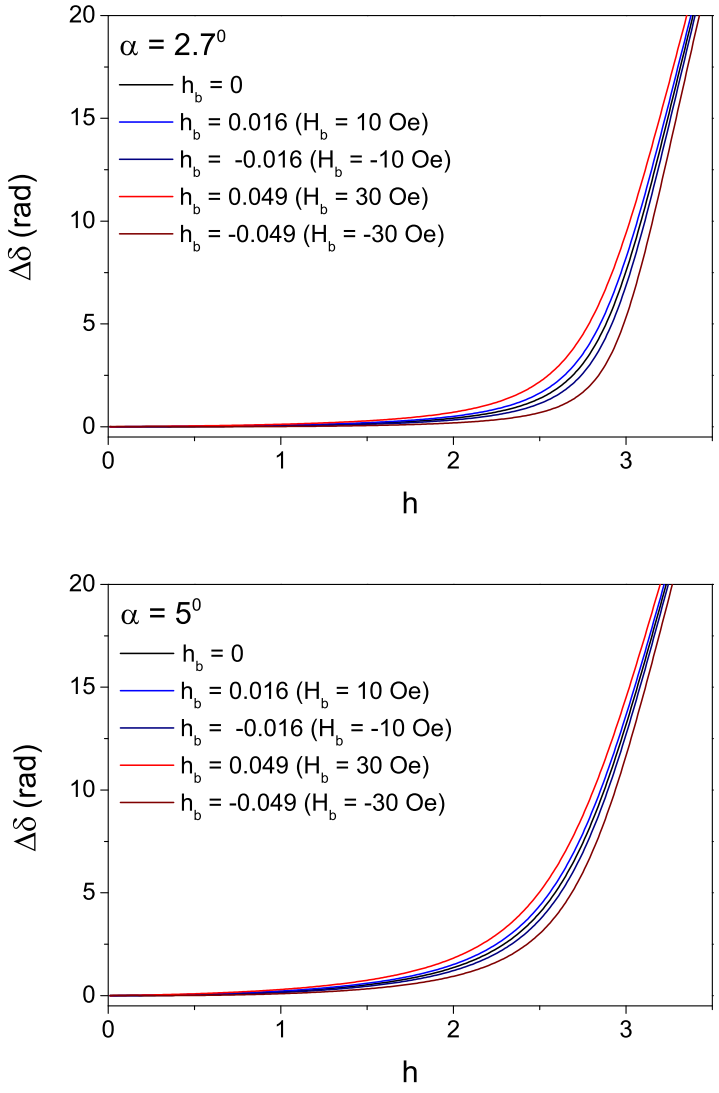

FIGURE 4.7: Effect of the direction and magnitude of the bias field on the phase lag change for two values of pretilt angle: 2.7^o and 5^o.

to the classical case. The smearing increases with increasing pretilt angle or bias field magnitude. Therefore, in such cases it is possible to refer to an "effective" threshold field only. The pretilt or the bias field imposes the largest change in the phase lag at test magnetic field values close to the threshold value. There is not much difference between the curves in Figure 4.6 for a higher field range.

Changing the direction of bias field can cause another symmetry-breaking effect. In the absence of a pretilt (when $\alpha = 0, b \neq 0$), different directions of the bias field will induce different ways of director switching. However, both directions of the bias field produce optically identical results. In the same way, different orientations of the easy axis with respect to the z axis are optically indistinguishable when there is no bias field ($\alpha \neq 0, b = 0$). However, this no longer holds in the presence of

both a pretilt and a bias field ($\alpha \neq 0, b \neq 0$). In this case, the symmetry, broken by the pretilt, is further reduced by applying a bias field in one or another direction. So, different directions of the bias field for a fixed easy axis becomes optically different, resulting in a shift of the phase lag curve, as demonstrated in Figure 4.7. In this figure, the bias field is labelled as positive (forward direction) if it points in the direction of easy axis orientation, as indicated in Figure 4.1. The opposite direction (backward direction) is labelled as negative.

It can be seen that the shift between the two phase lag curves in Figure 4.7, that correspond to different bias field directions, depends on the pretilt as well as on the modulus of the bias field. Comparison between the upper and the lower plots shows that the phase lag curve becomes smoother with increasing pretilt angle, but a bias field of the same strength causes a smaller shift between the two curves. The quantitative characteristics of the effects of bias field and pretilt angle on the phase lag shift will be given in the next section. In the rest of this section, these effects are studied experimentally.

For experimental confirmation of the model prediction, the Frederiks transition measurements (see Section 3.3) were carried out for cells filled with two different liquid crystals: E7 and 5CB. For each cell, the dependences of the phase lag change, $\Delta\delta$, on the magnetic field, H, were measured several times with different amplitudes and directions of the bias magnetic field. The bias field direction was varied by changing the voltage polarity on the Helmholtz coils, without changing the cell position in the set up. By doing so, the same spot on the cell was tested during each experimental run. This eliminated any effect of thickness variation across the cell. Typical experimental curves are plotted as dotted lines in Figure 4.8 and 4.9. These curves show the same trend as discussed in Section 4.1.1. These data also confirm the predicted shift between phase lag curves on changing the bias field direction.

The experimental data were fitted to the numerical model using the procedure described in Section 4.1.1. The corresponding theoretical curves for each set of experimental data are plotted in Figure 4.8 by the solid lines on the top of the experimental points. It should be mentioned that both theoretical curves in each graph were obtained with the same system parameters, except the bias field parameters b, which differed by sign only. The fitting parameter in all cases was the diamagnetic anisotropy χ_a. Its value for the nematic E7 cell is $\chi_a = 1.22 \times 10^{-7}$, which is consistent with the previous fit. For the nematic 5CB cell, the fitting value is $\chi_a = 1 \times 10^{-7}$, the order of magnitude of which is consistent with the value found

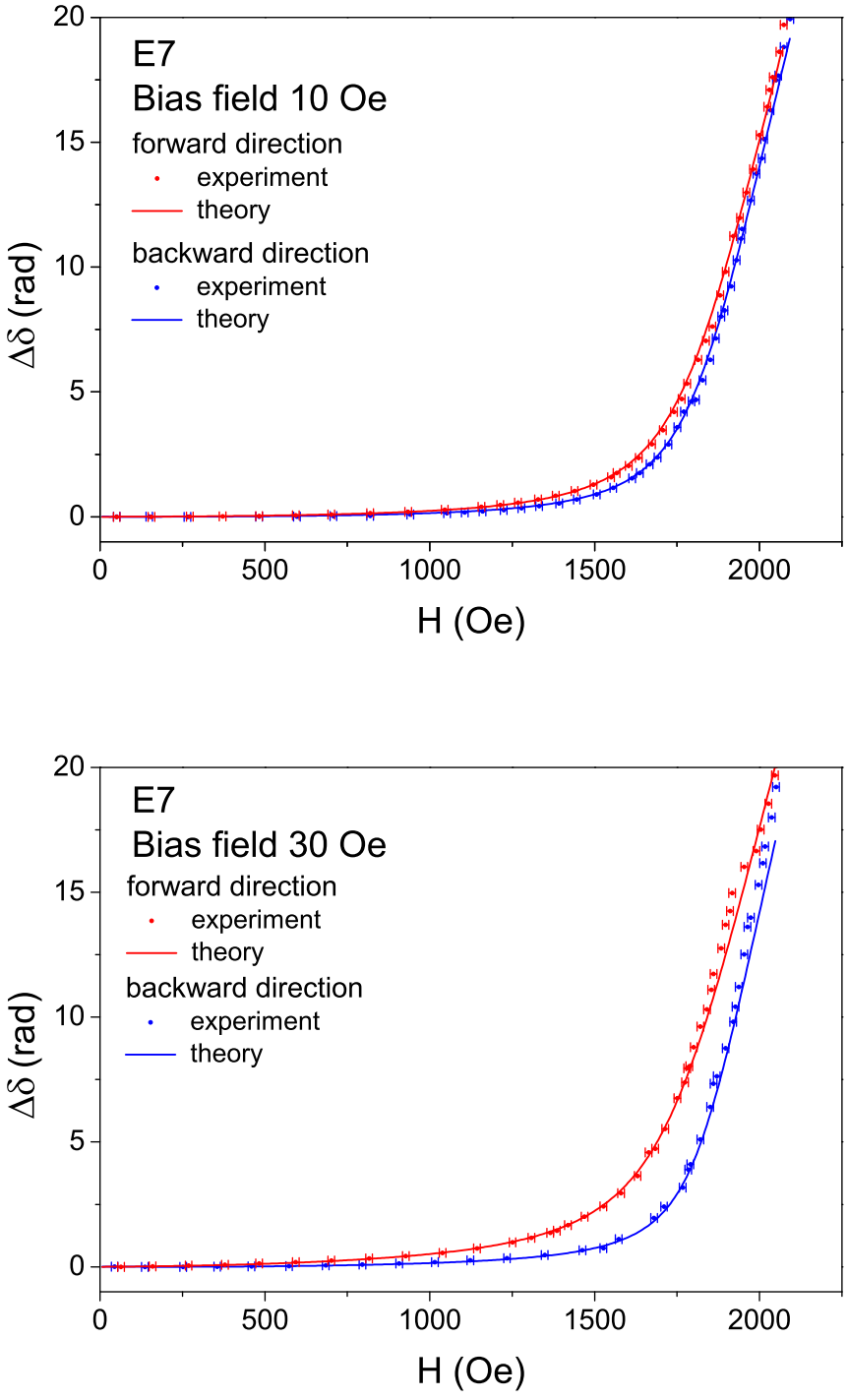

FIGURE 4.8: Shift of the phase lag curve depending on the direction of the bias magnetic field in a cell with nematic liquid crystals E7 and different amplitudes of the bias field (see legend). Dots are experimental data with error bars; lines are fitting curves.

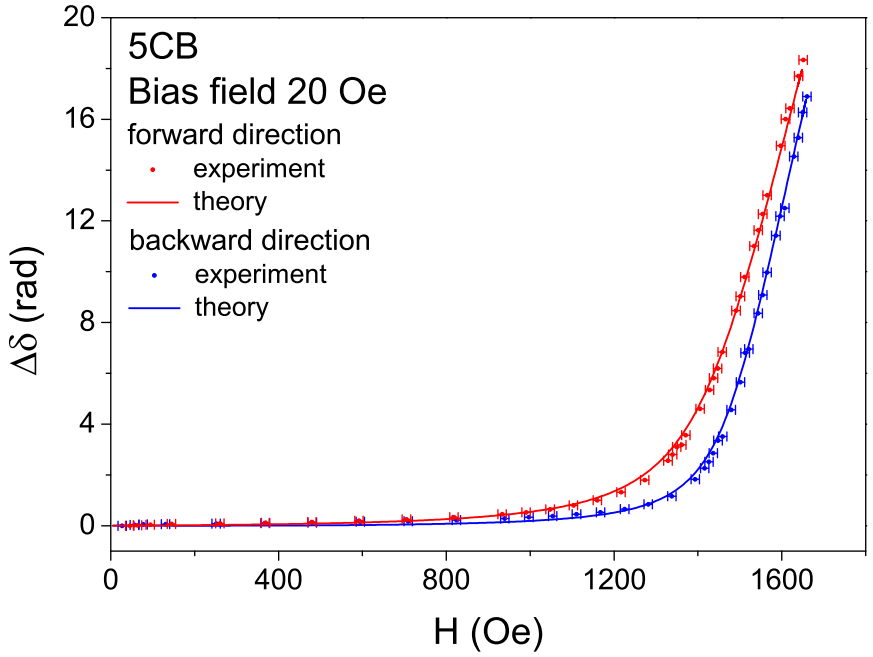

FIGURE 4.9: Shift of the phase lag curve depending on the direction of the bias magnetic field in a cell with nematic liquid crystals 5CB (see legend). Dots are experimental data with error bars; lines are fitting curves.

in the literature (see Table 3.1 and [1]). The agreement between the fitting curves and the experimental data confirms the validity of the nematic model.

The curves in Figure 4.8 and 4.9, in some sense, resemble curves with the shifted "effective" Frederiks threshold. As predicted within the model, a large magnitude of bias field causes a larger shift in the apparent threshold. Moreover, the shift in the test field threshold is significantly larger than the magnitude of the bias field causing it. For example, in the second plot in Figure 4.8 (for $H_b = 30$ Oe), the difference in test fields H that corresponds to $\Delta\delta = 2.5$ between the blue and red curves is approximately 200 Oe, an effective amplification of a factor of about 7.

It can be seen that the largest shift is observed when test magnetic fields are close to the Frederiks threshold. At this strength of the test magnetic field, the liquid crystal just starts to reorient, so the director deviation angle is small. Thus, in this region the system can be described analytically using the small angle approximation method [9].

4.3 Analytical description of magneto-optic response in nematic cell

The small angle approximation method is commonly used to describe the nematic director deviation just above the Frederiks threshold [9]. In this method, a function of the director orientation angle is expressed by the first term of the harmonic expansion, $\theta(z) = \theta_0 \sin \pi z$, where the amplitude of the director angle, θ_0, is assumed as a small ($\theta_0 \ll 1$) [10]. This approximation satisfies the boundary conditions: $\theta(z = 0,\ z = 1) = 0$.

In the geometry of the model considered here, there is a surface pretilt, which makes the boundary conditions as $\theta(z = 0,\ z = 1) = \alpha$. Such boundary conditions can be satisfied by assuming the director angle function as $\theta(z) = \alpha + \theta_0 \sin \pi z$. The pretilt and the bias field are assumed to be small ($\alpha, b \ll 1$), so the first order expansion of the free energy (4.6) in powers of α and b yields:

$$F_N = \int_0^1 \frac{1}{2} \left(\frac{d\tilde{\theta}}{dz} \right)^2 - \frac{h^2}{2} \sin^2 \tilde{\theta} - \frac{h}{2}(\alpha h + b) \sin 2\tilde{\theta}\ dz + o(\alpha^2, b^2), \tag{4.11}$$

where $\tilde{\theta} = \theta_0 \sin \pi z$. One elastic constant approximation, $p = 0$, is also assumed in this expansion.

Firstly, let us consider the classical Frederiks geometry ($\alpha = b = 0$). The trigonometric functions in the free energy functional (4.11) can be expanded in a Taylor series for small values of θ_0. By performing integration over the z coordinate, the following expansion is obtained:

$$F_N \simeq \frac{\pi^2 - h^2}{4} \theta_0^2 + \frac{h^2}{16} \theta_0^4 + o(\theta_0^5). \tag{4.12}$$

Solving the Euler-Lagrange equation, $\partial F_N / \partial \theta_0 = 0$, yields the following amplitude of director deviation:

$$\theta_0(h) = \begin{array}{ll} 0 & \text{if } h \leqslant \pi \\ \sqrt{2\left(1 - \frac{\pi^2}{h^2}\right)} & \text{if } h > \pi. \end{array} \tag{4.13}$$

Solution (4.13) clearly indicates the threshold behaviour of the nematic director deviation in the magnetic field. The nematic director can be distorted only by

fields stronger than the Frederiks threshold value. The critical dimensionless field is $h_c = \pi$. Taking into account Equation (4.5), h_c corresponds to the Frederiks threshold field that was introduced in Equation (2.28):

$$H_c = \frac{\pi}{D}\sqrt{\frac{K_1}{\chi_a}}. \tag{4.14}$$

In the geometry of the model, when $\alpha \neq 0,\ b \neq 0$, the following expression for the free energy functional (4.11) is obtained after performing the Taylor expansion of the trigonometric functions and the integration over the z coordinate:

$$F_N \simeq -\frac{2h}{\pi}(\alpha h + b)\theta_0 + \frac{\pi^2 - h^2}{4}\theta_0^2 + \frac{8h}{9\pi}(\alpha h + b)\theta_0^3 + \frac{h^2}{16}\theta_0^4 + o(\alpha^2, b^2, \theta_0^4). \tag{4.15}$$

It can be seen that both the pretilt and the bias field yield linear terms in θ_0. These linear terms cause non-zero director deviation below the threshold field, when $h \ll \pi$. In this region, assuming that θ_0 is small, we can take into account only the first two terms in Equation (4.15):

$$F_N \simeq -\frac{2h}{\pi}(\alpha h + b)\theta_0 + \frac{\pi^2 - h^2}{4}\theta_0^2. \tag{4.16}$$

The solution of the corresponding Euler-Lagrange equation $\partial F_N/\partial\theta_0 = 0$ is

$$\theta_0(h) \simeq \frac{4h(\alpha h + b)}{\pi(\pi^2 - h^2)}. \tag{4.17}$$

Figure 4.10 shows a comparison between two functions of the director deviation angle in the centre of the cell that are either calculated numerically or approximated by Equation (4.17) above. The pretilt angle in this and the following calculations is 2.7°, which corresponds to the pretilt angle in the experimental cell. It can be seen from the graphs that Equation (4.17)) gives a good approximation for the director deviation angle in the region far below the threshold. It diverges when $h \to \pi$ because the denominator in Equation (4.17) approaches zero. In this region, the second term in Equation (4.16) also disappears. So, in order to describe the director deviation, the higher-order terms in θ_0 of the expansion in Equation (4.15) should be taken into account.

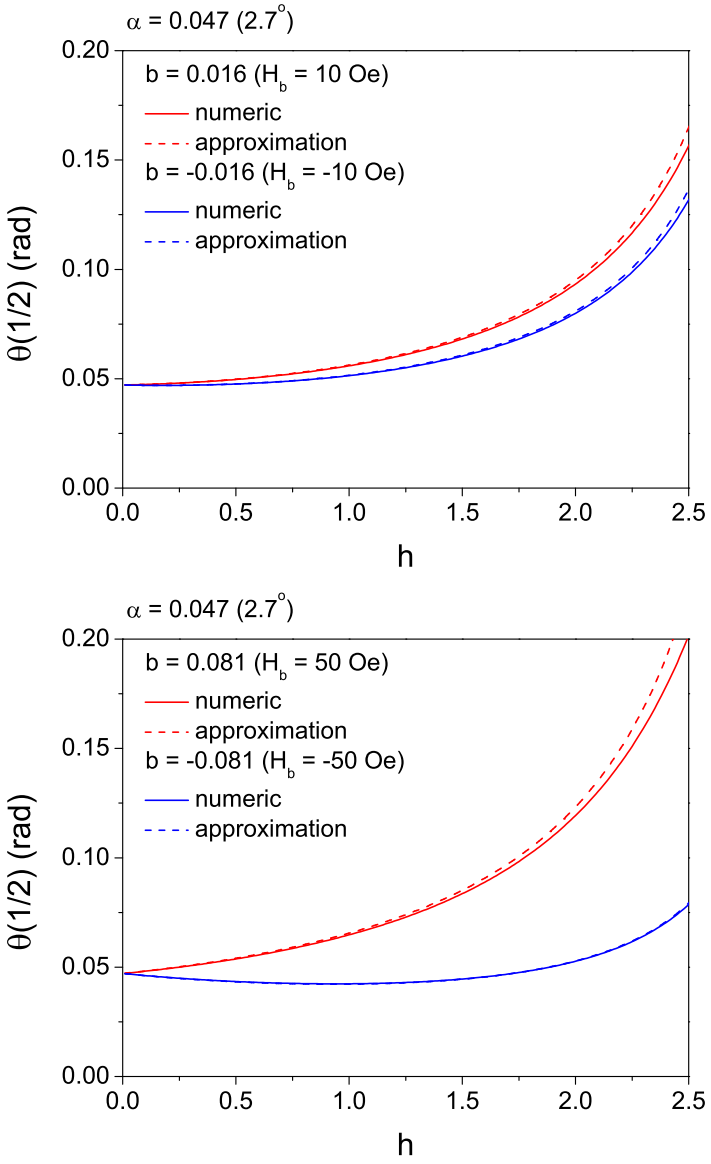

FIGURE 4.10: Comparison of analytic approximation for director deviation angle in the centre of the cell with numerically calculated results for different value of the bias magnetic field.

Another interesting feature shown in Figure 4.10 is a local minimum observed in the curves with negative values of the bias field. To find a position of this minimum, h^*, Equation (4.17) should be differentiated with respect to h. Setting this differential to zero yields the following solution:

$$h^* = -\frac{\alpha\pi^2}{b} \pm \frac{\pi}{b}\sqrt{\alpha^2\pi^2 - b^2}. \tag{4.18}$$

h^* defined by Equation (4.18) has a real positive value when $-\alpha\pi < b < 0$. It should be mentioned that the director deviation angle θ_0 is negative for the

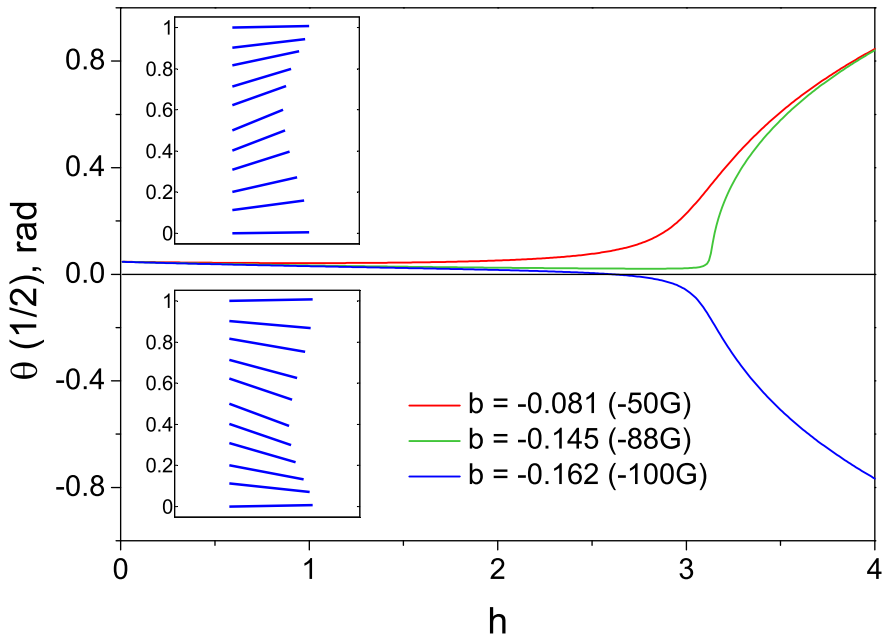

FIGURE 4.11: Director deviation angle at the centre of the cell for different values of the bias field below and above critical value b^* ($b^* = -0.146$ for $\alpha = 0.047$ (2.7°)). The insets illustrate the director profile inside the cell for $h = 4$: the top one, for $b = -0.081$, represents the synclinic configuration; the bottom one, for $b = -0.162$, represents the anticlinic configuration.

dimensionless field value $h = h^*$. The local minimum in $\theta_0(h)$ disappears at $b = -\alpha\pi$, and θ_0 has a negative value over the whole field range below and above the threshold.

Figure 4.11 presents the numerically calculated director deviation angle at the centre of the cell, $\theta(z = 1/2) = \theta_0 + \alpha$, for different negative value of the bias field. The inset to Figure 4.11 depicts the associated director configurations, which can be either "synclinic" ($\theta(1/2) > \alpha$, with director tilt inclined toward the surface pretilt), or "anticlinic" ($\theta(1/2) < \alpha$, with director tilt opposing the surface pretilt). At low test fields h, a negative bias field always favours the anticlinic configuration. However, when $b > b^*$, where $b^* = -\alpha\pi$, the director reorients to the synclinic configuration above the threshold. As the bias field magnitude approaches the critical value b^*, the field-induced reorientation transition sharpens, in a manner resembling the classical Frederiks threshold. At this point, the bias field in some sense just "cancels out" the effect of the pretilt. The same result can be obtained from Equation (4.15). When $h = \pi$ and $b = -\alpha\pi$, all terms except the highest order one in this equation disappear, in the same way as in Equation (4.12) at

$h = \pi$. At this critical bias field, the director field reorientation mode above the threshold switches from the synclinic to the anticlinic configuration.

Unfortunately this result could not be verified experimentally. The critical bias field that corresponds to the pretilt angle of 2.7^o in the experimental cell should be -88.5 Oe. In the experimental set up, however, the maximum bias field that could be produced by the Helmholtz coils was about ± 30 Oe. Above this limit, the coils produced enough heat to significantly increase the temperature of the cell, changing the optical and elastic properties of the nematic.

The next step is to characterise the effect of the bias field direction on the phase lag shift that is described in Section 4.2. This can be done by introducing a function $\Phi_b(h)$ that measures the shift in phase lag with a change of the bias field direction with respect to the bias field absolute value:

$$\Phi_b(h) = \frac{\delta(h,b) - \delta(h,-b)}{2b} \simeq \left.\frac{\partial \delta(h,b)}{\partial b}\right|_{b=0}, \tag{4.19}$$

This function is calculated numerically for different amplitudes of the bias field and is plotted in Figure 4.12. It can be seen that $\Phi_b(h)$ has a maximum close to the threshold magnetic field and that its value is almost independent of the bias field up to the critical value of $|b^*|$.

To determine $\Phi_b(h)$ analytically, the phase lag integral (4.9) should be expanded in a series for small angles. Again, assuming the director orientation angle as $\theta(z) = \alpha + \theta_0 \sin(\pi z)$, the first and second order terms in θ_0 of the Taylor series after integration over the z coordinate become

$$\delta = k_0(n_0 - n_e) + k_0 \nu n_e \left(\frac{\alpha^2}{2} + \frac{2\alpha\theta_0}{\pi} + \frac{\theta_0^2}{4} \right) + o(\alpha^2, \theta_0^2), \tag{4.20}$$

where $k_0 = 2\pi D/\lambda$, $\nu = (n_e^2 - n_o^2)/n_o^2$. After that, $\Phi_b(h)$ is obtained by substituting θ_0 from Equation (4.17) into (4.20) and differentiating with respect to b. The resulting function then becomes

$$\Phi_b(h) = 8 k_0 n_e \nu \frac{\alpha h}{(\pi^2 - h^2)^2}. \tag{4.21}$$

This expression is independent of b, which means that the phase lag shift with a change of the bias field direction, $\delta(b) - \delta(-b)$, is directly proportional to the bias field magnitude. Function $\Phi_b(h)$ expressed by Equation (4.21) is plotted in

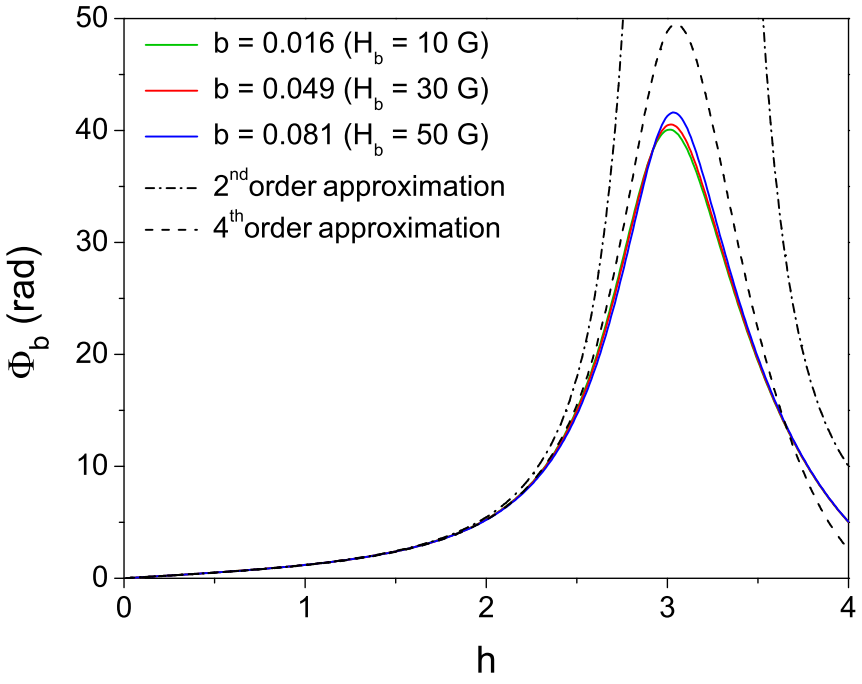

FIGURE 4.12: Numerical estimates of $\Phi_b(h)$ (see Equation (4.19)) for different values of the bias field (solid lines), the second and the fourth order approximation of Φ_b (dash-dot and dot lines).

Figure 4.12 by the dash-dot line. It approximates well to the numerical predictions in the region of small h, however diverges near the Frederiks threshold.

To capture the maximum of $\Phi_b(h)$, the higher-order terms in θ_0 have to be included into the expansion (4.20), and the higher order approximation for $\theta_0(h)$, which is capable of describing the threshold behaviour, have to be used. The Euler-Lagrange equation for θ_0 obtained from Equation (4.15) is

$$-\frac{2h}{\pi}(\alpha h+b)+\frac{\pi^2-h^2}{2}\theta_0+\frac{8h}{3\pi}(\alpha h+b)\theta_0^2+\frac{h^2}{4}\theta_0^3=0. \tag{4.22}$$

Equation (4.22) is a cubic in θ_0, and does not have a simple analytic solution. However, it is a quadratic in h, and can be solved for $h(\theta_0)$. Therefore, the fourth order approximation of Φ_b can be obtained as a function of θ_0, rather than h. These calculations are performed using Maple software. The expression for $\Phi_b(\theta_0)$ is not presented here because of its length. Using the numerically calculated relation between θ_0 and h and the analytical approximation for $\Phi_b(\theta_0)$, the fourth order approximation function of $\Phi_b(h)$ is plotted by the dash line in Figure 4.12. This plot gives a clear indication that the fourth order calculation can describe

the behaviour of the maximum in Φ_b and provide a better approximation to the system over a larger range of magnetic field, including the threshold field.

In the calculation presented above, the one elastic constant approximation is assumed ($p = (K_3 - K_1)/K_1 = 0$). However, p is not small for the liquid crystal E7 ($p \simeq 0.56$). Including the difference between elastic constants into the free energy expansion (4.15) gives the leading order terms containing p as $O(p\alpha\theta_0^3)$ and $O(p\alpha^2\theta_0^2)$. Therefore, the second order approximation is insensitive to the value of p. The fourth order calculations performed with $p = 0$ and $p \neq 0$ showed explicitly that the system behaviour depended only weakly on p at fields close to the Frederiks threshold.

Summary

In this chapter a numerical model which describes the Frederiks transition in a nematic cell, in the presence of easy axis pretilt and in-plane bias magnetic field has been developed. The pretilt and the bias field cause symmetry-breaking effects that destroy the classical Frederiks transition. It has been predicted within the model that changing the direction of the bias field leads to a shift of effective Frederiks threshold; the shift exceeds the value of the applied bias field by a factor of 7. This prediction has been confirmed by achieving a good agreement between experimental data and theoretical curves.

Analytical equations that determine liquid crystal alignment and characterise the effect of the bias field direction on the phase lag shift have also been derived. It has been achieved using an expansion method, with the pretilt, the bias field, and the director deviation angle, acting as small parameters. It has been shown that including only up to the second order terms in the free energy expansion gives a reasonable approximation to the system only in the small field region below the threshold, and diverges near the Frederiks threshold. To describe the system behaviour around the Frederiks threshold, terms in the expansion up to the fourth order have to be taken into account. The analytical solution has predicted an anticlinic director configuration (director deviation opposite to those desired by the pretilt) above the threshold for the negative bias field with the magnitude larger than the critical value.

The numerical model will be extended in Chapter 6 to describe the Frederiks transition in ferronematic suspensions, and will be used to make a comparison

between nematic and ferronematic cells. The effect of the bias field direction should also be taken into account for ferronematic cells not only in the model but also in the experiment. As has been shown before, applying the bias field in different directions can cause a significant shift in the effective Frederiks threshold. Thus, in order to distinguish this effect from the effect of nanoparticles, the same direction of the bias field with respect to the cell position has to be kept during experiments with different ferronematic suspensions.

References

[1] P. G. de Gennes and J. Prost. *The Physics of Liquid Crystals*. Clarendon Press, Oxford, 2nd edition, 1993.

[2] A. Repiova and V. Frederiks. K voprosy o prirode anisotropno-zhidkogo sostoyaniya veshestva (On the problem of the nature of the anisotropic liquid state of matter) (in russian). *Journal of Russian Physical Chemistry Society*, 59:183–200, 1927.

[3] L. M. Blinov. *Electro-optical and Magneto-optical Properties of Liquid Crystals*. Wiley, Chichester, 1983.

[4] A. Rapini and M. J. Papoular. Distorsion d'une lamelle nematique sous champ magnetique: conditions d'ancrage aux parois. *Journal de Physique. Colloques*, 30(C4), 1969.

[5] C. G. Broyden. A class of methods for solving nonlinear simultaneous equations. *Mathematics of Computation*, 19(92):577–593, 1965.

[6] L. N. Trefethen. *Spectral Methods in Matlab*. SIAM, Philadelphia, 2000.

[7] J. R. Taylor. *An Introduction to Error Analysis: the Study of Uncertainties in Physical Measurements*. University Science Books, Sausalito, California, 2nd edition, 1997.

[8] A. M. Mood, F. A. Graybill, and D. C. Boes. *Introduction to the Theory of Statistics*. McGraw-Hill, New York, 3rd edition, 1974.

[9] I.-C. Khoo. *Liquid Crystals*. Wiley, 2nd edition, 2007.

[10] H. L. Ong. Magnetic-field-enhanced and -suppressed Intrinsic Optical Bistability in Nematic Liquid Crystals. *Physical Review A*, 31(5):3450–3453, May 1985.

Chapter 5

Magneto-optic properties of ferronematic suspensions

This chapter presents an experimental study of ferronematic suspensions - suspensions of ferromagnetic nanoparticles in nematic liquid crystals. It focuses on the magneto-optic properties of the ferronematics prepared using several types of nanoparticles with different size, shape and surfactant coatings. Section 5.1 contains an overview of the previous experimental reports in this area, which also describes the type of magnetic materials and the liquid crystals that were used in the preparation of the ferronematic suspensions. It also shows that the ferronematic properties depend on both the magnetic colloidal inclusions and their surface coatings.

Section 5.2 describes two ferronematic suspensions, one prepared with small magnetic nanoparticles of iron oxide and the other with non-magnetic nanorods of α-hematite. The magnetic properties of these suspensions were investigated by performing Frederiks transition experiments in a magnetic field. In the experiments, the magnetic nanoparticle suspensions showed an additional linear response at a low field, while the non-magnetic nanorod suspensions showed no extra response compared to an undoped liquid crystal. A comparison between the experimental results from both suspensions, having the same particle content, proved that the extra linear effect in the ferronematic suspension was only due to the magnetic properties of the doped particles. The magnetic nanoparticle suspensions were also tested using electro-optic measurements. These experiments showed that the suspensions were characterized by the same elastic constants and dielectric constants as the undoped liquid crystal. These results will be used in Chapter 6

in a comparison of the magneto-optic experimental curves with the theoretical calculations.

Section 5.3 discusses another set of ferrosuspensions prepared with magnetite nanorods. This section starts with the description of the nanorod synthesis and their characteristics. After that, the effect of particle surface coating on the suspension stability is investigated using two surfactant materials: Oleic acid (OA) and 4-n-Octyloxybiphenyl-4-carboxylic acid (OBPh). The magnetite nanorod suspensions were characterised using polarized microscopy, clearing temperature measurements, and magneto-optic and electro-optic measurements. The experiments showed that the particle surfactant coating significantly influenced the suspension stability. A better suspension stability and a higher optical quality of cells were achieved in the case of the OBPh stabilized nanorods rather than the OA stabilized nanorods. Finally, the magneto-optic properties of the magnetite nanorod-nematic composite mixture were studied by measuring the magnetic-field-induced Frederiks transition. The experiments demonstrated a decrease in the effective Frederiks threshold, thereby demonstrating an increased sensitivity to magnetic fields for the ferronematic suspension.

5.1 Review of experimental work on ferronematics

An idea of doping liquid crystals with magnetic nanoparticles in order to improve their sensitivity to magnetic fields came from the theoretical work of Brochard and de Gennes in 1970 [1]. After this paper, some attempts have been made to realize ferronematic suspensions experimentally. An overview of the main experimental reports from different groups is presented here.

The first ferronematic suspensions based on thermotropic liquid crystals were reported by Chen and Amer in 1983 [2]. Their ferronematic suspensions consisted of methoxybenzyledene butylanine (MBBA) nematic doped with a small amount (a volume concentration between 1.86×10^{-7} and 2.66×10^{-6}) of $\gamma - Fe_2O_3$ needles, with a length of 0.5 μm and an aspect ratio of 7:1. The particles were coated by dimethyl octadecyl aminopropyl trimethoxysilyl chloride, the surfactant which provided liquid crystal alignment perpendicular to the particle surfaces. The suspensions were studied in homeotropic liquid crystal cells. They investigated how the variation of the cell birefringence, induced by applying an external magnetic

field, depended on the cell thickness and on the concentration of nanoparticles. An optical response at a low magnetic field ($H < 10$ Oe) was detected in their samples; this response increased with increasing either the cell thickness or the particle content. However, the magnetic particles flocculated at higher fields ($H > 50$ Oe for the lowest concentration and $H > 10$ Oe for the highest concentration), which resulted in non-uniform complex textures observed in the cells by cross-polarized microscopy. This aggregation of particles seemed to be irreversible, suggesting that their suspensions were not stable and the results were unrepeatable. Moreover, a similar magneto-optic response, reported in this paper, was not reproduced later in the literature.

In later reports [3, 4], Chen studied an electro-optic effect in the same ferroparticle suspensions. He detected a decrease in the effective Frederiks threshold voltage depending on the magnetic field that was applied simultaneously to the cell with ferronematic suspension. No decrease in the threshold voltage was detected in the undoped nematic cell under the same conditions. The threshold shift detected in the ferronematic cell was proportional to the magnetic field strength. It was explained by the magnetically induced tilt of the host nematic as a result of its interaction with magnetic particles. The magnetic field in this experiment was kept below 10 Oersted, which was the maximum field they could apply without causing strong particle aggregation.

Another set of papers, concerning ferronematic suspensions, was reported by Kopčanský *et al.* Their first suspensions were prepared using small (average diameter $\sim$ 10 nm), almost spherical nanoparticles made of magnetite Fe_3O_4 and coated by Oleic acid. The host media were different thermotropic liquid crystals: nematics 4-heptyl-4'-cyanobiphenyl (7CB) [5], methoxybenzyledene butylanine (MBBA) [6], 4-alkyl-4'-cyanobicyclohexyl (ZLI 1695, Merck) [7, 8], 4-(trans-4'-n-hexylcyclohexyl)–isothiocyanatobenzene (6CHBT) [9], and smectic 4-n-octyl-4'-cyanobiphenyl (8CB) [10, 11, 12]. They measured the reorientation transition in ferronematic cells induced not only by the magnetic fields, but also by a combination of magnetic and electric fields. The liquid crystal reorientation was detected by measuring the capacitance of the cell. It needs to be noted that they did not report on either stability or optical properties of their ferronematic suspensions.

These experiments indicated that doping different liquid crystals with the same magnetic particles could cause different effects: the magnetic or electric Frederiks threshold could be shifted either up or down. The authors explained this phenomenon using the Burylov-Raikher theory [13, 14]. The difference in the effects

of the same nanoparticles on different liquid crystals arises from different equilibrium orientation between the nematic director ($\boldsymbol{n}$) and the magnetic particle orientation (magnetic director $\boldsymbol{m}$). When the nematic and magnetic directors are pointed in the same direction ($\boldsymbol{n} \parallel \boldsymbol{m}$), an external field applied perpendicular to them ($\boldsymbol{H} \perp \boldsymbol{n}, \boldsymbol{m}$) rotates the particles, causing the reorientation of the nematic director at a lower field. In the case of normal alignment between the particle magnetic moments and the nematic director ($\boldsymbol{n} \perp \boldsymbol{m}$), an external field applied perpendicular to $\boldsymbol{n}$ but parallel to $\boldsymbol{m}$ stabilizes the nanoparticle orientation, which hinders the director reorientation. Therefore, the Frederiks transition requires higher fields. Using planar or homeotropic cells and applying the combination of electric and magnetic fields, they corroborated the type of anchoring between the nematic and magnetic orientations. The perpendicular alignment between $\boldsymbol{n}$ and $\boldsymbol{m}$ was found in 7CB and 8CB based suspensions and the parallel alignment was found in MBBA, 6CHBT and ZLI1695 based suspensions [8].

These authors also estimated an effective surface coupling energy between nematic and nanoparticles from the shift of the effective Frederiks threshold. The calculations were performed using equations for the threshold field derived by Burylov and Raikher [14]. The values of the surface coupling energy varied for different liquid crystals in the range between $(2.3 - 0.4)$ erg cm^{-2} for 8CB [12] and $(5.5 - 0.3) \times 10^{-3}$ erg cm^{-2} for ZLI 1695 [7].

In another report [15], they studied the effect of particle shape on the effective coupling energy. Three types of Fe_3O_4 ferroparticles were selected for this study. They were either spherical particles with a mean diameter of 11.6 nm, or chainlike particles with a diameter of 34 nm and a chain length of 446 nm, or nanorods with a mean diameter of 80 nm and a length of 1200 nm. Suspensions with the same concentration of the particles in liquid crystal 6CHBT were prepared and studied. They measured the orientation transitions induced by a magnetic field in cells that were at the same time biased by an electric field ($\boldsymbol{H} \perp \boldsymbol{E}$). The threshold magnetic fields were shifted to lower values in all cells with the suspensions, compared to the cells with the undoped liquid crystal. This shift strongly depended on the particle morphology with the largest effect observed in the rodlike particle suspension. The surface coupling energy estimated from the threshold fields was reported to be of the order of $\sim 10^{-2}$ erg cm^{-2} for the spherical particles, ~ 1 erg cm^{-2} for the chainlike particles and ~ 10 erg cm^{-2} for the rodlike particles.

In recent work [16], Kopčanský *et al.* reported on ferronematic suspensions that were prepared using single wall carbon nanotubes functionalized with magnetic

particles of Fe_3O_4. These particles with a size from 10 to 25 nm were synthesized on the surface of the nanotubes functionalized with the carboxyl group ($-COOH$). Magnetization of the functionalized nanotubes was up to 40 times higher than for the bare nanotubes. When both types of nanotubes were added to 6CHBT nematic liquid crystal at a low volume concentration (2×10^{-4}), an electric-field-induced Frederiks transitions was measured in planar cells filled either with the undoped 6CHBT or with suspensions of nanotubes whether functionalized or not. During the experiment, the cells were biased by a constant magnetic field. The magnetic field was applied in the direction of the initial director alignment and the electric field was applied perpendicular to it. An increase in Frederiks threshold voltages was observed with increasing the bias magnetic field strength. The shift of the threshold voltages was higher in the cell with the functionalized nanotube suspension than in the cells with the undoped nematic and with the bare nanotube suspension. This leads to a conclusion that the nanotubes were aligned parallel to the nematic director. The effective surface anchoring energy, estimated from the threshold voltage shift, varied within the range of $(8.8 - 1.1)$ erg cm^{-2} and $(150 - 55)$ erg cm^{-2} for suspensions with the bare and with the magnetically functionalized nanotubes, respectively.

Another magnetic dopant, based on carbon nanotubes, was investigated recently by the group of Reznikov [17]. They prepared a low concentration suspension of multi-wall carbon nanotubes filled with α-Fe in nematic 5CB. Besides the Frederiks transition in the magnetic field, they also investigated the optical properties of the colloids. Formation of large, elongated agglomerates ($5 - 50$ μm in length) of the nanotubes was detected in the suspension. The aggregation was explained by the magnetic dipole and van der Waals interactions between nanotubes. The elongated shape of aggregates was forced by anisotropy of the elastic forces in the surrounding liquid crystal medium. Despite the aggregation, this suspension demonstrated much higher magnetic sensitivity - it optically responded to an external field of only 50 Oersted.

To prepare a stable ferronematic suspension, it is necessary to coat particles with the suitable surfactant. This means that the interaction between nematic and ferroparticles, and hence the suspension properties, are determined not only by the particle characteristics (their size and shape, or magnetic properties) but also by the type of surfactant. In the experimental reports discussed above, however, mainly only one surfactant - Oleic acid - was used for most types of nanoparticles. The first detailed investigation of the surfactant effect on the suspension properties was reported by a group of Martinez-Miranda and Cordoyiannis. They

investigated suspensions of $FeCo$ magnetic nanoparticles of 11 nm or 2 nm size in smectic A liquid crystal 8CB. The nanoparticles were functionalized with different surfactants: n-hydroxy succinimide (NHS), polyethelene glycol (PEG 3000), aminopropyl tri-ethoxy silane (APTS), and mercapto hexa-decanoic acid (MHDA). These suspensions were characterised by measuring the deformation of smectic layers induced by the magnetic field [18, 19] and by investigating isotropic-to-nematic and nematic-to-smectic A phase transitions [20]. They found that by varying the surface coating of nanoparticles, they caused different impacts on the suspension properties, resulting in different responses to a magnetic field or in different phase transition temperatures. These results prove the impact of the surfactant on the properties of ferrosuspensions.

5.2 Suspensions with spherical magnetic nanoparticles and with hematite nanorods

The aim of this section is to investigate the effect of particle characteristics on the properties of ferronematic suspensions. It considers two types of ferronematic suspensions prepared with different nanoparticles that were coated with the same surfactant. The first set of ferronematic suspensions was prepared using magnetic nanoparticles of iron oxide (Fe_xO_y) obtained from Sigma-Aldrich Company Ltd. They were supplied as a heptane-based dispersion stabilized by Oleic acid. Using transmission electron microscopy (TEM) images of nanoparticles (see Figure 5.1), produced by Dr. Mark Herrington, it was possible to determine that the ferroparticles were almost spherical, with an average diameter between 15 and 20 nm.

A second set of suspensions was prepared using α-hematite (α-Fe_2O_3) polydisperse nanorods (Nanostructured & Amorphous Materials, Inc.). Their diameter varied from 40 to 30 nm and the length was between 250 and 600 nm. The TEM image provided by the supplier is presented in Figure 5.2. The nanorods were supplied as a powder. Before adding them into the liquid crystal, the nanorods were dispersed in heptane with the addition of Oleic acid to prevent their aggregation.

These two types of nanoparticles were chosen because of their different magnetic properties. In the suspension of iron oxide nanoparticles, based on the particle size, it is possible to assume that the Brownian relaxation process dominates over the Néel relaxation mode (see Section 2.3.1). This means that the magnetic moments are rigidly coupled to the ferroparticle crystallographic structures, so they

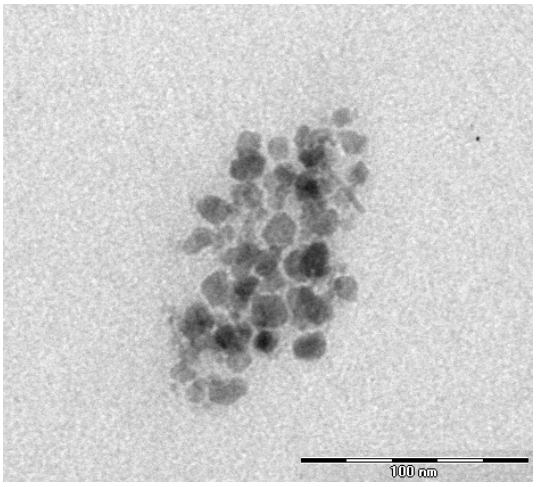

FIGURE 5.1: TEM image of magnetic iron oxide nanoparticles.

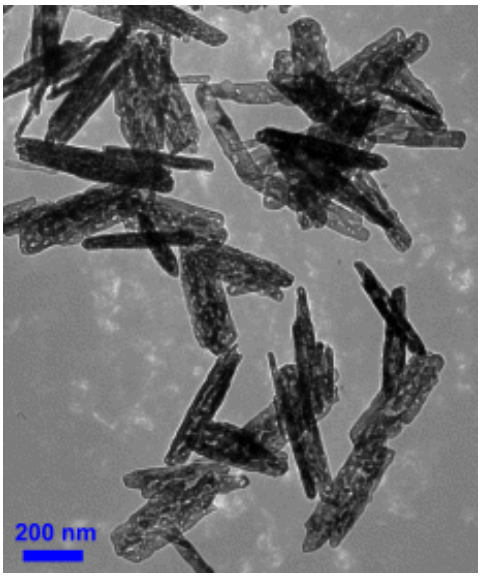

FIGURE 5.2: TEM image of α-Fe_2O_3 nanorods.

should demonstrate ferromagnetic behaviour. α-Fe_2O_3 nanorods, on the other hand, are known to have weak ferromagnetic properties at room temperature [21]. The magnetic properties of nanoparticles can be verified by a simple test. A small magnet is brought close to the bottles containing the nanoparticle heptane-based suspensions. The magnetic nanoparticles quickly move towards the magnet, showing their high sensitivity to the external magnetic field. The nanorod suspension, however, does not react to the approaching magnet at all, indicating that the nanorods have limited magnetic response.

Ferronematic suspensions were prepared using the nematic liquid crystal E7 (Merck). The heptane-based suspension of nanoparticles was added to the liquid crystal and

mixed well using an ultrasound bath. This mixture was heated to a temperature above 70 °C and left for a day for the solvent to evaporate. During this time, the mixture was mechanically shaken several times to uniformly distribute the nanoparticles. Using this method, suspensions with three different concentrations of each type of nanoparticles in a liquid crystal were prepared. These concentrations were 0.1%, 0.05% and 0.01% by weight, which corresponded to the volume concentrations, $f = 2 \times 10^{-4}$, 1×10^{-4} and 2×10^{-5}, respectively. The concentrations were estimated from the amount of nanoparticles in the initial heptane-based suspension that was added to the liquid crystal. After the solvent had evaporated, each suspension was sonicated in an ultrasound bath for 10 min and then filled into a standard 50 μm thick liquid crystal cell. The structure of this cell is described in Section 3.2. All cells had a good planar alignment with a small pretilt angle of $\alpha = (2.7 \pm 0.1)^\circ$ and without visible defects. The pretilt angle was measured independently by a crystal rotation method (see Section 3.2.2); and it did not differ from the pretilt in the cell with undoped E7. Moreover, the pretilt stayed the same after exposing the cell to a strong magnetic field during the magneto-optic experiment.

5.2.1 Results of the magneto-optic and electro-optic experiments

The Frederiks transition experiments in the magnetic field for a set of cells filled with the suspensions were carried out. A description of the experiment can be found in Section 3.3. The first experiments, results of which are shown in Figure 5.3 - 5.5, were performed by Dr. Oleksandr Buchnev using the magneto-optic set up in Institute of Physics, Kiev, Ukraine. The following analysis of these experimental data and further investigation of these suspensions, including the electro-optic measurements presented in this section, is the author's own work.

The experimental dependence of the cross-polarized intensity on the magnetic field measured in the cells with the magnetic nanoparticle suspensions and also with the undoped nematic are presented in Figure 5.3. The black curve corresponds to the undoped nematic cell. Detailed analysis of the Frederiks transition in the undoped liquid crystal was discussed in Chapter 4. For this curve, the Frederiks transition starts at a critical field of $H_c \simeq 1.5$ kOe. As discussed before, this transition is smoothed due to a surface pretilt and an in-plane bias field. The green, red and blue curves correspond to the cells with different concentration suspensions. Two interesting effects can be observed from these curves. Firstly, the variation

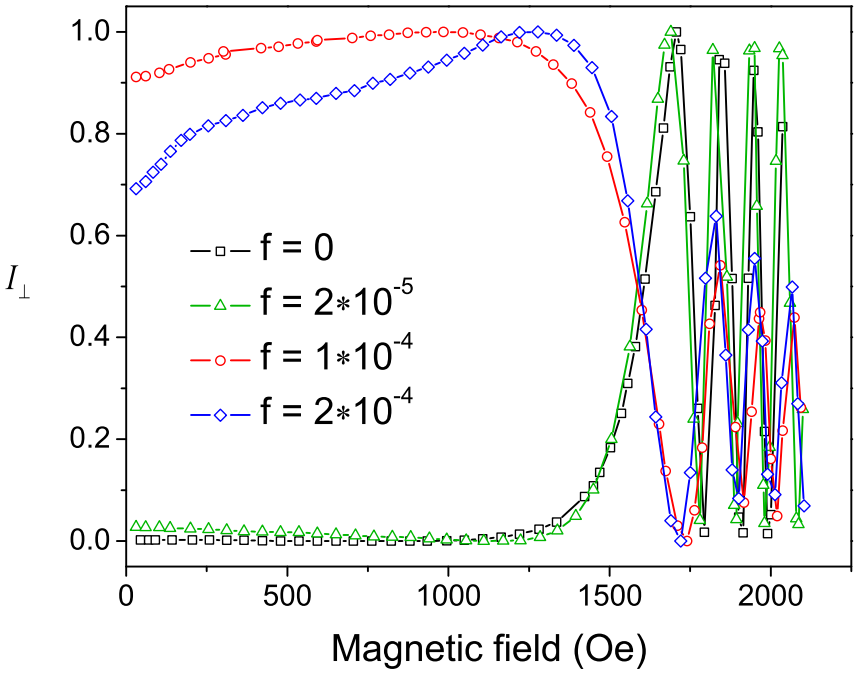

FIGURE 5.3: Experimental measured dependences of cross-polarized intensity on magnetic field for cells with undoped nematic and magnetic nanoparticle suspensions (see legend).

of the intensity in the ferronematic cells can be observed at a low magnetic field ($H < 100$ Oe), far below the Frederiks threshold in the undoped cell. The second effect is a decrease in the amplitude of intensity oscillations observed in the cells with high concentration suspensions in the high field region. The origin of this decrease will be discussed later in Section 5.2.2.

Let us concentrate on the first effect that happens in the low field region, below 500 Oersted. It is easy to characterize the experimental data plotted in terms of the phase lag shift rather than the cross-polarized intensity. The phase lag depending on the magnetic field strength is shown in Figure 5.4. It can be seen from the inset in Figure 5.4 that there is a response to the low field in the ferro-suspension cells. This response is linear with field and it increases with increasing nanoparticle concentration f. These results demonstrate that the suspensions can "feel" the magnetic fields of the order of only 100 Oersted. In addition, the phase lag curves become smoother near the threshold field, and the effective transition occurs at lower fields than in the undoped liquid crystal. Thus, the effective Frederiks thresholds shift from 1.50 kOe in the undoped E7 cell to approximately 1.45 kOe in the lowest concentration suspension and to 1.35 kOe in the highest concentration suspension.

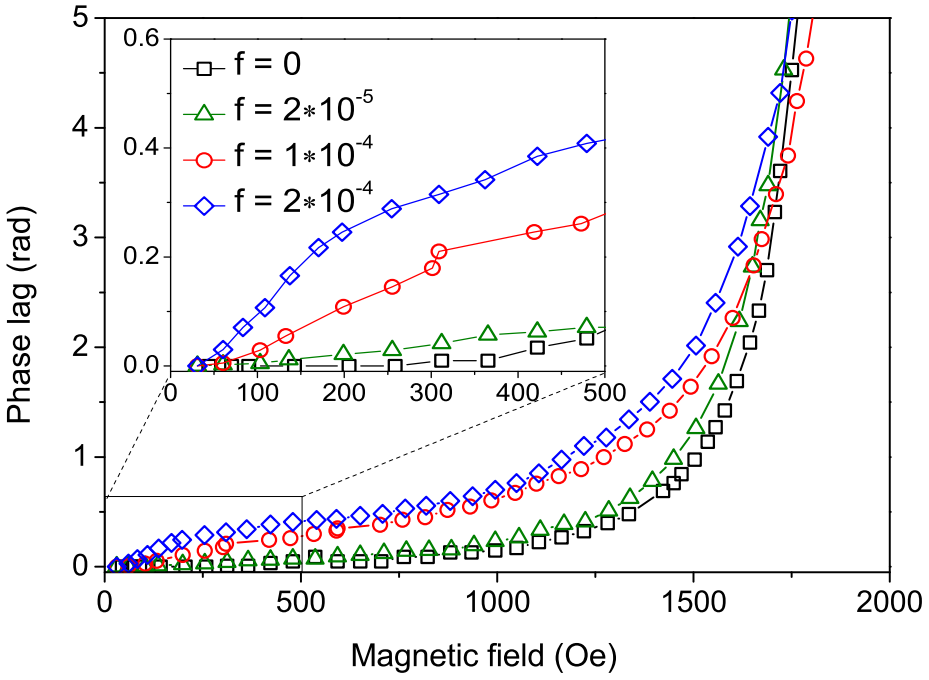

FIGURE 5.4: Change of the phase lag as a function of magnetic field for cells with undoped nematic and suspensions with magnetic nanoparticles.

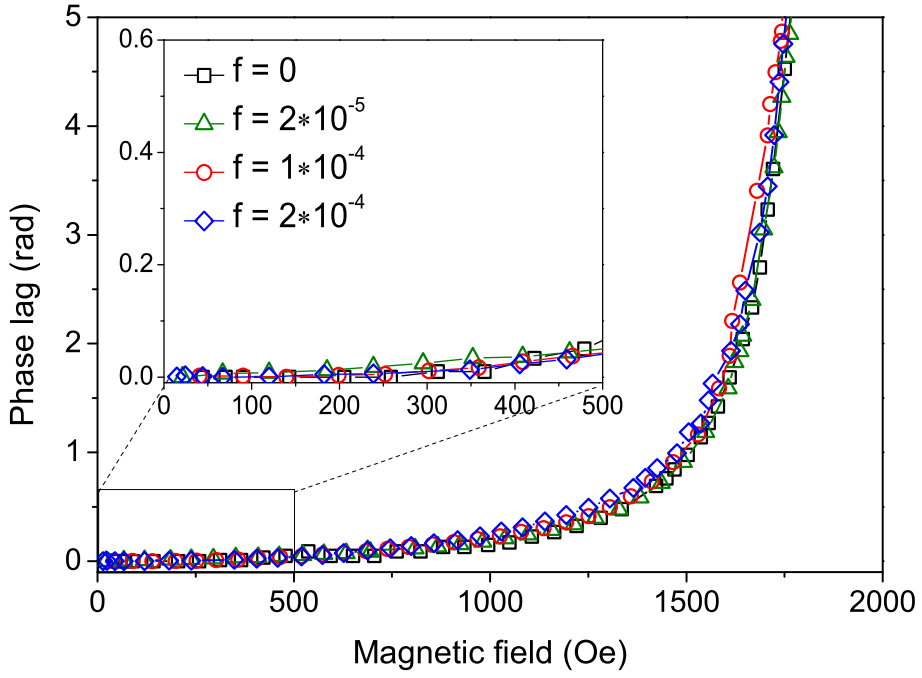

FIGURE 5.5: Change of the phase lag as a function of magnetic field for cells with undoped nematic and α-hematite nanorod colloidal suspensions.

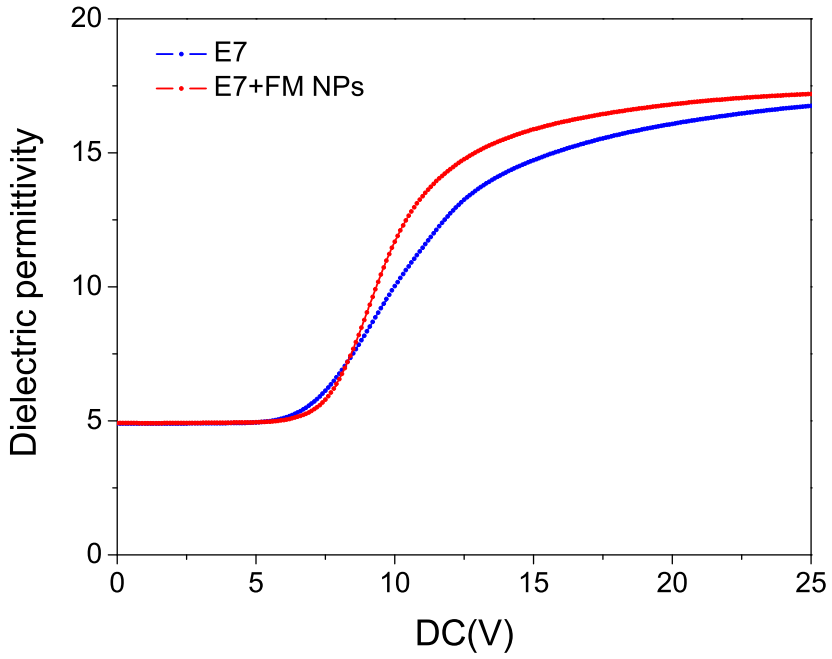

FIGURE 5.6: Dependences of the effective dielectric permittivity of the liquid crystal layer in the cells containing nematic E7 (blue line) and Fe_xO_y nanoparticle suspension with particles volume fraction of $f = 2 \times 10^{-4}$ (red line). The data are obtained from the capacitance measurements.

Results of the analogous magneto-optic measurements for the cells with α-Fe_2O_3 nanorod suspensions are plotted in Figure 5.5. There is no discernible difference between these measurements and those in the undoped liquid crystal. The colloidal components of the two suspensions are matched in concentration, and are made from chemically similar material, but their magnetic properties are very different. This means that the linear effects observed in the Fe_xO_y nanoparticle suspensions are only due to their magnetic properties. Moreover, doping liquid crystals with a low concentration of nanoparticles (volume concentration less than 2×10^{-4}) does not affect any of the liquid crystals characteristics, such as elastic constants, diamagnetic anisotropy, etc., which might cause the shift in the Frederiks threshold.

To verify that the ferronematic suspensions with low concentration of Fe_xO_y nanoparticles have the same elastic constants as undoped liquid crystals, the electro-optic measurements were performed. For these experiments two 12 μm thick guard electrode cells were filled with the undoped E7 and the most concentration nanoparticle suspension (volume fraction of nanoparticles $f = 2 \times 10^{-4}$). The structure of the guard electrode cell is described in Chapter 3.

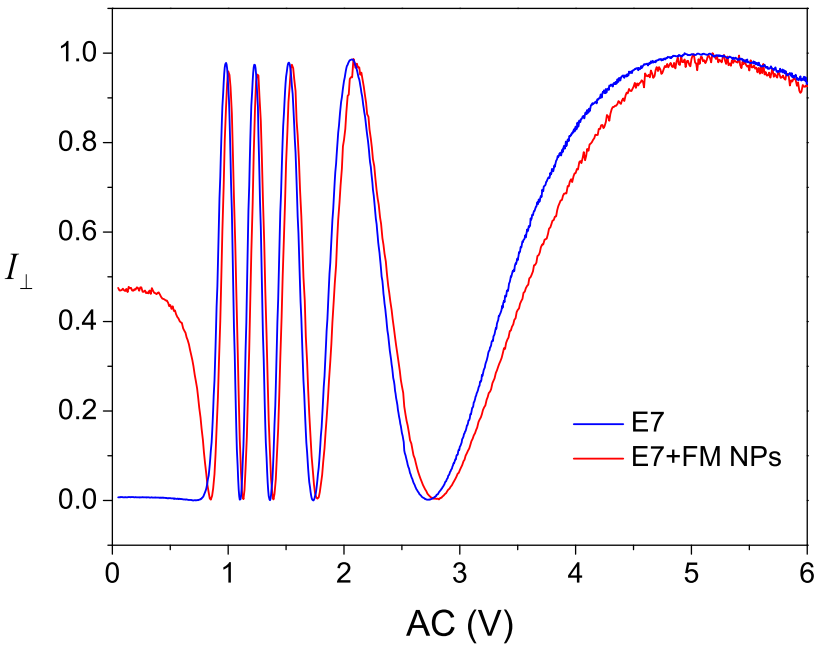

FIGURE 5.7: Experimental dependence of the normalized cross-polarized intensity on the AC Voltage for nematic E7 (blue line) and Fe_xO_y nanoparticle suspension with particles volume fraction of $f = 2 \times 10^{-4}$ (red line).

Firstly, the capacitance of these cells depending on DC electric field was measured by an autobalance bridge method (see Section 3.4.1 for details). An effective dielectric permittivity of liquid crystal layers was extracted by comparing the capacitance data with the previously measured capacitances of the empty cells. The corresponding dependences of the effective dielectric permittivities on DC electric field are presented in Figure 5.6. The dielectric permittivity at $V = 0$ corresponds to $\varepsilon_\perp$. At high voltages, the saturated value of dielectric permittivity corresponds to $\varepsilon_\parallel$. Based on the experimental curves, the dielectric constants of the undoped E7 are $\varepsilon_\perp = 4.900 \pm 0.005$, $\varepsilon_\parallel = 17.30 \pm 0.02$ and of the ferronematic suspension are $\varepsilon_\perp = 4.915 \pm 0.005$, $\varepsilon_\parallel = 17.32 \pm 0.02$. A comparison between these values shows that the dielectric constants of the highest concentration suspension do not differ significantly from the dielectric constants of E7. Thus, it is possible to assume that the lower concentration suspensions is also characterised by the same dielectric permittivities as the undoped E7.

After that, the Frederiks transition experiment in AC electric field was carried out. In this experiment, the cross-polarized intensity dependences on AC electric fields were measured for the same guard electrode cells containing the undoped nematic and the ferronematic suspension, using the set up described in Section 3.4.2.

The experimental curves are compared in Figure 5.7. The difference in the starting points of the curves is caused by a possible difference in the cell thicknesses. However, the intensity oscillations in both curves start at the same point, around 0.6 Volt, indicating the same Frederiks threshold voltages. Moreover, these curves almost overlap above the threshold. Taking into account that the suspensions are characterised by approximately the same dielectric constants, these results can be interpreted as an indication that the ferronematic suspension has the same elastic constants as E7. This conclusion again can be generalized to the lower concentration suspensions. It will be taken into account in the following fitting of the magnetic-field-induced Frederiks transition experimental data for the magnetic nanoparticle suspensions, which is presented in Chapter 6.

5.2.2 Stability of magnetic nanoparticle suspensions

At the next stage, the stability of colloidal Fe_xO_y particles in the suspensions is analysed. This helps us to understand the microscopic processes in the suspensions and explains the decrease in the amplitude of cross-polarized intensity oscillations that can be observed in Figure 5.3. The suspension stability was verified by repeating the magneto-optic experiment after a six month interval. The uniformity of nanoparticle distribution inside the cells was analysed using optical microscopy.

The Frederiks transition experiment in the magnetic field was repeated using the same cells and the same magneto-optic set up after a time interval of about six months. The experimental results demonstrated generally similar trends to those presented on Figure 5.4: a liner response to a low magnetic field and a decrease of the effective Frederiks threshold. However, these new results showed a slight divergence from the original data taken six months before. In particular, they demonstrated a lower ferronematic response for the same cells. The divergence between old and repeated data is large for the cell with higher concentration suspension. In some sense, the new results resembled the response measured in some lower concentration suspensions. The repeated results are not presented here; they will be shown in Section 6.4, together with a quantitative analysis of the decrease in the ferronematic response obtained from the numerical model.

The observed changes in the repeated experimental results may indicate a process of nanoparticle aggregation which had taken place over the six month interval. A magneto-optic response measured for a cell with nanoparticle suspension depends on the suspension concentration (see Figure 5.4). If nanoparticles form a cluster,

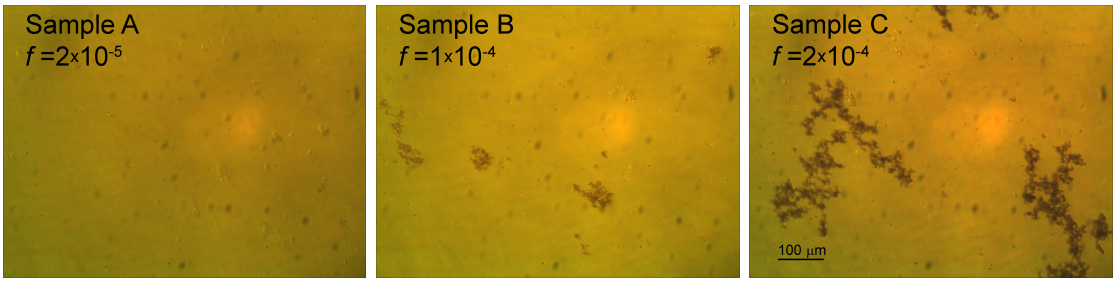

FIGURE 5.8: Optical microscope images of the cells containing magnetic nanoparticle suspensions with different concentrations.

they become in some sense excluded from the suspension volume. The magnetic moment of particles in a cluster is screened by the neighbouring particles of the same cluster, making an effective suspension magnetization smaller. A cluster can be considered as a particle with a large size. So, a partly aggregated suspension should be equivalent to a suspension of larger particles but with lower effective nanoparticle concentration. If clusters of particles become too large, they can produce significant distortion of liquid crystal around them, causing some additional effects that will be discussed later.

Some direct evidence of particle aggregation was obtained by microscopy. Microscopic images of three cells containing suspensions of different concentrations of Fe_xO_y nanoparticles were taken six months after preparing the cell, using an Olympus BX51 microscope and an Olympus DP12 camera. The images are presented in Figure 5.8. It should be mentioned that the particles are too small to be singly visible on the images. Any spot on the images indicates a cluster of particles. The cell with the lowest concentration suspension ($f = 2 \times 10^{-5}$) appears uniform without noticeable defects or particle clusters. However, the relatively large aggregates with a size up to 100 μm are observed in the cells with the higher concentration suspensions (with $f = 1 \times 10^{-4}$). The cell with the highest concentration of nanoparticles ($f = 2 \times 10^{-4}$) contains even more aggregates with a size above 100 μm and with a complex, irregular shape.

The large clusters of particles are detected in those cells where the reduced intensity amplitude was observed in the Frederiks transition experiment (see Figure 5.3). Micrometre-sized aggregates are able to cause local distortions of the nematic director around them [22]. These non-uniform director distortions might cause scattering and depolarization of light as it passes through the cell. This, in turn, would lead to a decrease in the intensity oscillation amplitude measured in the partly aggregated suspensions. To verify this hypothesis and to study the

behaviour of aggregates and the director distortions around them, microscopy images of the samples should be taken when the external magnetic field is applied to the cell. Unfortunately, the present set up does not allow doing that.

The recent paper of Buluy *et al.* [17] has investigated the behaviour of magnetic nanoparticle clusters, which were carbon nanotubes filled with α-Fe, in nematic 5CB under the influence of magnetic field. Their findings showed that the aggregates were formed during 8 hours after preparing the suspension. As expected, they observed local nematic distortions around the big aggregates. Applying the external magnetic field caused the individual reorientation of the aggregates that led to non-uniform reorientation of the director in the surrounded region. The director distortions increased in size with an increase of the external magnetic field, leading to stronger light scattering and higher level of polarization distortion. They also observed a decrease in output intensity with increasing magnetic field applied to their sample. Similar director distortions might occur around aggregates in our suspensions, which could explain the decrease in the intensity amplitude when the magnetic field strength is increased.

5.3 Ferronematic suspensions with magnetite nanorods

The next set of ferronematic suspensions was prepared using magnetite particles with a rodlike shape. The effect of the two surfactants: Oleic acid (OA) and 4-n-Octyloxybiphenyl-4-carboxylic acid (OBPh), on particle stability in the suspension was investigated. The magneto-optic measurements were also performed using the more stable suspension prepared with OBPh coated nanorods.

The magnetite nanorods were synthesized and characterized by Dr. Dmitry Bavykin from Engineering Sciences, University of Southampton. The nanorod synthesis consisted of two stages. At the first stage, single crystal magnetite nanoparticles were synthesized by oxidation of colloidal $Fe(OH)_2$ with air in an aqueous solution at pH 7; this method was recently reported by Vereda *et al.* [23]. The nanoparticles are characterized by a single crystal structure, an angular shape, and a wide distribution in particle sizes (see Figure 5.9a). The average nanoparticle size is approximately 20 nm. From a high resolution transmission electron microscope (HRTEM) image (see inset in Figure 5.9a), the interlayer spacing can be estimated as 0.48 nm, corresponding to the (111) planar spacing of spinel-type

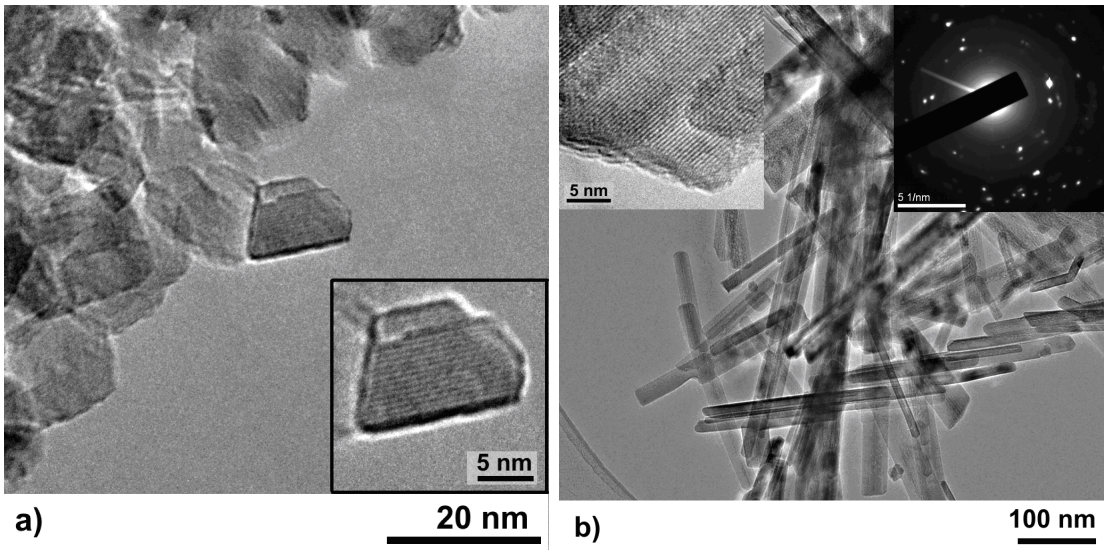

FIGURE 5.9: TEM images of magnetite (a) nanoparticles and (b) nanorods. Inset shows higher magnification images and SAED for bungle of nanorods

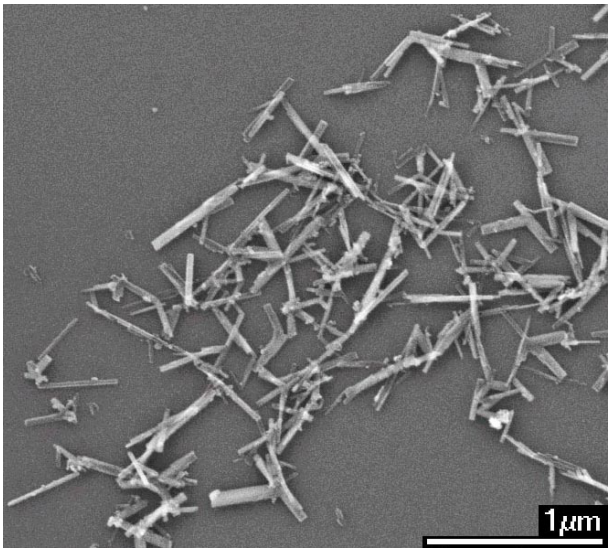

FIGURE 5.10: SEM image of magnetite nanorods.

magnetite [24]. During the second stage, the nanoparticles were transformed to the nanorods through recrystallization. This was achieved by an alkaline hydrothermal treatment of the magnetite nanoparticles with a 10 mol dm^{-3} concentration solution of $NaOH$ at 100°C lasting 48 hours. The resulting dark brown solid precipitate was separated, washed with water using filtration, and finally subjected to vacuum drying.

The magnetite nanorods were characterized using transmission electron microscopy (TEM) and scanning electron microscope (SEM) techniques. According to the

SEM data (see Figure 5.10), the nanorods are also characterized by a wide distribution in size, with an average diameter of 20 nm and a length of approximately 500 nm. The HRTEM image in the top left inset of Figure 5.9b demonstrates conclusively that the nanorods are single crystals and that the distance between lattice planes is also 0.48 nm. The selected area electron diffraction (SAED) image taken from the nanorods bundle (see top right inset in Figure 5.9b) shows narrow diffraction dots confirming the single crystal structure of the magnetite nanorods.

The first trial ferronematic suspension with the magnetite nanorods was prepared by adding a small amount of dry particle powder to the nematic liquid crystal E7 and mixing it well using a high power ultrasonic probe. The resulting suspension was initially quite uniform. However, the particles aggregated very rapidly with time, causing both precipitation and an uneven distribution of the magnetic material. This suspension was tested in the magneto-optic experiment. The results demonstrated a high level of noise in the collected signal and were unrepeatable, indicating that the time of suspension stability was shorter than the experiment duration. Large aggregates of particles were also observed under a polarized microscope in that cell immediately after the experiment.

5.3.1 Effect of surfactant on uniformity of nanorod suspensions

To stabilize nanorods in suspensions, they should be coated with a suitable surfactant agent. Surfactant molecules attach themselves to the particle surface, preventing the aggregation process by imposing a steric repulsion between particles and by improving interaction with E7 molecules. Two different surfactants were tried with the magnetite nanorods: Oleic acid (OA) obtained from Aldrich, and 4-n-Octyloxybiphenyl-4-carboxylic acid (OBPh) obtained from Alpha Aesar. Their chemical formulas are shown in Figure 5.11. Oleic acid is commonly used for preparing liquid-crystal-based suspensions of magnetic [15] and ferroelectric [25, 26] nanoparticles. It binds to iron oxide surfaces through the carboxylic ($-COOH$) group and prevents the aggregation of particles by the steric repulsion between carbon tails. However, previous experimental results (see Section 5.2.2) demonstrate that Oleic acid does not stabilize the magnetic nanoparticles well enough to prevent their aggregation. OBPh, however, besides the carboxylic group for binding with iron oxide surface, has the octyloxybiphenyl moiety that resembles a structure of E7 molecules. So, it should interact with the liquid crystal via

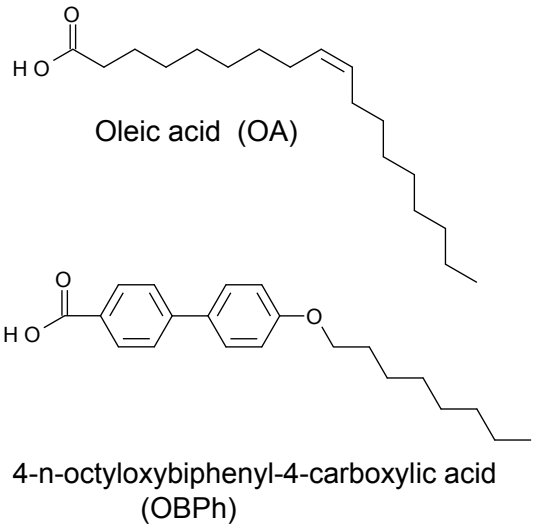

FIGURE 5.11: Molecular formula of Oleic acid and 4-n-Octyloxybiphenyl-4-carboxylic acid.

a stacking mechanism. Recently, OBPh has been successfully employed on the surface of gold nanoparticles in cyanobiphenyl liquid crystal suspensions [27].

Two ferronematic suspensions with the nanorods coated by OA and by OBPh were prepared using the following procedure. First, 10 mg of the dry nanorod powder was mixed with 10 cm^3 of solvent (acetone or hexane) with the addition of 9 mg of OBPh or 0.008 cm^3 of OA, respectively. Both mixtures were sonicated in an ultrasound bath for 60 minutes and then left for 1 minute to settle down. After that, 5 cm^3 of the mixture was collected from the top and mixed with 0.3 g of nematic liquid crystal E7. The solvent was removed from this mixture in a rotary vacuum evaporator under a pressure of 200 mbar and at a temperature of 40 °C. The resulting suspensions had a brownish colour (see Figure 5.12). They were too dense to be used in the magneto-optic experiment (the nanorods concentration is estimated to be $\sim$ 1.5% by wt.). So, the suspensions were diluted by 100 times with E7, which created the final suspensions with an estimated nanorod content of 0.015% by wt., or a volume concentration of 3×10^{-5}. However, the real amount of nanorods in the ferronematic suspension is likely to be lower because not all of the particles were entirely dissolved in the solvent and some of them precipitated. The ferronematic suspensions were sonicated again for a further 10 minutes and filled into standard, 50 μm thick cells.

As expected, more stable suspensions were achieved using OBPh. A photo of the two bottles with the initial, 1.5% concentration suspensions taken several days after the suspension preparation is shown in Figure 5.12. The precipitation of OA

FIGURE 5.12: Photo of bottles with 1.5 wt.% concentration suspensions of OBPh (bottle on the left) and OA (bottle on the right) coated magnetite nanorods in nematic E7.

coated nanorods is visible in the bottle on the right. The suspension of OBPh treated particles stays uniform without particle separation for a couple of months. The better stability of OBPh coated nanorods leads to improved optical quality of the cell containing the diluted suspension. This has been confirmed using polarized optical microscopy (POM). POM images of the cells containing suspensions of two type nanorods coated by OA and OBPh are presented in Figure 5.13. Bright and dark POM images, depending on the liquid crystal alignment direction with respect to the polarizer axes, indicate a good quality planar alignment in both cells. However, the large aggregates (10-100 μm in size) of OA coated nanorods can be easily seen on the left image in Figure 5.13. The cell containing the suspension of OBPh coated nanorods shows more uniform distribution of particles, and the large aggregates are now no longer present. Thus, this suspension was used in the following magneto-optic experiments, the result of which will be discussed in Section 5.3.3.

Carboxylic acids are known to have good adhesion with iron oxide. For this reason, the use of both OA and OBPh produces highly stable suspensions of nanorods in the solvents (hexane or acetone). However, when a medium around nanorods changes to the nematic E7, the degree of surfactant adsorption at the nanoparticle surfaces might decrease. There is a possibility that some amount of surfactant molecules may be transfered to the suspension bulk, causing some changes to the suspension properties. It is possible to perform additional purification of nanorod suspensions before transferring them into the nematic. However, this might also

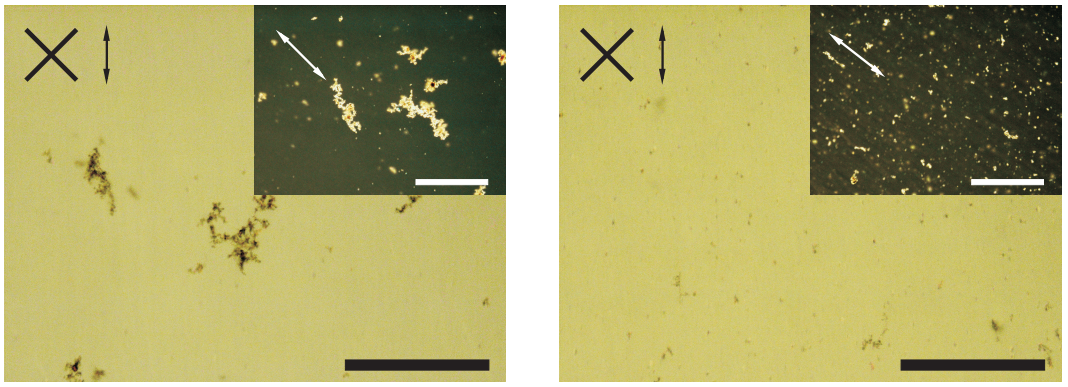

FIGURE 5.13: Polarized optical microscopy images of the cells containing the diluted suspensions of OA (left) and OBPh (right) coated magnetic nanorods. Crossed lines indicate the polarizer axes, line with arrows indicates the liquid crystal alignment direction. Scalar bars correspond to 200 μm.

wash out a surfactant from the particle surface, leading to a lower suspension stability. Another method for separating the possible effects of OA or OBPh from the effects of the magnetite nanorods is to study separately some extra suspensions containing only surfactant molecules in the nematic. To perform this, the extra nematic suspensions doped with OBPh or OA molecules at the same concentrations as in the nanorod suspensions were prepared and tested along with the nanorod-nematic suspensions.

5.3.2 Clearing temperature measurements

The next experiment consisted of measuring a clearing temperature - a temperature of phase transition between nematic and isotropic states. Standard, planar liquid crystal cells were used in this experiment. The cell was placed on a Mettler FP82 hot stage. The temperature of the hot stage was slowly increased at a rate of 0.1°C per minute, which was controlled by a Mettler FP80 central processor. The hot stage had a small window that allowed optical observation of the liquid crystal texture in the cell. The phase transition in the cell was visually observed using an Olympus CH-2 polarizing microscope, two polarizers of which were crossed. At this polarizer position, a bright uniform texture was observed when the suspension in the cell was in the nematic state because of the birefringence of the liquid crystal molecules. As the transition temperature was reached, small bubbles of the isotropic phase appeared in the cell. The isotropic phase has no birefringent properties, so droplets of this phase were seen as black spots in the cell texture.

TABLE 5.1: The clearing temperature of undoped nematic (E7), suspensions with OBPh and OA coated magnetite nanorods (E7+MNRs+OBPh and E7+MNRs+OA) and suspensions with surfactant molecules (E7+OBPh and E7+OA). Clearing temperatures are measured to an accuracy of 0.1°C.

LC/suspension	Clearing temperature, °C
E7	60.1
E7+MNRs+OBPh	59.1
E7+MNRs+OA	58.5
E7+OBPh	59.6
E7+OA	59.6

With a further temperature increase, the isotropic bubbles increased in size until they occupied the whole cell area. The clearing temperature corresponded to the state when the entire area under observation had made the transition to the isotropic phase.

Table 5.1 lists the clearing temperatures of the undoped nematic, the suspensions with OBPh and OA coated nanorods, and also the suspensions containing surfactant molecules alone. In all these suspensions a drop in the clearing temperature was observed. In the suspensions, adding either OBPh or OA to E7 caused the same decrease in the phase transition temperature, namely 0.5°C. A higher decrease in the clearing point was detected in the suspensions containing nanorods coated with these surfactants. However, the suspension with OA coated nanorods had a lower clearing temperature than the suspension with OBPh treated nanorods. The difference in clearing temperature was 0.6°C, a rather significant quantity. It should be mentioned that the clearing temperatures were measured to an accuracy of 0.1°C. This difference indicates that the strength of the interaction between the nanorods and the liquid crystal molecules depends strongly on the type of particle coating. The higher the transition temperature, the stronger the orientational nanoparticle-nematic coupling is to be expected [28, 29]. In our case, the higher phase transition temperature indicated a higher nanorod-liquid crystal molecule interaction in the E7+MNRs+OBPh solution than in the E7+MNRs+OA solution. This is also in agreement with the better dispersion of OBPh coated nanorods in the suspension observed in the microscope images in Figure 5.13.

5.3.3 Magneto-optic response in magnetite nanorod suspension

In the next stage of the investigation, the magnetic-field induced Frederiks transition was measured in cells containing the suspensions with OA and OBPh coated magnetite nanorods (E7+MNRs+OA and E7+MNRs+OBPh), as described in Section 3.3. For each suspension a set of cells was prepared and measured in the experiment. The selected results that give the best representation of magneto-optic responses from each batch of cells are shown in Figure 5.14. Each curve represents a single experiment on the selected cell from the batch.

The magneto-optic responses from the nanorod suspensions are also compared to the results measured in an undoped nematic cell (E7) in Figure 5.14. The cross-polarized intensity for both suspensions begins to oscillate at lower fields indicating a decrease in the effective Frederiks threshold for the suspensions in comparison with the undoped nematic. Moreover, the shift in the transition threshold is higher in the E7+MNRs+OBPh cell that in the other suspension. The figure also shows some noise in E7+MNRs+OBPh suspension at low fields. This can be connected

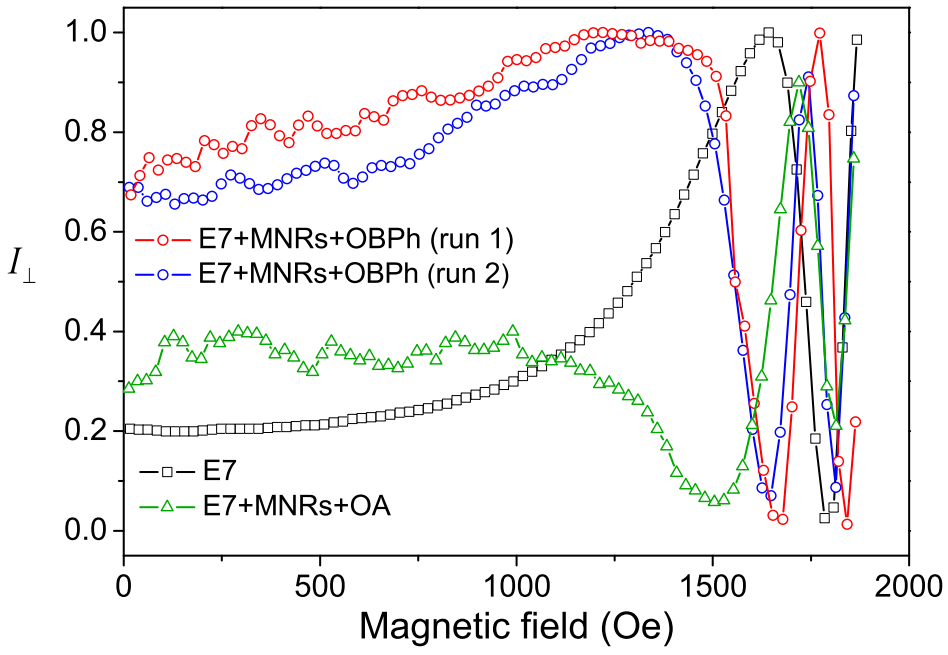

FIGURE 5.14: Experimental dependence of cross-polarized intensity on magnetic field for the cells with undoped nematic (E7) and OA- and OBPh-stabilized magnetite nanorod suspensions (E7+MNRs+OA and E7+MNRs+OBPh). Run 1 and 2 indicate different measurements performed with the same cell after one week interval.

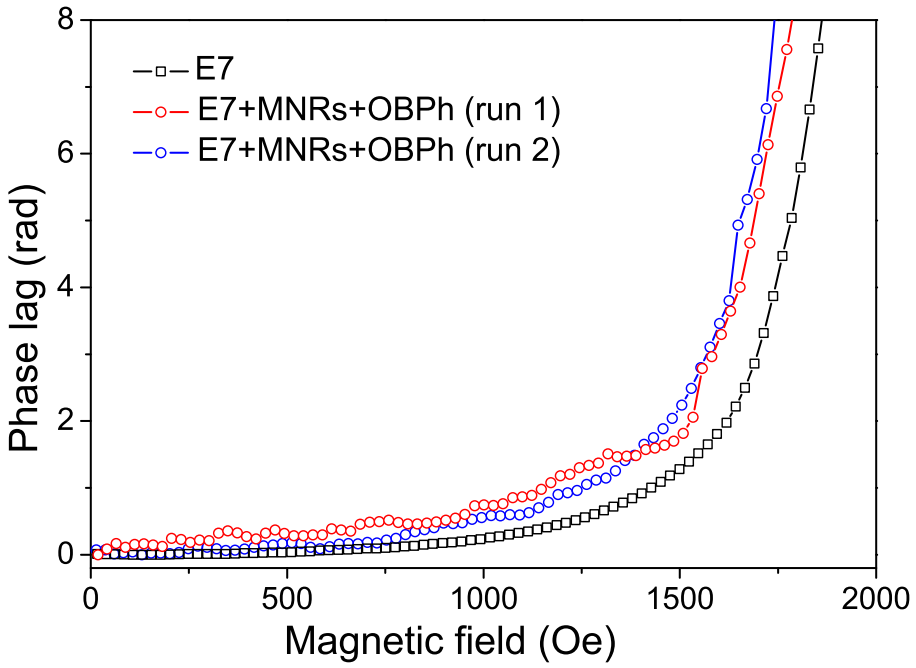

FIGURE 5.15: Change of the phase lag as a function of magnetic field for the cells with undoped nematic (E7) and OBPh-stabilized magnetite nanorod suspension (E7+MNRs+OBPh). Run 1 and 2 indicate different measurements performed with the same cell after one week interval.

with some flow of the nanorods. When the particles move inside the cell, the average number of them in the beam cross section varies. This effect is expected to be more significant for the magnetite nanorods as they have a larger size than the spherical nanoparticles. The results from the E7+MNRs+OA suspension show a higher level of noise, which agrees with a large size of the nanorod clusters in this suspension (see Figure 5.13). There is also a decrease in the amplitude of the output intensity from this cell at a high field - the effect observed before in the concentrated suspensions of spherical nanoparticles. In the E7+MNRs+OBPh cell however, the intensity oscillation reaches 0 and 1, which is in agreement with the absence of large aggregates in this cell.

To test the repeatability of results from E7+MNRs+OBPh suspension, the experiment with this cell has been performed twice: the first run - immediately after a cell preparation and the second run - after an interval of one week; both of these results are plotted in Figure 5.14 and 5.15. The optical response measured in the first experiment is higher at a low magnetic field, but it is also much nosier in comparison with the response from the second experiment. However, at a high field they are very close to each other. Experiments repeated later showed almost the

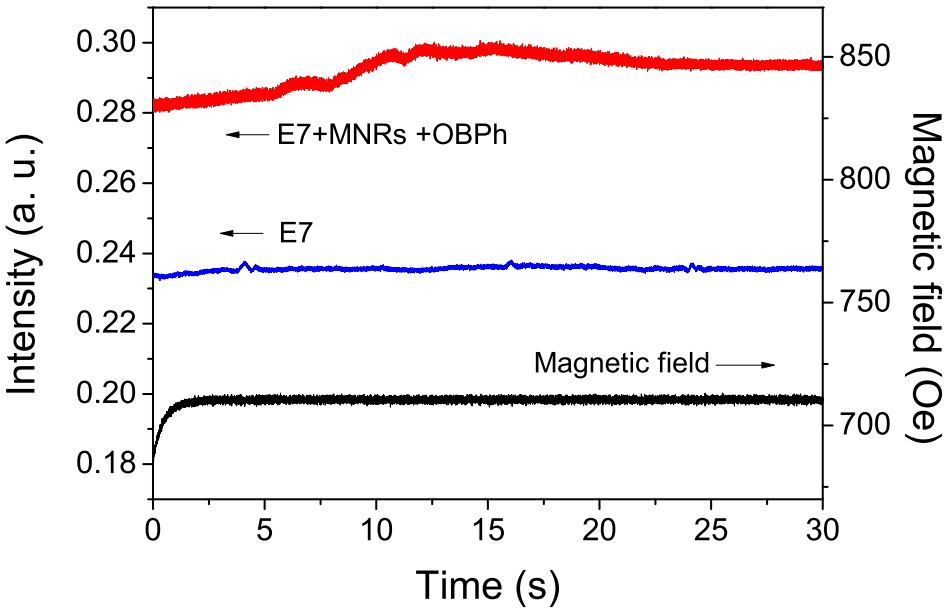

FIGURE 5.16: Optical signal collected from the cells containing undoped nematic (E7, blue curve) and OBPh-stabilized magnetite nanorod suspension (E7+MNRs+OBPh, red curve) when the magnetic field increases from 690 to 710 Oersted (black curve).

same result as during the second run. This might indicate some processes of particle relaxation that happens in recently prepared suspensions. After settling down, the suspension of OBPh treated nanorods remained stable for at least a month, demonstrating repeatable results. Because of that, only E7+MNRs+OBPh suspension will be further considered in this work.

The effective Frederiks transition is easy to analyse from Figure 5.15, where the results are plotted in terms of how how the phase lag change depends on the magnetic field strength. The transition in the cell with undoped E7 occurs at a magnetic field of around 1.5 kOe. The cell with magnetite nanorod suspension, by contrast, demonstrates the effective Frederiks transition at about 1.2 kOe, which is around 20% lower than the threshold in the undoped E7 cell. Moreover, a noticeable optical response in the E7+MNRs cell can be detected at a magnetic field strength of approximately 700 Oersted. Figure 5.16 shows the time dependence of the normalized laser beam intensity collected after transmission through the cells with undoped nematic and nanorods suspension as the magnetic field is increased from 690 to 710 Oersted. In the undoped E7 cell, there is essentially no change in the transmitted laser beam intensity as the field is changed. The laser beam intensity transmitted through the E7+MNRs cell, by contrast, changes noticeably

at the same field strength. The same optical response can be detected in the E7 cell only at a magnetic field above 1,000 Oersted. This explicitly indicates the higher magnetic sensitivity of the nanorod suspension.

It is possible to assume that an even stronger magneto-optic response could be achieved by increasing the amount of magnetic particles in the suspension. However, with increasing particle content, the average distance between them becomes smaller and they might aggregate, making the suspension unstable. This was investigated by testing a cell with a doubled nanorod concentration suspension in the magneto-optic experiment, the first results of which indeed demonstrated a higher optical response at both low and high magnetic fields. However, the low field response had a high level of noise. Repeated measurements detected a decrease in the effective Frederiks threshold, which became almost the same as in the lower concentration suspension, thus, indicating the aggregation of nanorods in the suspension.

To verify that the surfactant itself made no direct contribution to the magneto-optic properties of the suspension, additional magneto-optic measurements using cells containing the suspensions of only OBPh or OA molecules were performed. Here the same results as in the undoped E7 cell were obtained, verifying that the OBPh or OA by themselves have no effect.

The electo-optic measurements, which include capacitance measurements and Frederiks transition experiments in AC electric fields (see Section 3.4), have also been performed using a cell with a low concentration magnetite nanorod suspension. The results from both of these experiments, similar to the case with the magnetic nanoparticle suspension, do not differ from those measured in the undoped nematic cell. So, the capacitance measurements indicated that the dielectric constants did not change with the liquid crystal doping, and the Frederiks transition experiment indicated that the suspension had the same elastic constants as undoped nematic. This also meant that the lower magnetic field threshold in the magnetite nanorod suspension was the result of nanorod magnetic properties only.

Summary

The magneto-optic properties of ferronematic suspensions have been investigated experimentally in this chapter. As suggested from the previous experimental reports, the properties of suspensions depend on both the type of colloidal inclusion and their surface coating. In this study, three different types of iron oxide nanoparticles were used: spherical magnetic nanoparticles, α-hematite nanorods, and magnetite nanorods. The first two types of nanoparticles were coated with Oleic acid. Magnetite nanorods were stabilized using either Oleic acid (OA) or 4-n-Octyloxybiphenyl-4-carboxylic acid (OBPh). The ferronematic suspensions had a low nanoparticles content (volume fraction lower than 2×10^{-4}). The suspension properties have been investigated by magnetic-field-induced Frederiks transition experiments and by electro-optic measurements.

Frederiks transition in a cell with undoped E7 have been detected at a threshold field of around 1,500 Oersted. The Frederiks transition experiment performed with the cells containing spherical magnetic nanoparticle suspensions have demonstrated a thresholdless, linear optical response to a low magnetic field, below 500 Oersted. The linear response increases with increasing nanoparticle concentration and can be clearly detected at a field strength of only 100 Oersted. Moreover, an effective Frederiks threshold in these cells is observed at up to 10% lower fields as compared to the cell with undoped nematic. A much higher threshold decrease, by around 20%, has been detected in the cell with magnetite nanorod suspension. However, the linear low field response is not as apparent in this suspension as in the spherical nanoparticle suspensions. On the other hand, the third, α-Fe_2O_3 nanorod suspensions show no extra magneto-optic response as compared to the undoped nematic. These nanorods have very weak magnetic properties at room temperature. Comparison between experiments with α-Fe_2O_3 nanorod suspensions and other suspensions indicates that the additional ferronematic effects in the magnetic nanoparticle and magnetite nanorod suspensions are only due to their magnetic properties. This also means that doping nematics with a low nanoparticle concentration has no effect on the liquid crystal properties, which may cause the decrease in the Frederiks threshold. This conclusion has also been confirmed by the results of electro-optic measurements, which have indicated that the suspensions are characterized with the same dielectric constants and elastic constants as E7.

Suspension stability strongly depends on the type of particle surfactant. Magnetic nanoparticles have been coated with Oleic acid, a surfactant which crates

a highly stable suspension of nanoparticles in the solvent (heptane). However, the particles form aggregates after transferring to the liquid crystal medium. The size of aggregates in the suspensions increases with the particle concentration, reaching hundreds of microns. At these sizes, the aggregates could cause non-uniform distortions of the nematic host around them. These distortions might cause scattering and depolarization of light, explaining the drop in the intensity amplitude oscillations observed in Frederiks transition experiments. Other magnetite nanorods have been stabilized using either OA or OBPh. Utilizing OBPh yields more stable nanorod suspensions in nematic E7 with a more uniform particle dispersion compared to OA. The clearing temperature in the suspension containing OBPh coated nanorods is 0.6°C higher that in the "equivalent" suspension of OA coated nanorods. This indicates that there is a stronger interaction of liquid crystal molecules with the OBPh coated nanorods. Suspensions of OBPh treated nanorods also produce more stable and repeatable results in Frederiks transition experiments.

References

[1] F. Brochard and P. G. de Gennes. Theory of magnetic suspensions in liquid crystal. *Journal de Physique (Paris)*, 31:691–708, 1970.

[2] S.-H. Chen and N. M. Amer. Observation of macroscopic colective behavior and new texture in magnetically doped liguid crystal. *Physical Review Letters*, 51(25):2298–2301, 1983.

[3] S.-H. Chen and B. J. Liang. Electo-optic effect of a magnetically biased ferronematic liquid crystal. *Optics Letters*, 13(9):716–718, 1988.

[4] B. J. Liang and S.-H. Chen. Electric-field-induced molecular reorientation of a magnetically biased ferronematic liquid-crystal film. *Physical Review A*, 39:1441–1446, 1989.

[5] M. Koneracká, V. Kellnerová, P. Kopčanský, and T. Kuczynski. Study of magnetic Fredericksz transition in ferronematic. *Journal of Magnetism and Magnetic Materials*, 140–144:1455–1456, 1995.

[6] M. Koneracká, V. Závišová, P. Kopčanský, G. Czechowski, and B. Żywucki. Study of magnetic Fredericksz transition in ferronematics. *Journal of Magnetism and Magnetic Materials*, 157/158:589–590, 1996.

[7] P. Kopčanský, I. Potočová, M. Koneracká, M. Timko, J. Jadzyn and G. Czechowski, and A. G. M. Jansen. The structural instabilities of ferronematic based on liquid crystal with low negative magnetic susceptibility. *Physica Status Solidi (b)*, 236(2):450–453, 2003.

[8] P. Kopčanský, N. Tomašovičová, M. Koneracká, M. Timko, V. Závišová, N. Eber, K. Fodor-Csorba, T. Toth-Katona, A. Vajda, J. Jadzyn, E. Beaugnon, and X. Chaud. The structural instabiliteis in ferronematic based on liquid crystal with negative diamagnetic susceptibility anisotropy. *Journal of Magnetism and Magnetic Materials*, 322:3696–3700, 2010.

[9] P. Kopčanský, I. Potočova, M. Koneracká, M. Timko, A. G. M. Jansen, J. Jadżyn, and G. Czechowski. The anchoring of nematic molecules on magnetic particles in some types of ferronematics. *Journal of Magnetism and Magnetic Materials*, 289:101–104, 2005.

[10] I. Potočová, M. Koneracká, P. Kopčanský, M. Timko, L. Tomčo, and J. Jadzyn and G. Czechowski. The influence of magnetic field on electric Fredericksz transition in 8CB-based ferronematic. *Journal of Magnetism and Magnetic Materials*, 201:163–166, 1999.

[11] I. Potočová, P. Kopčanský, M. Koneracká, L. Tomčo, M. Timko, and J. Jadzyn and G. Czechowski. The structural instabilities in ferronematics and ferrosmectics. *Journal of Magnetism and Magnetic Materials*, 252: 150–152, 2002.

[12] P. Kopčanský, I. Potočová, M. Timko, M. Koneracká, A. G. M. Jansen, and J. Jadzyn and G. Czechowski. The structural transition in ferronematics in combined electric and magnetic fields. *Journal of Magnetism and Magnetic Materials*, 272–276:2355–2356, 2004.

[13] S. V. Burylov and Yu. L. Raikher. Macroscopic properties of ferronematics cause by orientational interactions on the particles surface. I Extended continuum theory. *Molecular Crystals and Liquid Crystals*, 258:107–122, 1995.

[14] S. V. Burylov and Yu. L. Raikher. Macroscopic properties of ferronematics cause by orientational interactions on the particles surface. II Behavior of real ferronematics in external field. *Molecular Crystals and Liquid Crystals*, 258: 123–141, 1995.

[15] P. Kopčanský, N. Tomašovičová, M. Koneracká, V. Závišová, M. Timko, A. Dzarova, A. Sprincova, N. Eber, K. Fodor-Csorba, T. Toth-Katona, A. Vajda, and J. Jadzyn. Structural changes in the 6CHBT liquid crystal doped with spherical, rodlike, and chainlike magnetic particles. *Physical Review E*, 78:011702, 2008.

[16] Z. Mitróová, N. Tomašovičová, M. Timko, M. Koneracká, J. Kováč, J. Jadzyn, I. Vávra, N. Éber, T. Tóth-Katona, E. Beaugnon, X. Chaud, and P. Kopčanský. The sensitivity of liquid crystal doped with functionalized carbon nanotubes to external magnetic fields. *New Journal of Chemistry*, 35: 1260–1264, 2011.

[17] O. Buluy, S. Nepijko, V. Reshetnyak, E. Ouskova, V. Zadorozhnii, A. Leonhardt, M. Ritschel, G. Schönhense, and Yu. Reznikov. Magnetic sensitivity of a dispersion of aggregated ferromagnetic carbon nanotubes in liquid crystals. *Soft Matter*, 7:644–649, 2011.

[18] L. J. Martinez-Miranda, K. McCarthy, L. K. Kurihara, J. J. Harry, and A. Noel. Effect of the surface coating on the magnetic nanoparticle smetic-a liquid crystal interaction. *Applied Physics Letters*, 89:161917, 2006.

[19] L. J. Martinez-Miranda and L. K. Kurihara. Interacton and response of a smetic-a liquid crystal to a nanometer particle: phase transition due to the combined effect of the functionalization compound and particle size. *Journal of Applied Physics*, 105:084305, 2009.

[20] G. Cordoyiannis, L. K. Kurihara, L. J. Martinez-Miranda, C. Glorieux, and J. Thoen. Effect of magnetic nanoparticles with different surface coating on the phase transitions of octylcyanobiphenyl liquid crystal. *Physical Review E*, 79:011702, 2009.

[21] I. Dzyaloshinsky. A thermodynamic theory of weak ferromagnetism of antiferromagnetics. *Journal of Physics and Chemistry of Solids*, 4:241–255, 1958.

[22] H. Stark. Physics of colloidal dispersions in nematic liquid crystals. *Physics Reports*, 351:387–474, 2001.

[23] F. Vereda, J. de Vicente, M. del Puerto Morales, F. Rull, and R. Hidalgo-Alvarez. Synthesis and characterization of single-domain monocrystalline magnetite particles by oxidative aging of $Fe(OH)_2$. *Journal of Physical Chemistry C*, 112(15):5843–5849, 2008.

[24] R. M. Cornell and U. Schwertmann. *The Iron Oxides: Structure, Properties, Reactions, Occurences and Uses*. Wiley-VCH, Weinheim, Germany, 2nd edition, 2003.

[25] Yu. Reznikov, O. Buchnev, O. Tereshchenko, V. Reshetnyak, A. Glushchenko, and J. West. Ferroelectric nematic suspension. *Applied Physics Letters*, 82: 1917–1919, 2003.

[26] H. Atkuri, G. Cook, D. R. Evans, C.-I. Cheon, A. Glushchenko, V. Reshetnyak, Yu. Reznikov, J. West, and K. Zhang. Preparation of ferroelectric nanoparticles for their use in liquid crystalline colloids. *Journal of Optics A: Pure and Applied Optics*, 11:024006, 2009.

[27] S. Khatua, P. Manna, W.-S. Chang, A. Tcherniak, E. Friedlander, E. R. Zubarev, and S. Link. Plasmonic nanoparticles - liquid crystal composites. *Journal of Physical Chemistry C*, 114(16):7251–7257, 2010.

[28] L. M. Lopatina and J. V. Selinger. Theory of ferroelectric nanoparticles in nematic liquid crystals. *Physical Review Letters*, 102:197802, 2009.

[29] L. M. Lopatina and J. V. Selinger. Maier-Saupe-type theory of ferroelectric nanoparticles in nematic liquid crystals. *Physical Review E*, 2011.

Chapter 6

Modelling ferronematic suspensions

This chapter describes a theoretical model for the magneto-optic response in ferronematic cells. The model is based on the continuum theory of ferronematics, which was developed by Brochard and de Gennes [1] and modified by Burylov and Raikher [2, 3]. The main concepts of the ferronematic theory are outlined in Section 6.1. In particular, Section 6.1.1 introduces a coupling between ferroparticles and nematic molecules in ferronematic suspensions as predicted by the Burylov-Raikher theory, and Section 6.1.2 describes the orientational and optical effects in ferronematics, according to the model developed by Zadorozhnii *et al.* [4].

A new approach to modelling ferronematics is suggested in Section 6.2. Unlike the previous models [3, 4], the proposed theory is extended to include not only the ferromagnetic effect of particles, but also the nematic diamagnetic effect. This allows the present model to predict the ferronematic response in a larger range of magnetic fields. Section 6.2 compares the effects of the particle ferromagnetism and nematic diamagnetism on the ferronematic response by analysing some experimental results from Chapter 5. Section 6.3 develops the governing equations that describe a ferronematic cell in a magnetic field. The cell geometry corresponds to the magneto-optic experiment, so it includes a surface pretilt of the nematic director and a bias magnetic field, the importance of which has been shown in Chapter 4. There are only two unknown parameters in the model which describe, respectively, the effective ferroparticle-field interaction and the ferroparticle-nematic director interaction. These parameters are determined in Section 6.4 by comparing the results of the model with the experimental magneto-optic curves for different ferronematic suspensions that are presented in Chapter 5.

6.1 Continuum theory of ferronematics

The idea of doping liquid crystals with nanoparticles came from the pioneering work of Brochard and de Gennes in 1970 [1], in which the authors considered theoretically a suspension of ferromagnetic nanoparticles (ferroparticles) in a nematic liquid crystal. The ferroparticles had rod-like shape with a length L and diameter d, which were much larger than the nematic molecule size and $L/d \sim 7 - 10$. In the theory, they introduced a coupling between the nematic and the ferroparticles. This ensured that any rotation of ferroparticles by the external magnetic field would be transferred to the nematic matrix.

Depending on the particle concentration, two different scenarios in ferronematic systems were predicted. When the particle concentration is low, each particle can only disturb the nematic matrix in a small volume around it. This distortion does not overlap with the distortions caused by other particles, so the main volume of the nematic remains undisturbed. However, when the particle concentration is high enough, any uniform rotation of ferroparticles by a magnetic field can cause a uniform distortion of the whole nematic host. This scenario is called the "collective behaviour". In this case, it is possible to neglect the individual orientation of each particle, and to describe all particles by a macroscopic function of bulk magnetization, which is expected to change smoothly throughout the ferronematic volume. The nematic matrix can also be treated as a uniform sample, ignoring some local director distortions around the particles.

By considering the collective behaviour, Brochard and de Gennes developed the first continuum theory of ferronematics. In their theory they assumed a rigid coupling between a nematic director and the ferroparticle magnetization. This meant that the nematic orientation was always aligned with the magnetization vector. However, this is a very unsupported assumption which does not have either experimental or theoretical confirmation.

6.1.1 Ferronematic theory of Burylov and Raikher

The Brochard-de Gennes theory was extended by Burylov and Raikher to the case of a soft coupling between a nematic and ferroparticles [5]. The nature of this coupling was explained by the anisotropy of nematic anchoring energy on the particle surface. As the particle size was considered to be much larger than the nematic molecules size, the surface anchoring energy was assumed to be in the

Rapini-Papoular form (see Equation (2.23)). Considering deformations caused by a single rod-like particle in the liquid crystal matrix [2, 6], they showed that the surface anchoring energy was proportional to $\pi K L w_{BR}$ and the energy of local nematic distortions around one particle was proportional to $\pi K L w_{BR}^2$, where K was an elastic constant, and also that

$$w_{BR} = \frac{W_s d}{K} \tag{6.1}$$

was a dimensionless coupling parameter. It scaled the coupling energy to the elastic energy around single particle [7]. W_s was the surface anchoring energy density.

The parameter w_{BR} determines the type of anchoring between a nematic and the particles: rigid coupling occurs when $w_{BR} \gg 1$ and soft coupling when $w_{BR} \leqslant 1$. In the case of rigid coupling, the Brochard-de Gennes theory is valid. In the case of soft anchoring, the surface anchoring energy overcomes the energy of nematic distortions and determines the interaction between the particles and the nematic host. Burylov and Raikher have derived the following equation for the effective coupling energy density between a nematic director, $\boldsymbol{n}$, and a single ferroparticle with magnetic moment along the unit vector $\boldsymbol{m}$ [5]:

$$f_{coup} = Av\frac{W_s}{d}(\boldsymbol{n}\cdot\boldsymbol{m})^2, \tag{6.2}$$

where v and d are the ferroparticle volume and diameter, respectively. Parameter A depends on the equilibrium orientation between $\boldsymbol{n}$ and $\boldsymbol{m}$: $A = 1$ when $\boldsymbol{m} \perp \boldsymbol{n}$ and $A = -2$ when $\boldsymbol{m} \parallel \boldsymbol{n}$.

These authors also studied the collective response of ferronematic suspensions to an external magnetic field [2, 3]. They derived the free energy functional of a ferronematic cell and, using it, predicted and analysed some effects in ferronematic behaviour. The main concepts of Burylov-Raikher theory are summarized here.

In their continuum theory, a ferronematic system can be described by two vector fields: the nematic director $\boldsymbol{n}(\boldsymbol{r})$, and the normalized magnetization (often called the magnetic director) $\boldsymbol{m}(\boldsymbol{r})$, and also by the scalar field of ferroparticle volume concentration $f(\boldsymbol{r})$. The free energy functional of ferronematic systems consists of the following terms:

$$\mathcal{F}^{BR} = \int_V \frac{1}{2}\left[K_1(\boldsymbol{\nabla}\cdot\boldsymbol{n})^2 + K_2(\boldsymbol{n}\cdot\boldsymbol{\nabla}\times\boldsymbol{n})^2 + K_3(\boldsymbol{n}\times\boldsymbol{\nabla}\times\boldsymbol{n})^2\right] - \frac{1}{2}\chi_a(\boldsymbol{n}\cdot\boldsymbol{H})^2 + \frac{k_bT}{v}f\ln f - fM_s(\boldsymbol{m}\cdot\boldsymbol{H}) + Af\frac{W_s}{d}(\boldsymbol{n}\cdot\boldsymbol{m})^2\ dV, \tag{6.3}$$

where $K_{1,2,3}$ are the elastic constants, χ_a is the nematic diamagnetic anisotropy, M_s is the ferroparticle volume magnetization, T is the temperature. The first two terms in Equation (6.3) are the elastic deformation energy and the magnetic energy of the nematic matrix. The next two terms are the magnetic energy of ferroparticles and the entropy of particle solution, respectively. The last term is the coupling energy obtained from Equation (6.2) by averaging over the sample volume.

By minimizing the free energy (6.3) with respect to $\boldsymbol{m}$, Burylov and Raikher found the following equation (see Equations (31)-(32) in [2]):

$$\begin{aligned}(\boldsymbol{m}\times\boldsymbol{H}_e) &= 0,\\ \boldsymbol{H}_e &= \boldsymbol{H} - \frac{2AW_s}{M_sd}(\boldsymbol{n}\cdot\boldsymbol{m})\boldsymbol{n}.\end{aligned} \tag{6.4}$$

It shows that the equilibrium particle orientation depends on the external magnetic field $\boldsymbol{H}$ and on the internal field, parallel to the director, that is arisen due to the nematic-magnetic coupling. This formula is called the bonding equation. At a given $\boldsymbol{H}$, it couples the equilibrium orientations of nematic and magnetic directors ($\boldsymbol{n}$ and $\boldsymbol{m}$) at each point of the sample volume.

Another important feature, described in [2], is a segregation effect [1, 8, 9]. This involves the re-distribution of magnetic colloidal particles in the ferronematic bulk. Typically, nanoparticles move towards the centre of the sample, where the nematic director is most free to rotate. In the theory, the following formula for the equilibrium distribution of the ferroparticle concentration is obtained by minimizing the free energy (6.3) with respect to f (see Equation (33) in [2]):

$$f = f_0\exp\left[\frac{M_sv}{k_bT}(\boldsymbol{m}\cdot\boldsymbol{H}) - \frac{aW_sv}{dk_bT}(\boldsymbol{n}\cdot\boldsymbol{m})^2\right], \tag{6.5}$$

where the constant f_0 depends on the total amount of ferroparticles in the suspension.

It should be mentioned that both effects of the nematic diamagnetism (the second term in Equation (6.3)) and the particle ferromagnetism (the fourth term)

are included in the Burylov-Raikher free energy functional. However, during the analysis of ferronematic response to a magnetic field, the authors assumed that the nematic diamagnetism was negligible. While solving the equations to predict the ferronematics behaviour in [3], they omitted the corresponding term in the free energy. Because of this assumption, the Burylov-Raikher theory was only able to describe the ferronematic response for small magnetic fields, below the Frederiks threshold field in the undoped nematic. In this small field region, the ferronematic response to the magnetic field was predicted to be linear and to be without a threshold.

Following early experimental reports [10, 11], Burylov and Raikher also studied the electric-field-induced Frederiks transition in a ferronematic cell, when the cell was exposed to both magnetic and electric fields in different geometries. In this case, they predicted a shift in the threshold electric field that depended on the strength of the bias magnetic field applied to the cell, and the coupling between the nematic and the ferroparticles. However, such geometries are not considered in this thesis, so the details of the work are omitted here. They can be found in [3].

6.1.2 Analysis of ferronematic response in Zadorozhnii model

Based on the Burylov-Raikher free energy functional (6.3), the following numerical model of ferronematics was developed by Zadorozhnii *et al.* [4, 12, 13]. The model analysed the equilibrium distributions of nematic, $\boldsymbol{n}$, and magnetic, $\boldsymbol{m}$, directors depending on the magnetic field strength, which were found by a numerical minimization of the free energy functional. Cells with two different geometries were considered in the model: a planar nematic cell with the parallel equilibrium orientation between $\boldsymbol{n}$ and $\boldsymbol{m}$ and a homeotropic cell with orthogonal alignment between $\boldsymbol{n}$ and $\boldsymbol{m}$. In both geometries, the magnetic field was applied perpendicular to the cells. These authors also made an asymptotic analysis and derived analytical equations that described the system behaviour using the small angle approximation method. Using the asymptotic calculations, they made a comprehensive study of the ferronematic response to a magnetic field depending on different system parameters, in particular, on the effective nematic-magnetic coupling strength [4]. The main results predicted by this model are presented here.

In the Zadorozhnii theory, the nematic and magnetic directors are described by the angles θ_0 and ψ_0 of their deviations from the initial orientations at the centre

of the cell. The authors introduced dimensionless parameters that scaled different effects on the system. The coupling effect is defined by the following coupling parameter:

$$\omega = \frac{fW_pD^2}{K}, \tag{6.6}$$

which scales the coupling energy to the deformation energy of the whole nematic matrix. In this equation W_p is an effective coupling energy per unit volume of ferroparticles, D is the cell thickness. A dimensionless temperature t is defined as a ratio between the entropy of the colloidal particles and the nematic elastic energy (between the fourth and the first terms in Equation (6.3)):

$$t = \frac{k_bTfD^2}{vK}, \tag{6.7}$$

This parameter controls the segregation effect. The non-segregated case and the highly segregated case correspond to $t \gg 1$ and to $t < 1$, respectively. A dimensionless magnetic field ρ measures the ferroparticle-magnetic interaction:

$$\rho = \frac{fM_sHD^2}{K}. \tag{6.8}$$

Figure 6.1 summarizes the main results of Zadorozhnii *et al.* [4] presented in terms of the predicted nematic distortion angle depending on the dimensionless magnetic field. At a low magnetic field there is a thresholdless switching of the nematic director, which is consistent with the Burylov-Raikher theory. However, a new feature predicted by the model at higher fields is that there are three distinct regimes for the ferronematic response, depending on the coupling parameter ω (see Figure 6.1). In the low coupling regime, when $\omega \leqslant \omega_c = \pi^2/2$, there is an inverse Frederiks effect: the nematic reorientation increases with field, then reaches a maximum and finally reduces to zero. The nematic distortion disappears at the critical magnetic field $\rho_c = 2\omega\omega_c/(\omega_c - \omega)$, which has been found by the asymptotic analysis. Magnetic particles, at the same time, become completely aligned with the magnetic field. It the intermediate coupling regime, which correspond to $\omega_c < \omega \leqslant 3\omega_c/2$, the nematic orientation also has a maximum and then reduces at higher fields but always remains above zero. It the high coupling regime, however, the nematic orientation increases over the whole field range, saturating at high fields.

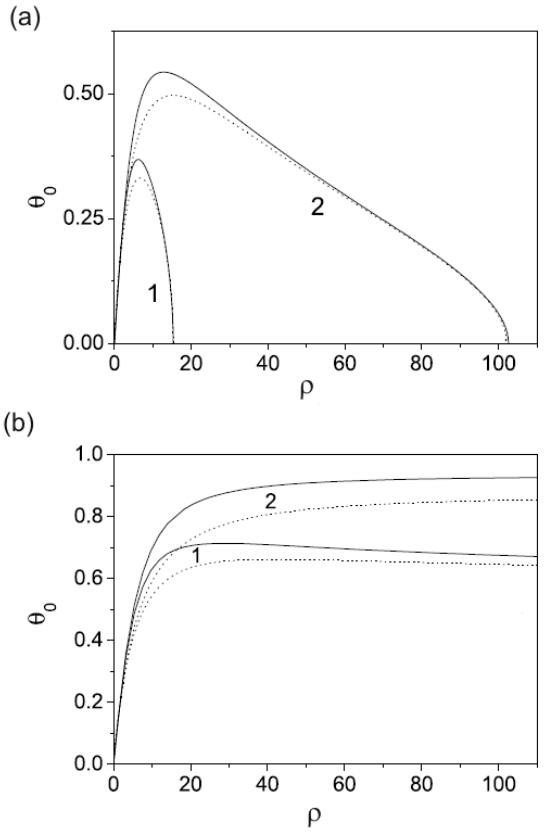

FIGURE 6.1: Nematic director distortion in the middle of the cell as a function of the dimensionless magnetic field depending on the coupling regime. (a) Weak coupling regime: curve 1 corresponds to ω=3 (curve 1) and curve 2 to ω=4.5 (curve 2). (b) Intermediate (curve 1 with ω=6) and strong (curve 2 with ω=8) coupling regimes. Solid and dotted lines show comparison between the results of numerical and asymptotic calculations; figures are taken from [4].

Using the expansion method for small angles, the authors derived analytical expressions for the nematic and magnetic director orientations around the critical magnetic field for inverse Frederiks transitions. Analyzing the segregation effect, they pointed out another interesting result; that when the segregation effect is high enough, it may cause the inverse Frederiks transition to be a first order transition, leading to bistability in the decay part of the response curve.

It should be mentioned that the assumption of a negligibly small diamagnetic effect, made by Burylov and Raikher, is also held in the Zadorozhnii model. Thus, all effects predicted by the model should occur in the ferronematic cell at magnetic field strengths below the Frederiks threshold, where the undoped nematic does not show any response. In this model, the classical Frederiks threshold corresponds to infinitely large dimensionless field limit, $\rho \to \infty$. The model can not describe the ferronematic response at magnetic fields close to and above the Frederiks threshold field in undoped nematic.

6.2 Direct and indirect effects of a magnetic field

Here, a new approach for modelling ferronematic systems is suggested. The proposed model aims to describe the ferronematic behaviour over the whole range of magnetic fields. It is designed to model the optical response in the experimental ferronematic cells discussed in Chapter 5. As will be shown in this section, in order to modify the existing theory and develop a realistic numerical model, both effects of the particle ferromagnetism and nematic diamagnetism should be taken into account. Let us first consider the impact of each of these magnetic effects on the ferronematic response.

The suggested numerical model for a ferronematic cell in an external magnetic field is based on the free energy functional that has a form similar to the free energy functional from the Burylov-Raikher theory (see Equation (6.3)):

$$\mathcal{F}_{FN} = \int_V \frac{1}{2}\left[K_1(\boldsymbol{\nabla}\cdot\boldsymbol{n})^2 + K_2(\boldsymbol{n}\cdot\boldsymbol{\nabla}\times\boldsymbol{n})^2 + K_3(\boldsymbol{n}\times\boldsymbol{\nabla}\times\boldsymbol{n})^2\right] - \frac{1}{2}\chi_a(\boldsymbol{n}\cdot\boldsymbol{H})^2 - fM_s(\boldsymbol{m}\cdot\boldsymbol{H}) - f\Omega(\boldsymbol{n}\cdot\boldsymbol{m})^2\, dV, \tag{6.9}$$

Let us recall again that the first and second terms are the elastic and the magnetic energies of the nematic matrix, the third term is the magnetic energy of colloidal particles and the last term is the coupling energy. Parameter Ω is the effective coupling energy density, per unit nanoparticle volume, associated with orientational alignment between the ferroparticles and liquid crystal director. It corresponds to the parameter W_p from the Zadorozhnii model [12]. If the coupling is assumed to be an effect of the nematic anchoring with the surface of ferroparticles (as was assumed in the Burylov-Raikher theory [2]), then an effective surface anchoring energy W_s can be defined as:

$$W_s = \Omega d, \tag{6.10}$$

where d is the particle size.

The following assumptions are made in this new model. Firstly, the effect of local re-distribution of colloidal particles - the segregation effect - and the effect of particle aggregations are both neglected. It is assumed that the particles are uniformly distributed within the sample bulk. That is why, by contrast with Equation (6.3), the entropy of the particle solution (the third term) is omitted in Equation (6.9). Secondly, the dipole-dipole interaction between neghbouring nanoparticles is neglected. Energy associated with this interaction is proportional

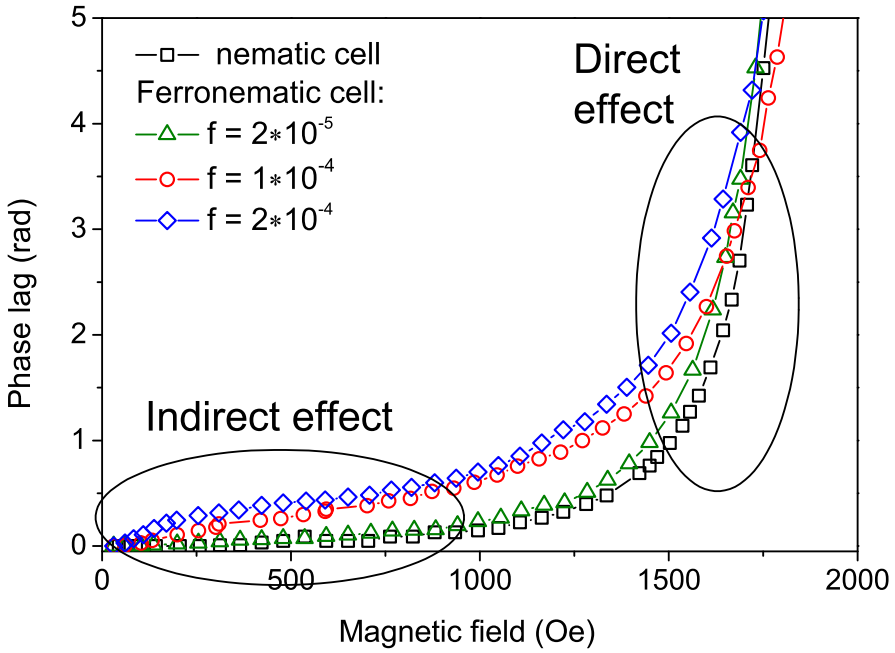

FIGURE 6.2: Experimentally measured response of a nematic cell and ferronematic cells with different particle volume fractions, with respect to the external magnetic field.

to: $\frac{1}{r_{ij}^3}(\boldsymbol{m}_i \cdot \boldsymbol{m}_i) - \frac{3}{r_{ij}^5}(\boldsymbol{m}_i \cdot \boldsymbol{r}_{ij})(\boldsymbol{m}_j \cdot \boldsymbol{r}_{ij})$, where $\boldsymbol{r}_{ij}$ is the vector between two dipoles $\boldsymbol{m}_i$ and $\boldsymbol{m}_j$. Volume concentrations of magnetic inclusions in the experimental suspensions are small, $f \sim 10^{-5} - 10^{-4}$, which correspond to large inter-particle distances, of the order of 10 to 50 times the particle size. Because of this, the energy between two neighbouring particles becomes negligibly small.

The effect of particle aggregation is also neglected in the model. In fact, the model deals with an average continuum distribution of magnetic inclusions rather than a set of separate particles. In this sense, a cluster of multiple particles is equivalent to a single particle of a large size. So, the model should describe a partly aggregated suspension. This approximation however is valid for suspensions containing only particle clusters of small size, at which they can not significantly disturb the nematic director around them. The effect of local nematic distortions around particles is not taken into account here.

An external magnetic field can influence the nematic host of ferronematic composites by two distinct effects, one of which associated with the diamagnetic nature of the nematic, and the other with the ferromagnetic properties of the colloidal inclusions. These effects will be called the direct and the indirect effects, respectively. The direct effect of the magnetic field is caused by the diamagnetic anisotropy of

nematic molecules. It is described by the magnetic energy of the nematics, which is the second term in the free energy functional (6.9). This term is a quadratic in the magnetic field $\boldsymbol{H}$, which leads to the threshold behaviour of the nematic director response to the field. Considering the experimental data (see Figure 6.2 above), the direct effect dominates the ferronematic behaviour at a field strength close to the Frederiks threshold value in the undoped nematic. It is worth mentioning that only the direct effect causes the magneto-optic response in the undoped nematic cell.

The indirect effect is associated with the presence of ferromagnetic inclusions in a ferronematic mixture. An applied magnetic field tends to align ferroparticle magnetic moments along its direction; this effect is modelled by the magnetic energy of ferroparticles (the third term) in the free energy functional (6.9). The effect of particle rotations is transferred to the liquid crystal matrix as a result of the magnetic-nematic coupling, which is described by the coupling energy (the fourth term) in the free energy functional. The indirect effect is linear in the field $\boldsymbol{H}$. This leads to a linear, thresholdless magneto-optic response at a small field in the experimental ferrosuspensions, as indicated in Figure 6.2.

The direct effect of the magnetic field on ferronematic systems was neglected in the previous theoretical studies of Burylov and Raikher [2, 3] and in the following Zadorozhnii model [4, 12, 13]. Even though the nematic magnetic energy term was included in the Burylov-Raikher theory, they omitted it during the modelling of nematic reorientation in the magnetic field. The resulting calculations might be regarded as applicable in the low external magnetic field limit, but in the very strong indirect coupling regime. In the low field limit, indeed, the direct effect is always small as a result of the low liquid crystal diamagnetic anisotropy. However, the experimental data included here do not correspond to this limit. Although there is the linear ferronematic response to a low magnetic field (see Figure 6.2), the principal reorientation is observed at fields close to the effective Frederiks threshold. This is not predicted by previous theories. Experimental data indicate that the direct effect is rather dominant and that the magnetic field-induced reorientation is only perturbed by the presence of the colloidal particles. In order to overcome this problem, the direct effect is specifically included in the present model and assumed as dominant. The experimental ferronematic colloids can be called as "weak ferronematic" systems. It is worth noting that, in principle, the model can also treat the limit at which the indirect effect dominates ("strong ferronematic" systems).

6.3 Numerical model of ferronematics

The present model considers a cell with ferronematic suspension in an external magnetic field. The geometry of the system corresponds to the magneto-optic experiment (see Section 3.3). The ferronematic cell of thickness D has planar liquid crystal alignment with a small pretilt angle, α, and a rigid anchoring on the cell substrates. The nematic host is described by the nematic director $\boldsymbol{n}$, and the ferromagnetic inclusions are modelled by the magnetic director $\boldsymbol{m}$. The cell is assumed to be uniform in two in-cell-plane directions, so that the nematic and magnetic directors depend on the z coordinate only. These quantities are characterised respectively by the angles $\theta(z)$ and $\psi(z)$ as depicted in Figure 6.3. The external magnetic field is applied in two directions: the test magnetic field $\boldsymbol{H}$ with a varying strength is applied in the z direction, and a small constant bias field $\boldsymbol{H}_b$ is applied in the x direction. In this geometry:

$$\boldsymbol{n} = (\cos\theta,\ 0,\ \sin\theta), \tag{6.11a}$$

$$\boldsymbol{m} = (\cos\psi,\ 0,\ \sin\psi), \tag{6.11b}$$

$$\boldsymbol{H} = (H_b,\ 0,\ H). \tag{6.11c}$$

The model deals with the dimensionless free energy of the system, F_{FN}. It is possible to scale energy with respect to the thermal energy (k_bT), as was suggested in the Burylov-Raikher theory. In this model, however, we neglect the temperature dependent segregation effect. That way it is more convenient to follow the notation from the Zadorozhnii model, where the dimensionless free energy is scaled with respect to the elastic properties of the liquid crystal matrix: $F_{FN} = \mathcal{F}_{FN}D/(K_1S_0)$, where S_0 is the area of the cell. A dimensionless coordinate z ($0 < z < 1$) is also introduced. It is scaled with respect to the cell thickness D.

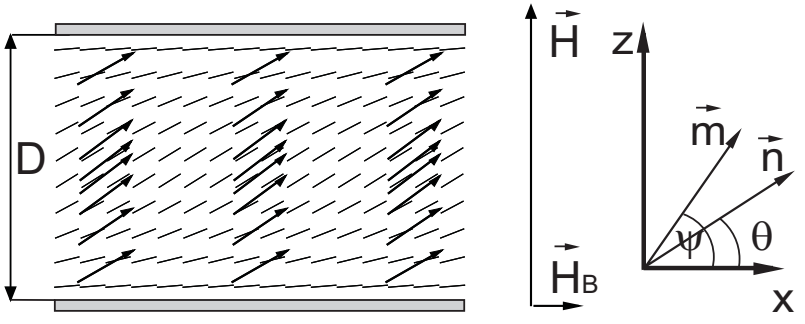

FIGURE 6.3: Geometry of the ferronematic cell.

There are different alternatives for scaling the test magnetic field. In the Zadorozhnii theory, the dimensionless magnetic field ρ (see Equation (6.8)) measures the magnetic energy of the ferroparticles. This notation was suitable for their model because the corresponding contribution to the system free energy was assumed to be dominant. But this is not the case in the present model. As was shown above, the contribution from the ferromagnetic effect is suspected to be rather a perturbation to the standard nematic model. Because of this, another scaling of the magnetic field is introduced: a dimensionless parameter for the test field, h, and another parameter for the bias field, b. These dimensionless magnetic fields are defined in the same way as in the nematic model: $h = H/H_s$, $b = H_b/H_s$, where $H_s = D^{-1}\sqrt{K_1/\chi_a}$ (see Equation (4.5)). This scaling is also convenient for comparison between the nematic and ferronematic models. It means that the classical Frederiks threshold occurs at a dimensionless field of $h = \pi$.

The following dimensionless parameters are also introduced in the model:

$$\kappa = \frac{M_s f D}{\sqrt{\chi_a K_1}}, \tag{6.12a}$$

$$\omega = \frac{\Omega f D^2}{K_1}. \tag{6.12b}$$

These parameters contain all the characteristics of the ferromagnetic colloidal inclusions. The *magnetic parameter* κ, which depends on the particles magnetization M_s, characterises the ratio of the magnetic field effect associated with ferroparticles to the direct coupling of the magnetic field with the nematic matrix. Thus, $\kappa < 1$ and $\kappa > 1$ correspond respectively to the direct or indirect effects dominating the magnetic properties of the ferronematic suspension. The *coupling parameter* ω is introduced in the same way as in the Zadorozhnii model (see Equation (6.6)). It measures the coupling energy between ferroparticle and nematic orientations scaled to the liquid crystal elastic deformation energy.

The dimensionless free energy functional (6.9) in the present geometry and with the dimensional parameters reduces to:

$$F_{FN} = \int_0^1 \frac{1}{2}\left(\frac{d\theta}{dz}\right)^2 [1 + p\sin^2\theta] - \frac{1}{2}\left[h\sin\theta + b\cos\theta\right]^2 - \kappa\left[h\sin\psi + b\cos\psi\right] - \omega\cos^2(\psi - \theta)\, dz. \tag{6.13}$$

From the mathematical point of view, the free energy (6.13) is a functional that depends on two variable functions: nematic orientation $\theta(z)$ and magnetic orientation $\psi(z)$. Minimization of this functional yields the following Euler-Lagrange equations:

$$\frac{d^2\theta}{dz^2}\left[1+p\sin^2\theta\right]+\frac{p}{2}\left(\frac{d\theta}{dz}\right)^2\sin 2\theta+\frac{h^2-b^2}{2}\sin 2\theta$$
$$+hb\cos 2\theta+\omega\sin 2(\psi-\theta)=0, \tag{6.14a}$$
$$\kappa(h\cos\psi-b\sin\psi)-\omega\sin 2(\psi-\theta)=0. \tag{6.14b}$$

The second equation is the bonding equation (see Equation (6.4)), which couples the nematic and magnetic orientations in each point of the cell and at given magnetic fields h and b.

The case with undoped nematic corresponds to $\kappa=\omega=0$. In this case the system of Equations (6.14a) and (6.14b) decouples. Equation (6.14b) is identically satisfied, and Equation (6.14a) reduces to the corresponding Euler-Lagrange equation from the nematic model (4.7). In the case of non-magnetic colloidal inclusions $\kappa\to 0$, but $\omega\neq 0$. Then, Equation (6.14b) has a solution $\theta=\psi$, and the nematic alignment is again described by Equation (4.7). When particles are magnetic but do not interact with a liquid crystal, $\omega\to 0$, $\kappa\neq 0$, they become completely aligned by the magnetic field: $\tan\psi=h/b$. The nematic host again behaves in the same way as the undoped nematic.

In the general case, when $\kappa\neq 0$ and $\omega\neq 0$, the system of Equations (6.14a) and (6.14b) does not have analytical solutions. So, it is solved numerically using the method of successive iterations. The solution of the first equation (6.14a) is found using the Broyden method [14], coupled with the spectral methods for determining the derivatives over the spatial coordinate [15] (details of these methods are presented in Appendix A). The second bonding equation (6.14b) is solved with respect to the unknown variable $\psi(z)$, yielding the magnetic director profile at a given nematic director and magnetic field strengths. Fixed boundary conditions are imposed for the nematic orientation function: $\theta(z=0,z=1)=\alpha$, while the boundary conditions for $\psi(z)$ are found from the bounding equation at each value of h and b, separately. The numerical solution of Equations (6.14a) and (6.14b) is computed by the specifically modified MATLAB code from the nematic mode. The code yields nematic, $\theta(z)$, and magnetic, $\psi(z)$, director profiles inside the cell as a function of the test magnetic field, for the given coupling and magnetic parameters, as well as liquid crystal characteristics and cell parameters.

At the next step of the model, the nematic director orientation angle $\theta(z)$ is used to calculate the optical response from the cell. The phase lag between the ordinary and extraordinary components of a beam induced by the nematic layer, $\Delta\delta$, and the corresponding intensity of the beam after the cell, $I_\perp$, are calculated in the same way as in the nematic model (see Section 4.1 for details). The numerical results calculated by the model can now be compared with the experimental dependences of the phase lag $\Delta\delta$ and the cross-polarized intensity $I_\perp$ on the test magnetic field magnitude, measured from different ferronematic suspensions that are described in Chapter 5.

6.4 Fitting the experimentally measured ferronematic response

In this section the numerical model of ferronematics is used to fit the experimental magneto-optic data measured in the cells, with the two different ferronematic suspensions that were discussed in Chapter 5. Firstly, this helps to verify the numerical model, but also a further analysis of the experimental ferrosuspension can be carried out, including an estimation of the effective coupling energy between the particles and the nematic host, from the values of the fitting parameters.

The fitting procedure is very similar to the one described in Section 4.1.1. A set of numerically calculated functions of the nematic director orientation $\theta(z)$ for different values of the magnetic field strength H is used to calculate the dependence of the cross-polarized intensity $\boldsymbol{I}_\perp(H)$, which is then compared with the experimental cross-polarized intensity curve. The only extra fitting parameters for the ferronematic cells are the magnetic and coupling parameters κ and ω. All other parameters are either known from the previous measurements or taken from the literature. The cell thickness is obtained from the zero field cross-polarized intensity, $I_\perp(H = 0)$, in the same way as with the undoped nematic. The nematic diamagnetic anisotropy χ_a, the elastic constants K_1 and K_3, and the refractive indices n_o and n_e, following the conclusions from the previous chapter, are assumed not to differ from that of the undoped liquid crystal. The value of $\chi_a = 1.22 \times 10^{-7}$ is taken from the fitting of the undoped E7 cell, K_1, K_3, n_o, and n_e are taken from the literature (see Table 3.1). The values of a pretilt angle $\alpha = 2.7^\circ$ and a bias field $H_b = 16$ Oe are taken from direct measurements (see Chapter 3).

The fitting procedure, at first, is applied to the magneto-optic data measured in the cells with spherical magnetic nanoparticles. After that, the same procedure is applied to the suspensions doped with the magnetite nanorods.

6.4.1 Data from the spherical magnetic nanoparticle suspensions

The cross-polarized intensity data measured from Fe_xO_y nanoparticle-doped cells were discussed in Section 5.2.1 (see Figure 5.3). They can be further analysed using the numerical model of ferronematics. For convenience, the following labels will be used for the cells with different concentration suspensions: sample A is a cell with the ferroparticle volume fraction $f = 2 \times 10^{-5}$, sample B is a cell with $f = 1 \times 10^{-4}$, and sample C is a cell with $f = 2 \times 10^{-4}$.

The comparison between an experimental cross-polarized intensity and a fitting curve for sample A is presented in Figure 6.4. This figure shows a good agreement between the theory and experiment over the whole range of the magnetic field. The optimal fit is obtained for the magnetic and coupling parameters $\kappa = 0.08,\ \omega = 0.07$. The parameter of the fit quality, r, defined by Equation (4.10) in Section 4.1.1, for this sample is 0.013; a value which is compatible with the value for the undoped E7 (see Table 6.1).

In sample B, it is also possible to obtain a good fit between the theoretical model and experiment, but this agreement holds only at low and intermediate magnetic fields. These fit results, shown in Figure 6.5, are obtained with the ferronematic parameters $\kappa = 0.31,\ \omega = 0.30$. The experimental and theoretical curves diverge at a field above 1800 Oersted. In particular, the model predicts a set of oscillations of the normalized intensity $I_\perp$ which pass through zero and unity. On the other hand, the maxima in the experimental data oscillations reach only about 0.5. This trend is also confirmed in sample C, see Figure 6.6. The model can predict the general behaviour of the system and give the reasonable fitting parameters: $\kappa \approx 0.5$ and $\omega \approx 0.4$. However, the oscillations exhibit a reduced amplitude at high fields and the fit at lower fields is not as good. This also can be seen from the increase in the parameter r (see Table 6.1).

The reduction in the amplitude of the intensity oscillations is probably connected with particle aggregations as was discussed in Section 5.2.2. Local distortions of the nematic director are expected to be around large aggregates, which might cause

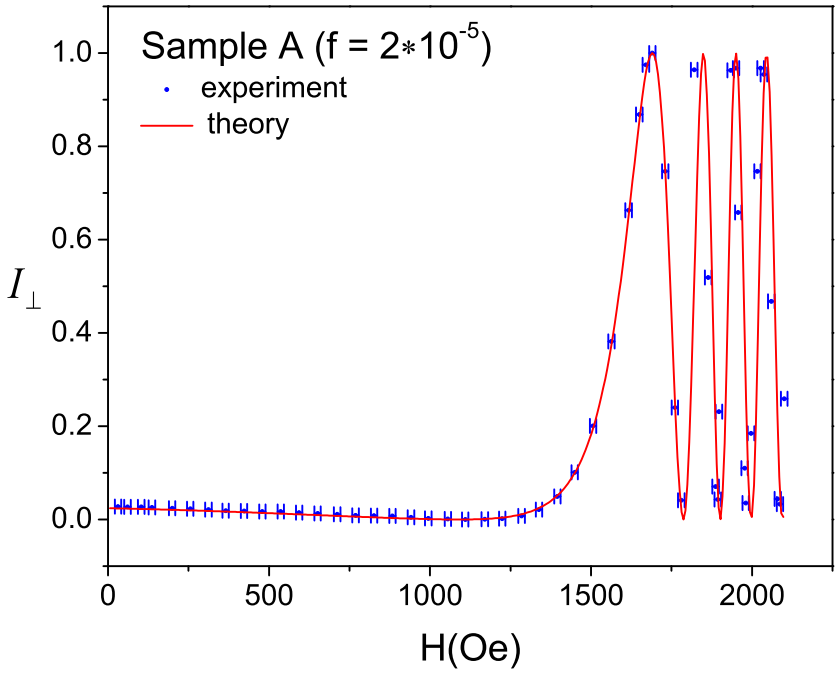

FIGURE 6.4: Sample A, $f = 2 \times 10^{-5}$: optimal model predictions (solid line) and experimental values (dots with error bars) for the cross-polarized intensity $I_\perp$. Note the good agreement between model and experiment, even up to high magnetic fields

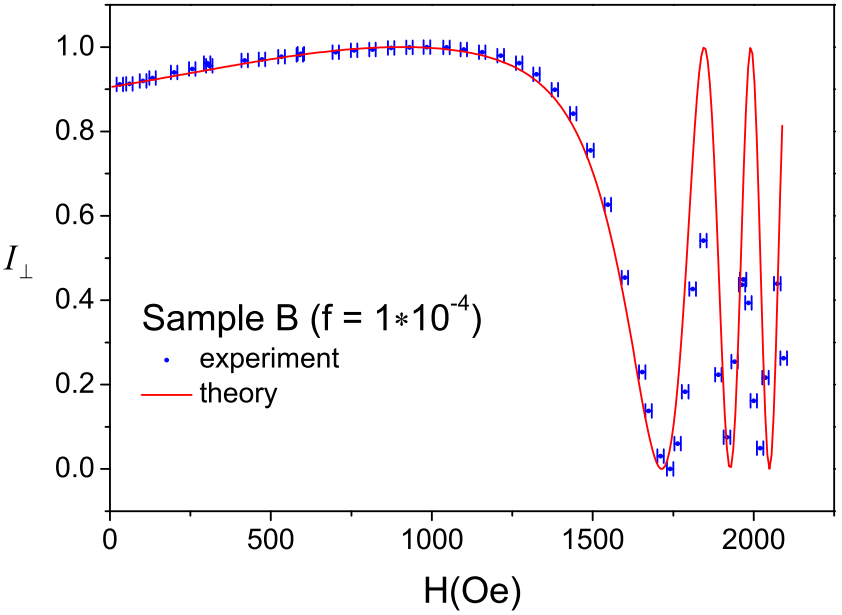

FIGURE 6.5: Sample B, $f = 1 \times 10^{-4}$: optimal model predictions (solid line) and experimental values (dots with error bars) for the cross-polarized intensity $I_\perp$. Note the good agreement between model and experiment only up to magnetic fields $\sim$ 1800 Oersted

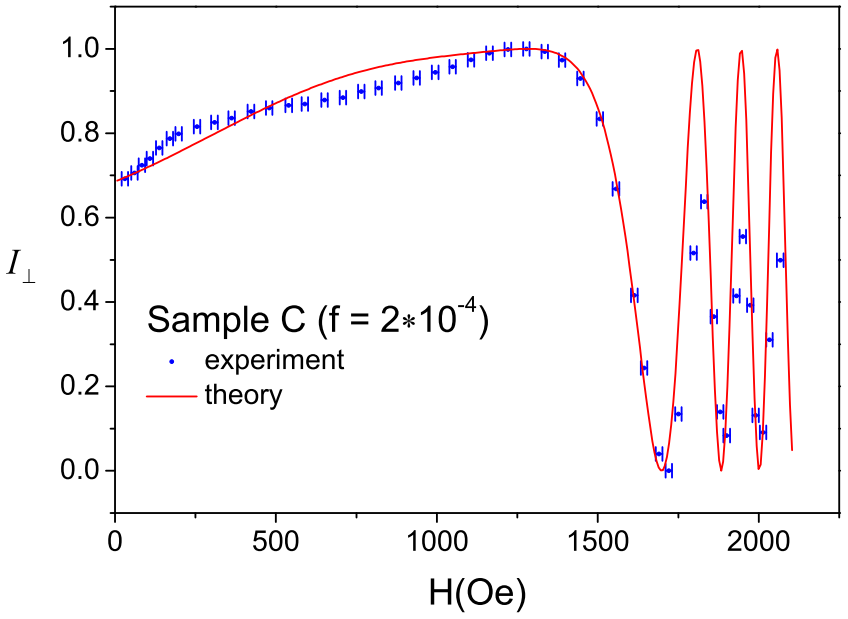

FIGURE 6.6: Sample C, $f = 2\times10^{-4}$: optimal model predictions (solid line) and experimental values (dots with error bars) for the cross-polarized intensity $I_\perp$. Note the only moderate agreement between the optimal model and experimental curves, with poorer fits occurring both in the low field and high field regimes.

TABLE 6.1: Values of magnetic, κ, and coupling, ω, parameters obtained from fitting the experimental data, and an estimate of coupling energy for different samples of ferronematic suspensions.

Suspension	f	r	κ	ω	ω/κ	Ω, erg cm^{-3}
Undoped E7	0	0.014	n/a	n/a	n/a	n/a
FN sample A	2×10^{-5}	0.013	0.08	0.07	0.875	3.9×10^4
FN sample B	1×10^{-4}	0.075	0.31	0.30	0.967	4.7×10^4
FN sample C	2×10^{-4}	0.054	0.5	0.4	0.8	3.8×10^4

scattering and depolarization of light, leading to a reduced intensity amplitude. In the model, however, this process is not taken into account and a uniform nematic orientation over the whole range of magnetic fields is assumed. So, the model does not predict a reduced intensity amplitude.

The fitting parameters for all suspensions are presented in Table 6.1. It can be seen that the coupling and magnetic parameters for sample B are approximately four times larger than those for sample A. This is roughly consistent with the difference in the particle concentrations in these suspensions, as κ and ω are predicted to be proportional to f (see Equations (6.12a), (6.12b) from Section 6.3). However, this proportionality no longer holds for the higher concentration sample C. This might

indicate the effect of particle aggregation in the suspensions. In the aggregates, the magnetic moment of a particle is compensated by that of the neighbouring particles, so the average magnetization of the suspensions becomes smaller. This means that in partly aggregated suspensions the effective particle content, which defines the ferronematic response, is smaller than the total amount of particles.

Based on Equations (6.12a), (6.12b), the ratio between the coupling and magnetic parameters, ω/κ, should be independent of the particles concentration. Thus, this ratio should be the same for all suspension regardless the level of aggregation. As expected, these ratios for all suspensions (see Table 6.1) do not differ significantly, even in spite of the lack of fit for the suspension of highest concentration.

The ratio ω/κ can be used to evaluate the effective coupling energy density between the nematic and magnetic orientations:

$$\Omega = \frac{M_s}{D}\frac{\omega}{\kappa}\left(\frac{K_1}{\chi_a}\right)^{1/2}, \tag{6.15}$$

where the nematic elastic constant, K_1, is taken from Table 3.1, the cell thickness D and the diamagnetic anisotropy χ_a are taken from the fit, and the particle magnetization are know from the data sheet, $M_s = 75$ emu cm^{-3}. The values of Ω obtained from different samples are also listed in Table 6.1. The average value is $\Omega = (4 \pm 0.4) \times 10^4$ erg cm^{-3}.

The Burylov-Raikher theory [6, 16] refers to the effective surface anchoring energy at the surface of a ferroparticle: $W_s = \Omega d$ (see Equation (6.10)), where d is the typical dimension of a colloidal nanoparticle. Substituting $d = 20$ nm, our nanoparticle suspension is characterised by $W_s \approx 8 \times 10^{-2}$ erg cm^{-2}. This quantity is of the same order of magnitude as that estimated by Kopčanský *et al.* for small (~ 10 nm) spherical nanoparticles coated with Oleic acid [17].

To check the suspension stability, the Frederiks transition experiment in magnetic field was repeated after a six month interval using the same samples (see Section 5.2.2). This time the measurements for each sample were performed twice, with two different directions of the bias field: forward and backward (see Section 4.2 for definition). An example of the repeated experimental data for sample B is presented in Figure 6.7 (dots). The significant difference between the data collected at different directions of the bias field again proves the conclusions from Chapter 4. It shows that the bias field does not only initially align nanoparticles,

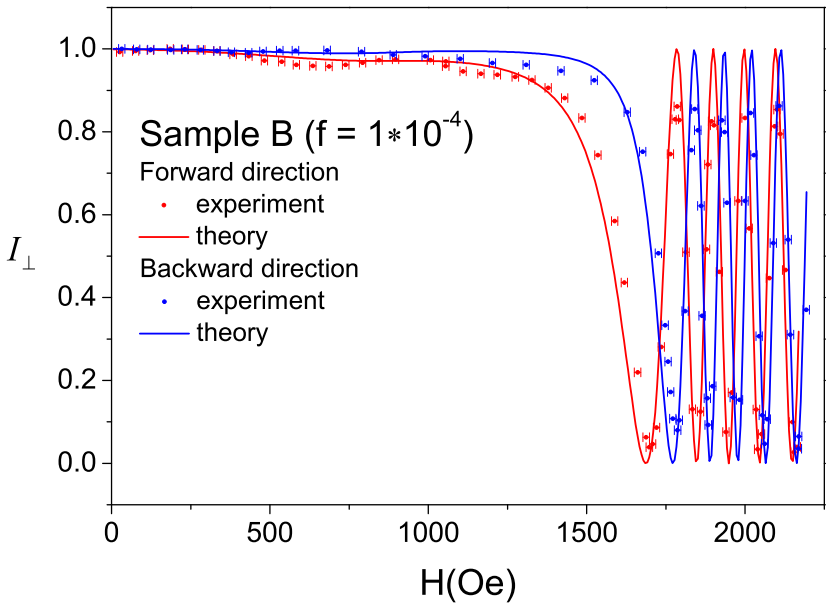

FIGURE 6.7: Sample B, $f = 1 \times 10^{-4}$: repeated measurements of the cross-polarized intensity $I_\perp$ (dots with error bars) and optimal fit (solid line). Two sets of data (marked by red and blue colour) correspond to experiments with different directions of bias magnetic field.

TABLE 6.2: Values of magnetic, κ, and coupling, ω, parameters obtained from fitting the repeated measurements of different ferronematic suspensions, and an estimate of coupling energy for different samples.

Suspension	f	r	κ	ω	ω/κ	Ω, erg cm^{-3}
FN sample A	2×10^{-5}	0.026	0.10	0.07	0.7	$3.2{\times}10^4$
FN sample B	1×10^{-4}	0.016	0.32	0.22	0.688	$3.3{\times}10^4$
FN sample C	2×10^{-4}	0.041	0.36	0.28	0.778	$3.7{\times}10^4$

but that it can also cause a shift of the effective Frederiks threshold. So, it is important to keep the same orientation of the bias field during the experiment with different cells for their further comparison later. The bias field is also included into the model, enabling a good fit.

The experimental data from the repeated measurements were fitted to the model. The fitting of cross-polarized intensity data for sample B are presented in Figure 6.7. Two sets of data for each sample were fitted simultaneously with the same fitting parameters. The only difference in the model between the two theoretical curves is the sign of the bias field parameter. The coupling and magnetic parameters obtained from the fitting of the repeated measurements for all samples, are listed in Table 6.2. They are also used for an estimation of the effective

coupling energy Ω for all samples.

The repeated measurements for all samples show the same general trends: the ferronematic parameters are larger in the higher concentration suspensions; the amplitude of the oscillations drops with increasing particle content. However, the curves for repeated experiments diverge from the previously measured curves for the same samples. This might be explained by supposing that further aggregation has occurred between the measurements. The coupling and magnetic parameters remain nearly the same only in the lowest concentration suspension, and fall by approximately 30% compared to the parameters from the old measurements in the highest concentration suspension. This again indicates an effect of the aggregation process, which is expected to be proportional to the concentration. However, the average value of the coupling energy $\Omega = (3.4 \pm 0.2) \times 10^4$ erg cm^{-3} changes only slightly.

6.4.2 Data from the magnetite nanorod suspension

The results of magneto-optic experiments performed with the magnetite nanorod suspension, which were discussed in Section 5.3.3, can also be analysed and fitted to the numerical model in the same way as discussed in the previous section. The experimental data obtained from a cell with the OBPh-coated magnetite nanorod suspension were plotted in Figure 5.14. The cross-polarized intensity data that correspond to the curve obtained from the second experimental run are selected for analysis in this section. These data and an optimal model fitting curve are presented in Figure 6.8. This figure demonstrates a good quality fit of the experimental data over the whole range of the magnetic field.

The fitting curve in Figure 6.8 is obtained with the following values of the fitting parameters: magnetic parameter $\kappa = 0.06$, and coupling parameter $\omega = 0.11$. The ratio between the fitting parameters ω/κ is 1.83, which is approximately two times higher than the corresponding ratio between parameters for magnetic nanoparticle suspensions. This might indicate that the coupling energy between the nanorods and nematic molecules is higher. However, it is not possible to calculate it using Equation (6.15) because the saturation magnetization of the nanorods, M_s, is unknown.

The saturation magnetization of bulk magnetite material can be obtained from the literature, $M_s = 480$ emu cm^{-3} [18, 19]. However, the saturation magnetization in small particles is usually lower than in the bulk material and depends both on the

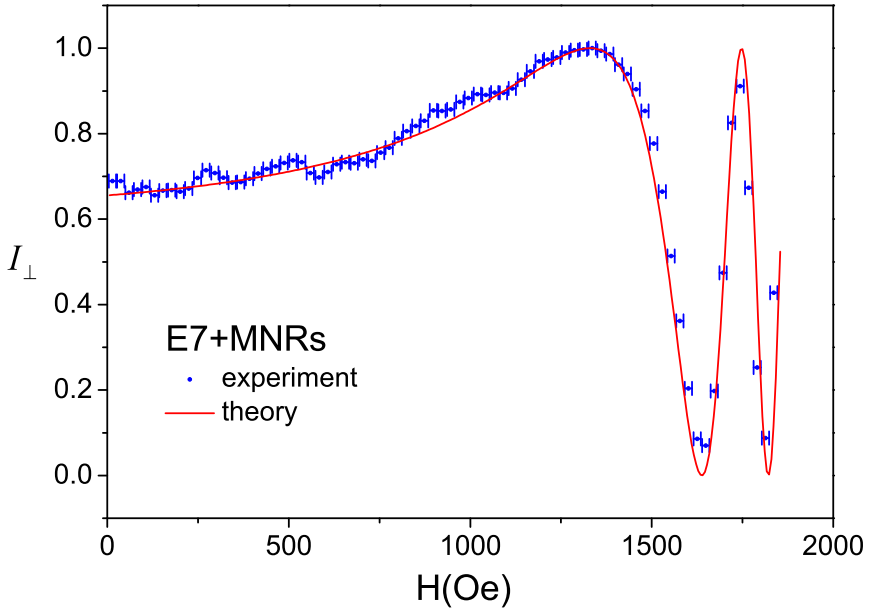

FIGURE 6.8: Magnetite nanorod suspension, $f = 3 \times 10^{-5}$: optimal model prediction (solid line) and experimental data (dots with error bars) for the cross-polarized intensity dependence $I_\perp(H)$.

particle size and on the method of synthesis [18, 19, 20]. Following Equation (6.15), Ω is directly proportional to M_s. This means that the upper bound of the coupling energy density can be estimated as $\Omega = 5.4 \times 10^5$ erg cm^{-3}. This calculation can only serve as a preliminary approximation, as it is based on a fit of only one set of experimental data. Nevertheless, it shows that the effective coupling energy between nematic E7 and the magnetite nanorods is more than one order of magnitude higher than the coupling energy with the spherical nanoparticles of iron oxide.

Summary

A numerical model that describes the magnetic-field-induced Frederiks transition in ferronematic cells has been developed in this chapter. The model is based on the free energy functional from the Burylov-Raikher continuum theory of ferronematics. However, the present model extends the theory of Burylov and Raikher. In the previous theories, the impact from nematic diamagnetism was assumed negligible as compared to the effect of particle ferromagnetism. Because of this, previous theory could only model the ferronematic response at a small magnetic field limit, far below the Frederiks threshold field in undoped nematic. In the

present theory, however, the effect of nematic diamagnetism has been taken into account. So, the model can predict the ferronematic response over the whole range of magnetic fields including small fields and high fields above the Frederiks threshold. Moreover, analysis of the experimental data from Chapter 5 suggests that this intrinsic nematic effect dominates the effect of magnetic inclusions in the experimental suspensions.

The experimental results of Frederiks transition experiments with some of the ferronematic suspensions described in Chapter 5, namely the suspensions with spherical magnetic nanoparticles and another with magnetite nanorods, have been fitted to the numerical model. The fitting procedure has allowed the determination of the magnetic and coupling parameters that give the best agreement between the model and the experimental curves. The values of these parameters, for different concentration suspensions, have permitted the evaluation of the effective coupling energy density between the nematic and magnetic orientations. This value is $(4 \pm 0.4) \times 10^4$ erg cm^{-3} in the spherical magnetic nanoparticle suspension. The estimation of the coupling energy in the case of the magnetite nanorods suggests that its value is approximately one order of magnitude higher as compared with the magnetic nanoparticles. However, despite the higher coupling energy in the magnetite nanorod suspension, the magnetic parameter κ obtained from fitting the magneto-optic curves is lower than the magnetic parameter for the spherical magnetic nanoparticle suspension with comparative concentration. This is in agreement with a lower linear response at low fields and a higher decrease in the effective Frederiks threshold observed in the magnetite nanorod suspension in comparison with the corresponding spherical nanoparticle suspension, which were presented in Chapter 5.

A good quality agreement between the theory and the experiment is obtained for the magnetite nanorod suspension. In the case of the spherical magnetic nanoparticle suspensions, the numerical model yields a good quality fit to the data obtained from the lowest concentration sample. At higher concentrations, despite some deviation between the theory and experiment, the theory still predicts the basic trend in the system. The lack of a better fit can be explained by nanoparticle aggregations in the suspensions, as this effect is not taken into account in the model. The evidence of particle aggregations has been confirmed in Chapter 5 by microscopy images and by repeating the experiment after a six month interval. The fitting parameters for the repeated data become smaller than the parameters for the original data; moreover, a larger change is observed in more concentrated samples.

References

[1] F. Brochard and P. G. de Gennes. Theory of magnetic suspensions in liquid crystal. *Journal de Physique (Paris)*, 31:691–708, 1970.

[2] S. V. Burylov and Yu. L. Raikher. Macroscopic properties of ferronematics cause by orientational interactions on the particles surface. I Extended continuum theory. *Molecular Crystals and Liquid Crystals*, 258:107–122, 1995.

[3] S. V. Burylov and Yu. L. Raikher. Macroscopic properties of ferronematics cause by orientational interactions on the particles surface. II Behavior of real ferronematics in external field. *Molecular Crystals and Liquid Crystals*, 258: 123–141, 1995.

[4] V.I. Zadorozhnii, T. J. Sluckin, V. Yu. Reshetnyak, and K.S. Thomas. The Frederiks effect and related phenomena in ferronematic materials. *SIAM Journal of Applied Mathematics*, 68(6):1688–1716, 2008.

[5] S. V. Burylov and Yu. L. Raikher. Ferronematics: on the development of the continuum theory approach. *Journal of Magnetism and Magnetic Materials*, 85:74–76, 2000.

[6] S. V. Burylov and Yu. L. Raikher. Orientation of a solid particle embedded in a monodomain nematic liquid crystal. *Physical Review E*, 50(1):358–376, 1994.

[7] S. V. Burylov and Yu. L. Raikher. On the orientation of an anisotropic particle suspended in a bulk uniform nematic. *Physics Letters A*, 149(5,6):279–283, 1990.

[8] S. B. Chernyshuk, B. I. Lev, and H. Yokoyama. Collective effects in doped nematic liquid crystals. *Journal of Experimental and Theoretical Physics*, 93, 2001.

[9] D. V. Makarov and A. N. Zakhlevnykh. Tricritical phenomena and the Freedericksz transition in ferronematic liquid crystals. *Physical Review E*, 81: 051710, 2010.

[10] S.-H. Chen and B. J. Liang. Electo-optic effect of a magnetically biased ferronematic liquid crystal. *Optics Letters*, 13(9):716–718, 1988.

[11] B. J. Liang and S.-H. Chen. Electric-field-induced molecular reorientation of a magnetically biased ferronematic liquid-crystal film. *Physical Review A*, 39:1441–1446, 1989.

[12] V. I. Zadorozhnii, A. N. Vasilev, V. Yu. Reshetnyak, K. S. Thomas, and T. J. Sluckin. Nematic director response in ferronematic cells. *Europhysics Letters*, 73(3):408–414, 2006.

[13] V.I. Zadorozhnii, V. Yu. Reshetnyak, A. V. Kleshchonok, T. J. Sluckin, , and K.S. Thomas. Inverse Frederiks effect and bistability in ferronematic cells. *Molecular Crystals and Liquid Crystals*, 475:221–231, 2007.

[14] C. G. Broyden. A class of methods for solving nonlinear simultaneous equations. *Mathematics of Computation*, 19(92):577–593, 1965.

[15] L. N. Trefethen. *Spectral Methods in Matlab*. SIAM, Philadelphia, 2000.

[16] S. V. Burylov and Yu. L. Raikher. Ferromenatics: enhanced magneto-optical response of a liquid crystalline system. *Materials Science and Engineering: C*, C2:235–241, 1995.

[17] P. Kopčanský, N. Tomašovičová, M. Koneracká, V. Závišová, M. Timko, A. Dzarova, A. Sprincova, N. Eber, K. Fodor-Csorba, T. Toth-Katona, A. Vajda, and J. Jadzyn. Structural changes in the 6CHBT liquid crystal doped with spherical, rodlike, and chainlike magnetic particles. *Physical Review E*, 78:011702, 2008.

[18] H. M. Lu, W. T. Zheng, and Q. Jiang. Saturation magnetization of ferromagnetic and ferrimagnetic nanocrystals at room temperatures. *Journal of Physics D: Applied Physics*, 40:320–325, 2007.

[19] N. Mahmed, O. Heczko, O. Söderberg, and S.-P. Hannula. Room temperature synthesis of magnetite (Fe_3-δO_4) nanoparticles by a simple reverse co-precipitation method. *IOP Conf. Series: Materials Science and Engineering*, 18:032020, 2011.

[20] H. Iida, K. Takayanagi, T. Nakanishi, and T. Osaka. Synthesis of Fe_3O_4 nanoparticles with various sizes and magnetic properties by controlled hydrolysis. *Journal of Colloid and Interface Science*, 314:274–280, 2007.

Chapter 7

Conclusions and future work

Liquid crystals are a phase of matter that occurs in some organic materials and that has properties between the liquid and crystal states. There are different mesophases; however, this thesis is only concerned with a nematic phase, in which the molecules do not have positional order, but demonstrate orientational order. As a result of the orientational order, nematics demonstrate birefringence. Additionally, nematics are characterised by anisotropy in dielectric and diamagnetic properties. This property offers the possibility of easily aligning and switching them by applying an electric or a magnetic field. However, conventional nematics have very low sensitivity to magnetic fields (their diamagnetic anisotropy is of the order of 10^{-7}). So, the magnetic threshold field for a conventional nematic cell is very high. For example, in a cell with the dimensions of a typical liquid crystal device, $5 - 50$ μm, a rather high field, of the order of 1 to 10 kOe, is required to trigger director reorientation. On the other hand, the dielectric anisotropy of nematics is relatively large, which makes the switching voltage as low as a few volts. Therefore, liquid crystals have found a broad application in devices driven by an electric field, but rather limited use when controlled by a magnetic field [1]. Liquid crystal sensitivity to magnetic fields remains an important challenge.

One of the methods for changing liquid crystal properties and making them suitable for a given application is by doping them with nanometre-sized particles. This procedure can enhance the existing properties, and introduce some new properties to the materials that are difficult or impossible to achieve by conventional chemical methods. Ferromagnetic nanoparticles appear to be an appropriate candidate for manipulating the magnetic properties of nematics. As has been predicted theoretically [2, 3] and shown in early experiments [4], suspensions of ferromagnetic nanoparticles in nematic liquid crystals can be realigned with much lower magnetic

fields than for undoped nematics. In the suspensions, ferromagnetic nanoparticles, which in some sense act as nanomagnets, can be easily aligned by a magnetic field. An existing coupling between the particles and nematic molecules ensures that the effect of a magnetic field is transferred into the underlying nematic host. The coupling strength strongly depends on the particle size and shape as well as on their surface treatment. However, the aggregation of particles, which appeared in the early ferronematic suspensions [4] and remained in the present work, has made some of the suspensions unstable.

7.1 Conclusions

In this thesis, magneto-optic effects in nematic liquid crystals and in ferronematic colloids have been investigated experimentally and theoretically. In the experimental part, suspensions of three different types of iron oxide nanoparticles in the nematic liquid crystal mixture E7 have been prepared and studied (see Chapter 5). These particles were: spherical magnetic nanoparticles of iron oxide, weakly-magnetic α-hematite nanorods, and ferromagnetic magnetite nanorods. The concentration of dopants in all suspensions was low (a volume fraction below 2×10^{-4}). The suspensions were investigated using magneto-optic and electro-optic measurements (see Chapter 3). The magneto-optic experiment was based on observing magnetic-field-induced Frederiks transition in a planar liquid crystal cell with a test magnetic field applied perpendicular to the cell plane. The Frederiks transition in the cell with the undoped nematic was detected at a field strength of around 1.5 kOe. The cells containing suspensions of magnetic nanoparticles and magnetite nanorods demonstrated a linear optical response at a low field and a decrease in the effective Frederiks threshold. The linear response was more significant in the magnetic nanoparticle suspensions - it was already observable at a field strength of only 100 Oe, which made them much more sensitive to the magnetic fields than the undoped nematic. It also increased with increasing the particle content in the suspension. However, the decrease of the Frederiks threshold observed in these suspensions was rather small - up to 10% lower than the threshold in the undoped nematic cell. The magnetite nanorod suspensions, on the other hand, demonstrated a much larger decrease in the threshold field - it was more than 20% lower than the threshold in the undoped nematic cell. The optical response measured in the cells with α-hematite nanorod suspensions did not demonstrate any additional effects, as compared to the response from the undoped nematic cell. The colloidal components of all suspensions were of comparable concentrations,

and were made from chemically similar material, but their magnetic properties were very different. An inevitable inference is that the effects observed in the suspensions with magnetic nanoparticles and magnetite nanorods are due to the magnetic properties of their dopants. The electro-optic measurements have shown that the suspensions with a low concentration of doped particles are characterised by the same dielectric constants and elastic constants as the undoped nematic.

The spherical magnetic nanoparticles were coated with Oleic acid, which produced a stable suspension in a solvent (heptane). However, the particles formed clusters in the nematic medium. Only the cell with the lowest volume content of particles, $f = 2 \times 10^{-5}$, appeared uniform without visible particle aggregates when observed under an optical microscope. Clusters of particles with a size of around 100 μm were observed in the cells with the higher concentration suspensions (with a volume fraction above 10^{-4}). The size and the number of clusters increased with increasing nanoparticle content. Magneto-optic experiments performed with the same cells demonstrated a decrease in the amplitude of laser beam intensity oscillations at magnetic fields above the Frederiks threshold. This may be caused by a scattering and depolarization of light by non-uniform nematic distortions in the cell, which appear around the large clusters of particles. Magneto-optic experiments repeated in these cells demonstrated a decrease in ferronematic response with time, indicating that the further aggregation process had possibly taken place on a long time scale (six months).

Apart from conventional Oleic acid (OA), another carboxylic acid - 4-n-Octyloxybiphenyl-4-carboxylic acid (OBPh) - has also been used as a stabilizing agent for the magnetite nanorods. OBPh has been selected because it contains octyloxybiphenyl group that resembles the chemical structure of E7 molecules, suggesting stronger interaction between the nanorods and nematic medium. Liquid crystal - OBPh coated nanorod suspensions have been more stable in a vial and also inside a cell. More uniform distribution of particles with much smaller aggregations has been detected in these suspensions under an optical microscope as compared to the suspensions of OA treated nanorods.

In the theoretical part of this thesis, two numerical models that predict the magneto-optic response in nematic and ferronematic cells have been developed. The nematic model is presented in Chapter 4 and the ferronematic model is presented in Chapter 6. The geometry of the system in these models corresponds to the experimental configuration. The cell has a planar alignment with a small surface pretilt angle. The magnetic field has two components: a test field applied

perpendicular to the cell, which causes the reorientational transition, and a small bias field applied in the direction of the initial nematic alignment, which ensures the initial alignment of nanoparticles in the suspensions.

The nematic model is based on the continuum theory and consists of two stages. At the first stage, an equilibrium orientation of the nematic director inside the cell is calculated for a given magnetic field by minimizing the free energy functional of the system. This director function is used in the next stage to model the propagation of a laser beam through the nematic layer. In particular, the model yields a phase lag between the ordinary and extraordinary components that a light beam acquires as it passes through the liquid crystal layer. It also predicts how the corresponding intensity of the beam after transmission through the cell and two polarizers depends on the test magnetic field. These results have been compared to the experimental data from the magneto-optic measurements in the cells with nematics E7 and 5CB. A fitting procedure produced a good quality agreement between the experiment and the model with reasonable values of the fitting parameters: the diamagnetic anisotropy for nematic E7 as 1.22×10^{-7} and for nematic 5CB as 1×10^{-7}.

The nematic model has predicted some new features in the magneto-optic response when both an in-plane bias magnetic field and a nematic pretilt at the surfaces are present. In the absence of the pretilt and the bias field, there are no director distortions below the threshold field and the Frederiks transition breaks reflection symmetry of the system at the threshold field. Both the pretilt and the bias field break the symmetry from the initial state, which leads to a smoothed Frederiks transition and small director distortions below the threshold. Changing the bias field direction causes another symmetry-breaking effect, which results in a shift of the effective Frederiks threshold. This effect, predicted in the model, has been confirmed experimentally in the cells with two different nematics: E7 and 5CB. A shift in the effective threshold of more than 200 Oersted has been measured when the bias field causing it was only 30 Oersted. This effect has been described analytically using the small angle approximation method.

The ferronematic model is based on a free energy functional from the Burylov-Raikher theory [3]. The model distinguishes two separate processes by which the magnetic field can influence the nematic host. There is a direct effect - associated with the diamagnetic anisotropy of nematic molecules, and an indirect effect - associated with the particle ferromagnetism. The direct effect dominates at a high magnetic field, determining threshold behaviour in the nematic switching, while

the indirect effect predicts a thresholdless ferronematic response at a low field. In the previous Burylov-Raikher [3] and Zadorozhnii [5, 6] models, the direct effect was assumed to be negligibly small in comparison with the indirect effect, which allowed the modelling of ferronematic response only at a low field, below the Frederiks threshold in the undoped nematic. In the present model, a combination of both effects allows a prediction of ferronematic behaviour over the whole range of magnetic fields. It contains two ferronematic parameters, which characterize the strength of particle ferromagnetic effect on the suspension response. These parameters are: a magnetic parameter κ, which scales the particle ferromagnetic effect with respect to the direct magnetic effect, and a coupling parameter ω, which determines the effective coupling energy between colloidal inclusions and a host nematic. From a theoretical point of view, a distinction is necessary between the cases of small and large magnetic parameter, specifically $\kappa < 1$ and $\kappa > 1$. In the former case, the direct effect dominates the magnetic response, whereas in the latter case, indirect effect prevails. Analysis of the experimental data suggests that the direct effect dominates in real ferronematic suspensions. However, the model can also treat the case when the indirect effect is dominant.

The numerical model has been fitted to experimental data for two classes of ferronematic suspensions: one containing spherical magnetic nanoparticles coated with OA, and another containing magnetite nanorods stabilized with OBPh. The ferronematic parameters κ and ω are assumed as fitting parameters in simulation the experimental magneto-optic data. The fitting procedure produces κ and ω for which the best possible agreement between the model and the experimental data is obtained. For all suspensions, the obtained magnetic parameters are lower than unity, indicating that in these ferrosuspensions the direct nematic effect still dominates the indirect effect. Using the best fit values of κ and ω from spherical magnetic nanoparticle suspensions with different concentrations, an effective coupling energy density between a nematic host and magnetic inclusions has been evaluated. Its value is $(4 \pm 0.4) \times 10^4$ erg cm^{-3}. For the magnetite nanorod suspension, the estimate of the coupling energy is around 5×10^5 erg cm^{-3}. This calculation is is not as reliable because it is based on only one set of experimental data. Nevertheless, it shows that the effective coupling energy between nematic E7 and the magnetite nanorods is more than one order magnitude higher than the coupling energy associated with spherical iron oxide nanoparticles.

A good agreement between the theoretical curve and the experimental data for the magnetite nanorod suspension has been obtained over the whole measured range of magnetic fields, which demonstrates the ability of the model to describe the

ferronematic response. In the case of the spherical magnetic nanoparticle suspension, the numerical model shows good agreement with experimental data obtained from the lowest concentration sample, but for the higher concentrations, despite some deviation between the theory and experiment, the theory still predicts a basic trend in the system behaviour. The lack of a better fit can be explained by particle aggregation; this effect is not taken into account in the model. The evidence of particle aggregation in the higher concentration suspensions has been confirmed in Chapter 5 by optical microscopy. Investigations of the particle clusters in the nematic medium, preformed by Buluy *et al.* [7], suggested that there are non-uniform local director distortions around big clusters, the size of which increases with an increase of the external magnetic field. Some ways of including this process in the numerical model will be required in order to predict the optical response for aggregated suspensions. This and several other aspects will require further work, which will be outlined in the next section.

7.2 Future work

There are several interesting and promising areas of both theory and experiment which can be investigated further. One of them is a study of partly-aggregated suspensions. As has been shown in Chapter 5, with increasing the amount of dopants, large clusters of particles (up to 100 μm in size) are formed inside the cells. The partly-aggregated suspensions still can be very sensitive to a low magnetic field [7]. However, a magneto-optic response in these cells cannot be fully described by the present continuum model. The extra effects in aggregated suspensions which are not predicted within the model, such as a decrease in the intensity amplitude, might be an evidence of non-uniform director distortions around the particle clusters. The present model assumes a collective nematic response, while in aggregated suspensions, an individual response of particle clusters is likely to occur. This has been demonstrated in the recent publication of Buluy *et al.* [7]. In this paper the authors estimated the size of the director distortions around clusters and their changes with increasing magnetic field strength. The complete description of partly aggregated suspensions, however, will require a more fundamental approach and detailed modelling.

It is obvious that in the case of partly-aggregated suspensions, a magneto-optic response is driven by an individual response of each cluster rather than their collective behaviour. So, the new model should based a on the consideration of

the director orientation around a single cluster of particles with a characteristic size and in the presence of external magnetic field. If this director profile is known, then an effective phase retardation caused by a single cluster could be found by integrating along the direction of one of the space axes. Magneto-optic response modelling in this case could be done by estimating a number of particle clusters in path of the testing laser beam and multiplying it by the phase retardation introduced by each cluster. A level of light depolarization, which determine a reduced amplitude of the intensity oscillations, than can be calculated using an amount of clusters, the characteristic size of director distortions around them and characteristics phase retardation. A realistic model will also require a due account of the polydispersity in the cluster size and estimating a level of light scattering.

In this work, the possibility of preparing stable and highly sensitive ferromagnetic colloids, based on nematic liquid crystals, has been demonstrated. However, further experimental investigations will be required with the aim of improving the magneto-optic properties of ferronematic colloids. One of the methods is to utilize new magnetic nanomaterials for the preparation of ferronematic colloids. As suggested in this work, particles should possess strong ferromagnetic properties and ideally have elongated shape (rodlike or elliptical). The stronger magneto-optic response is also expected from the suspensions with a higher concentration of dopants. However, either with increasing the particle magnetic moments or their amount, they are likely to form clusters or chains [7, 8], leading to suspension instability. So, a choice of suitable surfactant, which can prevent or control this process, is also essential. A surfactant should bind strongly to the particle surfaces and provide a good coupling with liquid crystal molecules. A good solubility of nanoparticles in liquid crystal medium can be achieved by using mesogenic surfactants [9, 10]. This will require a complex approach from both chemical and physical aspects.

Superparamegnetic nanoparticles are also promising materials for preparation of liquid-crystal-based colloids. These materials are now commercially available, as they have attracted a lot of interests for the bio-sensing and drug delivery application [11, 12]. In the absence of external magnetic field, on average, there are no permanent magnetic moments in these particles. However, they can be easily magnetized in the magnetic field. Absence of permanent dipole moment and their small size should simplify the preparation of colloids, as there is no direct magnetic interactions between particles. Nevertheless, their high magnetic polarizability should lead to a decrease in the response threshold.

Utilizing multiferroic nanoparticles, which demonstrate ferroelectricity as well as ferromagnetism, is another possible approach that promises interesting results in manipulating liquid crystal properties. Recently, a systematic synthesis of single crystal multiferroic nanoparticles of $BiFeO_3$ has been reported [13, 14]. Preparation of composite nanostructures with multiferroic properties, such as nanoparticles of $CoFe_2O_4$–$BaTiO_3$, has also been achieved [15]. Liquid-crystal-based colloids of multiferroic nanocolloids are expected to demonstrate both an enhancement in dielectric and optical anisotropy together with an increased sensitivity to magnetic fields.

In conclusion, we have demonstrated that a suspension of ferromagnetic nanoparticles can be sensitive to magnetic fields of the order of tens of Oersted units. The problem of suspension stability can be overcome by selecting a suitable surfactant for magnetic nanoparticles and by keeping a low concentration of nanoparticles. Future work is expected to increase ferronematic effect in such a way as to construct magnetically driven liquid crystal devices. The potential applications of ferronematic composites would include several magnetic device principles. Examples of such possible applications could be the construction of optical sensors for low magnetic fields, driven by liquid crystal reorientation, and also devices that employ optical switching triggered by magnetic fields.

References

[1] L. M. Blinov and V. G. Chigrinov. *Liquid Crystal Devices: Physics and Applications*. Artech-House, Boston-London, 1999.

[2] F. Brochard and P. G. de Gennes. Theory of magnetic suspensions in liquid crystal. *Journal de Physique (Paris)*, 31:691–708, 1970.

[3] S. V. Burylov and Yu. L. Raikher. Macroscopic properties of ferronematics cause by orientational interactions on the particles surface. *Molecular Crystals and Liquid Crystals*, 258:107–122, 123–141, 1995.

[4] S.-H. Chen and N. M. Amer. Observation of macroscopic colective behavior and new texture in magnetically doped liguid crystal. *Physical Review Letters*, 51(25):2298–2301, 1983.

[5] V. I. Zadorozhnii, A. N. Vasilev, V. Yu. Reshetnyak, K. S. Thomas, and T. J. Sluckin. Nematic director response in ferronematic cells. *Europhysics Letters*, 73(3):408–414, 2006.

[6] V.I. Zadorozhnii, T. J. Sluckin, V. Yu. Reshetnyak, and K.S. Thomas. The Frederiks effect and related phenomena in ferronematic materials. *SIAM Journal of Applied Mathematics*, 68(6):1688–1716, 2008.

[7] O. Buluy, S. Nepijko, V. Reshetnyak, E. Ouskova, V. Zadorozhnii, A. Leonhardt, M. Ritschel, G. Schönhense, and Yu. Reznikov. Magnetic sensitivity of a dispersion of aggregated ferromagnetic carbon nanotubes in liquid crystals. *Soft Matter*, 7:644–649, 2011.

[8] D. Eberbeck, F. Wiekhorst, U. Steinhoff, and L. Trahms. Aggregation behaviour of magnetic nanoparticle suspensions investigated by magnetorelaxometry. *Journal of Physics: Condensed Matter*, 18:S2829–S2846, 2006.

[9] S. Khatua, P. Manna, W.-S. Chang, A. Tcherniak, E. Friedlander, E. R. Zubarev, and S. Link. Plasmonic nanoparticles - liquid crystal composites. *Journal of Physical Chemistry C*, 114(16):7251–7257, 2010.

[10] M. Draper, I. M. Saez, S. J. Cowling, P. Gai, B. Heinrich, B. Donnio, D. Guillon, and J. W. Goodby. Self-assembly and shape morphology of liquid-crystalline gold metamaterials. *Advanced Functional Materials*, 21:1260–1278, 2011.

[11] Q. A. Pankhurst, J. Connolly, S. K. Jones, and J. Dobson. Applications of magnetic nanoparticles in biomedicine. *Journal of Physics D: Applied Physics*, 36:R167–R181, 2002.

[12] U. Jeong, X. Teng, Y. Wang, H. Yang, and Y. Xia. Superparamagnetic colloids: controlled synthesis and niche applications. *Advanced Materials*, 19: 33–60, 2007.

[13] T. J. Park, G. C. Papaefthymiou, A. J. Viescas, A. R. Moodenbaugh, and S. S. Wong. Size-dependent magnetic properties of single-crystalline multiferroic $BiFeO_3$ nanoparticles. *Nano Letters*, 7(3):766–772, 2007.

[14] S. M. Selbach, T. Tybell, M.-A. Einarsrud, and T. Grande. Size-dependent properties of multiferroic $BiFeO_3$ nanoparticles. *Chemistry of Materials*, 19: 6478–6484, 2007.

[15] J. Nie, G. Xu, and C. Cheng Y. Yang. Strong magnetoelectric coupling in $CoFe_2O_4$-$BaTiO_3$ composites prepared by molten-salt synthesis method. *Materials Chemistry and Physics*, 115:400–403, 2009.

Appendix A

Numerical methods for modelling nematics and ferronematics

This appendix describes the numerical methods that are used for modelling magnetic-field-induced transitions in nematic and ferronematic cells, in Chapter 4 and 6, respectively. Section A.1 provides a brief description of Broyden's method [1]. This method is utilized for the numerical solving of the Euler-Lagrange equation (4.7), which determines the director orientation in a nematic cell (see Section 4.1), and the system of Equations (6.14a, 6.14b), which determines the equilibrium nematic and magnetic director orientations in a ferronematic cell (see Section 6.3). The spectral methods [2] that are used for numerical evaluation of the spatial differentials in the Euler-Lagrange equations and the integral in Equation (4.9) are outlined in Section A.2 and A.3, respectively.

A.1 Broyden's method for solving nonlinear simultaneous equations

Broyden's method allows solution of a set of nonlinear simultaneous equations [1]. The set of n equations $F_i(x_1, x_2, ..., x_n) = 0,\ i = 1, 2, ..., n$, where $x_1, x_2, ..., x_n$ are independent variables, can be expressed as the simultaneous zeroing of a set of n functions. This set of functions is assumed to be real, continuous and differentiable with respect to the variables.

Broyden's method is a modification of Newton's method. Newton's method considers the set of n equations, which may be written as

$$\boldsymbol{F}(\boldsymbol{x}) = 0, \tag{A.1}$$

where $\boldsymbol{x}$ is the column vector of independent variables and $\boldsymbol{F}$ is the column vector of functions F_i. The zeros of the functions are found using a series of successive approximations to the solution. Assuming that $\boldsymbol{x}_n$ is the n-th approximation to the solution and $\boldsymbol{F}_n$ is the value of functions $\boldsymbol{F}(\boldsymbol{x}_n)$, then Newton's method allows us to define the next approximation to the solution as

$$\boldsymbol{x}_{n+1} = \boldsymbol{x}_n - \hat{\boldsymbol{A}}_n^{-1}\boldsymbol{F}_n, \tag{A.2}$$

where $\hat{\boldsymbol{A}}_n$ is the Jacobian matrix $[\partial F_i/\partial x_j]$ evaluated for the n-th approximation solution.

Newton's method is very simple in realization. However, it suffers from two serious disadvantages. Firstly, the finding of a sufficiently accurate estimate of the solution and the computing time required for this is completely reliant on the initial estimate of the solution. Ideally, the initial estimated solution is expected to be reasonably close to the exact solution. Otherwise, the method will fail to converge or produce a physically wrong solution. This problem can be solved by making a more accurate estimate of the physically expected final solution. In the application of this method to solving equations for nematic or ferronematic models, this problem is overcome in the following way. The set of solutions for nematic or magnetic director profiles inside the cell are calculated for a range of external magnetic fields, starting with zero field strength and going up to the maximum value. As the initial approximation to the solution at zero field, the director orientation function is assumed to be uniform and equal to a pretilt angle. For each next magnetic field step, the solution from the previous step is taken as the initial estimate. If the magnetic field step is small enough, the director orientations for two successive fields are assumed not to differ greatly from each other. So, the initial estimation for the solution at each magnetic field step is quite accurate, and finding the exact solution does not require too many Newton iteration steps.

The second disadvantage of Newton's method is the difficulty of computing the Jacobian matrix at each iteration step. Even if it is possible to differentiate the functions F_i analytically, it requires the calculation of all n^2 partial derivatives at each step. However, in the majority of problems, the functions are complicated

and the Jacobian matrix should be obtained by a numerical approximation, which requires a lot of computing time. In Broyden's method this problem is overcome as follows. The Jacobian matrix is calculated only once at the beginning of the iteration process. At each next step, the corrections to the approximate Jacobian matrix $\hat{\boldsymbol{A}}_{n+1}$ are computed from values of the vector functions and the estimated solution. There are several methods for estimating these corrections, the details of which can be found in [1]. In the numerical models described in this thesis the following approximation was employed:

$$\hat{\boldsymbol{A}}_{n+1} = \hat{\boldsymbol{A}}_n + \frac{\boldsymbol{y}_n - \hat{\boldsymbol{A}}_n \boldsymbol{p}_n}{||\boldsymbol{p}_n||} \boldsymbol{p}_n^T, \tag{A.3}$$

where $\boldsymbol{p}_n = \boldsymbol{x}_{n+1} - \boldsymbol{x}_n$ and $\boldsymbol{y}_n = \boldsymbol{F}_{n+1} - \boldsymbol{F}_n$. Clearly, after each step the approximated Jacobian becomes worse than the numerically calculated one. However, if the number of Newton iteration steps is not large (which appears to be the case in the nematic and the ferronematic numerical models) this method produces an accurate result and significantly reduces the computing time.

A.2 Differentiation on a Chebyshev grid

In the numerical models, the nematic and the magnetic directors are described as a set of values on the spatial grid rather than as a continuous function. The Chebyshev points are chosen as the grid, the nodes of which, z_i, are defined as

$$z_i = \cos(i\pi/N), \quad i = 0, 1, ..., N. \tag{A.4}$$

This grid has $N+1$ nodes on the segment $[-1, 1]$. It should be mentioned that the Chebyshev points are more concentrated near the edges than in the centre. At the same time, the functions of the nematic and the magnetic directors are assumed to have a higher gradient near the edges of the cell as a result of strong anchoring conditions. This means that utilizing the Chebyshev grid matches the geometry of the problem and allows the variable functions to be found more accurately.

The equations that determine the nematic or the magnetic director alignment contain derivatives over the coordinate z. These derivatives are approximated using spectral methods [2] due to their high accuracy and simplicity in realization. In this method, any given function $f(z)$ is defined as a vector consisting of the

function values on a grid $\{z_i\}$: $f_i = f(z_i),\ i = 0, 1, ..., N$. The differentiation is approximated by multiplication by an $(N+1) \times (N+1)$ matrix $\hat{\boldsymbol{D}}_N$, which is named differentiation matrix:

$$\frac{\partial}{\partial z}\boldsymbol{f} \simeq \hat{\boldsymbol{D}}_N \boldsymbol{f}. \tag{A.5}$$

The differentiation matrix on the Chebyshev grid is defined by the following theorem.

Theorem A.1. Chebyshev differentiation matrix.
For each $N \geqslant 1$, let the rows and columns of the $(N+1) \times (N+1)$ Chebyshev spectral differentiation matrix $\hat{\boldsymbol{D}}_N$ be indexed from 0 to N. The entries of this matrix are

$$(D_N)_{00} = \frac{2N^2+1}{6}, \qquad (D_N)_{NN} = -\frac{2N^2+1}{6}, \tag{A.6a}$$

$$(D_N)_{ii} = \frac{-z_i}{2(1-x_i^2)}, \qquad i = 1, ..., N-1, \tag{A.6b}$$

$$(D_N)_{ij} = \frac{c_i}{c_j}\frac{(-1)^{i+j}}{(z_i - z_j)}, \qquad i \neq j,\ i, j = 0, ..., N, \tag{A.6c}$$

where

$$c_i = \begin{array}{ll} 2, & i = 0 \text{ or } N \\ 1, & \text{otherwise.} \end{array}$$

The derivation of this theorem can be found in [2].

A.3 Clenshaw-Curtis quadrature

To calculate the optical phase lag of a liquid crystal layer with a given director profile, it is necessary to evaluate the integral in Equation (4.9). Let us denote the integral that we wish to calculate as:

$$I = \int_{-1}^{1} f(z)dz, \tag{A.7}$$

where $f(z)$ is defined as a set of values $\{f_i\}$ on $N+1$ Chebyshev points. The spectral method for numerical integration in Chebyshev points is Clenshaw-Curtis

quadrature. In this method the integral is approximated by the value I_N that is obtained numerically from the following summation:

$$I_N = \sum_{i=0}^{N} f_i w_i, \tag{A.8}$$

where w_i are Clenshaw-Curtis weights. These can be calculated as:

$$w_i = \frac{2}{N} \sum_{k=0}^{M} \frac{\cos(2k\pi i/N)}{1-4k^2}, \tag{A.9}$$

where $M = N/2$ for even N, and $M = (N+1)/2$ for odd N. More details of this method and its realization as a MATLAB code are presented in [2].

References

[1] C. G. Broyden. A class of methods for solving nonlinear simultaneous equations. *Mathematics of Computation*, 19(92):577–593, 1965.

[2] L. N. Trefethen. *Spectral Methods in Matlab*. SIAM, Philadelphia, 2000.

Appendix B

List of publications

Publications from results reported in this thesis

Journal papers:

N. Podoliak, O. Buchnev, G. D'Alessandro, M. Kaczmarek, and T. J. Sluckin. Large effect of a small bias field in liquid-crystal magnetic transitions. *Physical Review E*, 82: 030701R, 2010.

N. Podoliak, O. Buchnev, O. Buluy, G. D'Alessandro, M. Kaczmarek, Yu. Reznikov, and T. J. Sluckin. Macroscopic optical effects in low concentration ferronematics. *Soft Matter*, 7: 4742 - 4749, 2011.

N. Podoliak, O. Buchnev, D. V. Bavykin, A. N. Kulak, M. Kaczmarek, and T. J. Sluckin. Synthesis of magnetite nanorods thermotropic liquid crystal suspensions. (in preparation).

Conference papers:

N. Podoliak, D. Bavykin, O. Buchnev, G. D'Alessandro, M. Kaczmarek, and T. J. Sluckin. Effect of particle shape and functionality on magnetic field induced Frederiks transition in ferronematics. Oral presentation at the *14th International Topical Meeting on Optics of Liquid Crystals*, Yerevan, Armenia 2011.

N. Podoliak, O. Buchnev, M. Kaczmarek, G. D'Alessandro, T. J. Sluckin, O. Buluy, and Yu. Rezniko. Magnetic field induced Frederiks transition in nematics and

ferronematics. Poster presentation at the *3rd International Workshop on Liquid Crystal for Photonics*, Elche, Spain 2010.

N. Podoliak, O. Buchnev, M. Kaczmarek, G. D'Alessandro, T. J. Sluckin, O. Buluy,and Yu. Reznikov. Frederiks transition in ferromagnetic liquid crystal suspension. Poster presentation at the *23rd International Liquid Crystal Conference*, Krakow, Poland 2010.

N. Podoliak, O. Buchnev, M. Kaczmarek, G. D'Alessandro, T. J. Sluckin, O. Buluy, and Yu. Reznikov. The role of bias magnetic field for enhancing the magneto-optic response of nematic liquid crystals. Poster presentation at the *23rd International Liquid Crystal Conference*, Krakow, Poland 2010.

Other publications by the author

Journal papers:

N. Podoliak, D. Bartczak, O. Buchnev, A. G. Kanaras, and M. Kaczmarek. High nonlinear and photorefractive response in nematic liquid crystals doped with gold nanoparticles. (submitted to *Journal of Physical Chemistry C*).

Conference papers:

O. Buchnev, D. Bartczak, M. Kaczmarek, A. G. Kanaras, and N. Podoliak. Liquid crystal - gold nanoparticles suspension as a photorefractive material. Poster presentation at the *3rd International Workshop on Liquid Crystal for Photonics*, Elche, Spain 2010.

N. Podoliak, D. Bartczak, O. Buchnev, M. Kaczmarek, and A. G. Kanaras. Liquid crystal doped with gold nanoparticles as a photorefractive material. Poster presentation at the *23rd International Liquid Crystal Conference*, Krakow, Poland 2010.

O. Buchnev, D. Bartczak, A. G. Kanaras, N. Podoliak, V. Reshetnyak, Yu. Reznikov, and M. Kaczmarek. Suspension of liquid crystal-gold nanoparticles as a photorefractive material. Poster presentation at the *13th Topical Meeting on Optics of Liquid Crystals*, Eriche, Italy, 2009.